The Bolocam Lockman Hole Millimeter-Wave Galaxy Survey

by

G. T. Laurent

B.S., Colorado School of Mines, 1999

M.S., University of Colorado, 2001

A thesis submitted to the
Faculty of the Graduate School of the
University of Colorado in partial fulfillment
of the requirements for the degree of
Doctor of Philosophy
Department of Astrophysics and Planetary Sciences
2005

This thesis entitled:
The Bolocam Lockman Hole Millimeter-Wave Galaxy Survey
written by G. T. Laurent
has been approved for the Department of Astrophysics and Planetary Sciences

Prof. Jason Glenn

Prof. Webster Cash

Prof. James Green

Prof. John Price

Prof. John Stocke

Date ____________

The final copy of this thesis has been examined by the signatories, and we find that both the content and the form meet acceptable presentation standards of scholarly work in the above mentioned discipline.

Laurent, G. T. (Ph.D., Astrophysical, Planetary, and Atmospheric Sciences)

The Bolocam Lockman Hole Millimeter-Wave Galaxy Survey

Thesis directed by Prof. Jason Glenn

This work presents results of a new deep ($\sigma_{1.1\mathrm{mm}} \simeq 1.4$ mJy beam^{-1}) 1.1 mm submillimeter galaxy survey using Bolocam, a millimeter-wavelength bolometer array camera designed for mapping large fields at fast scan rates, without chopping. A map, galaxy candidate list, and derived number counts are presented. The data were reduced using a custom software pipeline to remove correlated sky and instrument noise via a principal component analysis. Extensive simulations and jackknife tests were performed to confirm the robustness of our source candidates and estimate the effects of false detections, bias, and completeness. In total, 17 source candidates were detected at a significance $\geq 3.0\ \sigma$, with six expected false detections. From both our observed number counts and a fluctuation analysis, we estimate the underlying differential number count distribution of submillimeter galaxies and find it to be in general agreement with previous surveys.

This work also presents 350 μm photometry of all 17 galaxy candidates detected in the Lockman Hole survey. Nine of the Bolocam galaxy candidates were detected at 350 μm and two new candidates were serendipitously detected at 350 μm (bringing the total in the literature detected in this way to three). Five of the galaxies have published spectroscopic redshifts, enabling investigation of the implied temperature ranges and a comparison of photometric redshift techniques. Because $\lambda = 350\ \mu$m lies near the spectral energy distribution peak for $z \approx 2.5$ thermally emitting galaxies, luminosities can be measured without extrapolating to the peak from detection wavelengths of $\lambda \geq$ 850 μm. Characteristically, the galaxy luminosities lie in the range $1.0 - 1.2 \times 10^{13}$ L$_{\odot}$, with dust temperatures in the range of 40 K to 70 K, depending on the choice of spectral index and wavelength of unit optical depth. The implied dust masses are 3 - 5 × 10^8 $M_\odot$. We find that the far-infrared to radio relation for star-forming ULIRGs systematically overpredicts the radio luminosities and overestimates redshifts on the order of $\Delta z \approx 1$, whereas redshifts based on either on submillimeter data alone or the 1.6 μm stellar bump and PAH features are more accurate.

Dedication

This work is dedicated to my wife Nicole. It is her constant love, support, and encouragement that has made this research possible.

Acknowledgements

With alacrity, I acknowledge the support of the entire Bolocam instrument and software team, including Jason Glenn, James Aguirre, Sunil Golwala, Douglas Haig, Peter Ade, Jamie Bock, Samantha Edgington, Alexey Goldin, Ben Knowles, Andrew Lange, Phil Maloney, Phil Mauskopf, Hien Nguyen, Phillippe Rossinot, Jack Sayers and Patrick Stover.

In addition, I acknowledge the support of the CSO director and staff, the support of Kathy Deniston, and the follow-up work provided by Eiichi Egami, Attila Kovács, George Rieke, Rob Ivison and Min Yun.

This work was supported in part by NSF grants AST-0098737, AST-9980846, and AST-0206158, PPARC grants PPA/Y/S/2000/00101 and PPA/G/O/2002/00015, and NASA GSRP Fellowship NGT5-50384.

Contents

Chapter

Appendix

Tables

Table

Figures

Figure

Chapter 1

Introduction

Submillimeter galaxies are extremely luminous ($L \sim 10^{13} L_{\odot}$), high-redshift ($z > 1$), dust-obscured galaxies detected by their thermal dust emission (for a review see Blain et al. 2002). The dust is heated by the ultraviolet and optical flux from young stars associated with prodigious inferred star formation rates (SFRs) of $\sim 100 - 1000$ $\mathrm{M}_{\odot}$ yr^{-1} (Blain et al., 2002). Although $\sim \frac{1}{3}$ of sources appear to contain an active galactic nucleus (AGN; Alexander et al., 2003; Ivison et al., 2004), in nearly all cases the AGNs are not bolometrically important ($<$ 20%; Alexander et al., 2004) or are Compton thick. Given these SFRs, a burst of duration 10^8 yr would be sufficient to form all the stars in an elliptical galaxy, making it plausible that submillimeter galaxies are the progenitors of elliptical galaxies and spiral bulges (Smail et al., 2002; Swinbank et al., 2004). Deep (sub)millimeter surveys with SCUBA (Holland et al., 1999) and MAMBO (Bertoldi et al., 2000) have now resolved 10%$-$40% of the cosmic far-infrared background (Puget et al., 1996; Hauser et al., 1998; Fixsen et al., 1998) into submillimeter galaxies in blank-field surveys (e.g., Greve et al., 2004; Borys et al., 2003; Scott et al., 2002) and 40%$-$100% using lensing galaxy clusters (Blain et al., 1999; Cowie et al., 2002). In total, hundreds of galaxy candidates have been detected by their thermal dust emission. Photometric redshifts constrain most of the submillimeter galaxies found so far to lie at $z > 1$ (e.g., Carilli & Yun, 1999; Yun & Carilli, 2002; Aretxaga et al., 2003). Spectroscopic redshifts of those galaxies with radio counterparts (65%) confirm the sources to lie at high redshift, yielding a submillimeter galaxy distribution peaking $z = 2.4 \pm 0.65$ (Chapman et al., 2005).

Bolocam is a new millimeter-wave bolometer camera for the Caltech Submillimeter Observatory (CSO).[1] Bolocam's large field of view ($8'$), $31''$ beams (FWHM at $\lambda = 1.1$ mm), and AC biasing scheme make it particularly well-suited to finding rare, bright submillimeter galaxies and for probing large-scale structure. We have used Bolocam to conduct a survey toward the Lockman Hole for submillimeter galaxies. The Lockman Hole is a region in UMa in which absorbing material, such as dust and galactic hydrogen, is highly rarefied ($\mathrm{H_I}$ column density of $N_{\mathrm{H}} \approx 4.5$ x 10^{19} cm^{-2}; Jahoda et al., 1990), providing a transparent window for sensitive extragalactic surveys over a wide spectral range, from the infrared and millimeter wavebands to UV and X-ray observations. Submillimeter (Scott et al., 2002; Fox et al., 2002; Ivison et al., 2002; Eales et al., 2003) and millimeter-wave (Greve et al., 2004) surveys for submillimeter galaxies have already been done toward the Lockman Hole. It is one of the one-quarter square degree fields of the SCUBA SHADES,[2] the focus of a deep extragalactic survey with *XMM-Newton* (Hasinger et al., 2001), and a target field for *Spitzer* guaranteed time observations. The coverage of the Lockman Hole region by several surveys therefore makes it an excellent field for intercomparison of galaxy candidate lists and measuring spectral energy distributions (SEDs), which will ultimately enable dust temperatures and redshifts to be constrained.

Clearly, it is crucial to characterize the spectral energy distributions (SEDs) where their emission peaks ($\lambda = 350$ μm for 40 K dust at a redshift of $z = 2.5$), measure their redshifts and luminosity functions, determine their power sources, and integrate them into theories of galaxy formation. We have therefore used the Submillimeter High Angular Resolution Camera (SHARC II) to obtain 350 μm photometry of all 17 submillimeter

---

[1] See http://www.cso.caltech.edu/bolocam.

[2] See http://www.roe.ac.uk/ifa/shades/links.html.

galaxy candidates from the Bolocam survey. Although submillimeter galaxy SEDs peak at a few hundred microns for all but the highest redshifts, $\lambda \geq 850$ μm surveys have been most successful at detecting galaxies because of the lower atmospheric noise and greater transmission, and less stringent telescope surface requirements. Most of the detections have been low signal-to-noise ratio (just over thresholds of 3-4 σ), necessitating multiwavelength confirmation. Furthermore, the SEDs have been extrapolated shortward from 850-1200 μm over the peak, or between 850-1200 μm and the far-infrared, to estimate dust temperatures, luminosities, and star formation rates. Clearly, 350 μm photometry can confirm galaxy candidates and sample the SEDs near their peaks for more precise inferences of physical parameters. Similarly, because of the difficulty in obtaining spectroscopic redshifts of large numbers of highly obscured galaxies, various photometric redshift estimation techniques have emerged, notably based on the far-infrared to radio luminosity relation in ULIRGs (Carilli & Yun, 1999; Yun & Carilli, 2002) and the stellar continuum bump in the infrared for *Spitzer*-detected galaxies (Egami et al., 2004; Sawicki, 2002). However, despite the difficulty, candidate spectroscopic redshifts have been obtained for $\sim$ 73 galaxies (Chapman et al., 2005). Thus, with well-determined dust-emission SEDs, including 350 μm, photometric techniques can be compared to spectroscopic redshifts.

This thesis is arranged as follows. A background on the history of submillimeter galaxies is presented in § 2. In §§ 3 - 4 the Bolocam instrument and the Lockman Hole observations are described. In § 5 the data reduction pipeline, including pointing and flux calibration, cleaning and sky subtraction, and mapping, is described. In § 6 the source candidate list and tests of the robustness of the candidates are presented. I devote §§ 7 - 8 to the extraction of the number counts versus flux density relation using simulations designed to characterize the systematic effects in the data reduction and the false detections, completeness, and bias in the survey. In § 9 I discuss the implications of the survey number counts. I present 350 μm photometry of all 17 submillimeter galaxy candidates from the Bolocam Lockman Hole survey in § 10. I estimate photometric redshifts in § 11, which I subsequently use to estimate physical properties of these galaxies (§ 12). In § 13 I describe future work for this program, and in § 14 I give conclusions.

Throughout the paper, a cosmology of $H_0 = 70$ km s^{-1} Mpc^{-1}, $\Omega_M = 0.3$, and $\Omega_\Lambda = 0.7$ is assumed.

Chapter 2

Background

2.1 Cosmic Infrared Background

The cosmic infrared background (CIB) was discovered by COBE (Hauser et al., 1998; Puget et al., 1996; Fixsen et al., 1998) and was found to have an integrated intensity of 14 nW m^{-2} ster^{-1}. This represents 20% of the total expected flux associated with the energy release of nucleosynthesis throughout the history of the universe (Fixsen et al., 1998). The detection of the infrared background was a critical discovery of cosmology, as the radiation contains the cumulative emissions of stars and galaxies from a major epoch of structure formation. (Due to the redshifting to longer wavelengths and the reprocessing of shorter wavelengths by dust, most of the energy released in the formation of stars and galaxies is expected to be emitted between 1 μm and 1 mm.) The COBE measurements therefore constrain models of the cosmological history of star formation, and the buildup of heavy elements and dust.

The source of this radiation remained unresolved until recently, when deep submillimeter- and millimeter-wave surveys (hereafter referred to as submillimeter) with SCUBA (Holland et al., 1999) and MAMBO Bertoldi et al. (2000) began to emerge, imaging the sky in the atmospheric windows of 450 and 850 μm (SCUBA) and 1.2 mm (MAMBO). These instruments were a critical advancement in bolometer technology, replacing previous single-pixel and one-dimensional array instruments. The submillimeter surveys of SCUBA and MAMBO revealed a population of extremely luminous

($L \sim 10^{13} L_\odot$), high-redshift ($z > 1$) galaxies. Currently, hundreds of these galaxies have been detected by their thermal continuum emission (e.g., Scott et al., 2002; Borys et al., 2003; Greve et al., 2004; Laurent et al., 2005), resolving 10% - 40% of the CIB. Taking advantage of gravitational lensing of these galaxies by intervening galaxy clusters (Blain et al., 1999; Cowie et al., 2002), 40% - 100% of the CIB has been resolved into submillimeter galaxies.

2.2 Submillimeter Galaxies

The primary (99%, Blain et al. 2002) source of submillimeter radiation from these galaxies is through re-radiated thermal continuum emission from dust grains in the interstellar medium (ISM), which has been heated by either ultraviolet and optical flux from young stars (with extreme inferred star formation rates of SFR $\sim 10^3$ $\mathrm{M}_\odot$ yr^{-1}; Blain et al. 2002) or accretion onto supermassive black holes (Alexander et al., 2003). The other source of submillimeter flux is from line emission from atomic and molecular transitions in the interstellar gas, including CO rotational transitions (which may be used to obtain accurate spectroscopic redshifts for the galaxies, Frayer et al. 1998).

The thermal continuum radiation from dust takes the form of modified blackbody emission spectrum:

$$f_\nu \propto \epsilon_\nu B_\nu(T) \propto [1 - \exp(-\tau_\nu)] B_\nu(T),$$

where $B_\nu(T)$ is the Planck function evaluated at dust temperature, T, and frequency, ν, and τ_ν is the optical depth of the dust:

$$\tau_\nu = \left(\frac{\nu}{\nu_0}\right)^\beta .$$

Because this spectrum is featureless, it is difficult to determine the source(s) of optical and UV flux that heat the dust grains; both intense star formation from young high-mass stars as well and accretion disks around active galactic nuclei (AGN) are capable of powering the thermal emission. Furthermore, these regions of dust emission are optically thick, making it difficult to glean information from the optical and UV. Observations of local ultra-luminous infrared galaxies (ULIRGs), however, suggest that intense star formation is the dominant mechanism (see below).

The thermal spectrum of submillimeter galaxies is a key feature of their detection at submillimeter wavelengths because the spectral energy distribution (SED) is sampled at wavelengths at which the SED is a strongly increasing function of frequency. Put simply, more distant galaxies are sampled closer to the peak of the SED. A desirable consequence of this strong negative K-correction at submillimeter wavelengths (in which flux density rises up the steep Rayleigh-Jeans side of the spectrum with redshift) is that the detection sensitivity of submillimeter galaxies is approximately uniform for galaxies of a given intrinsic luminosity for redshifts $1 < z < 10$. This effect is shown in Figure 2.1. Infrared and optical flux densities decline rapidly with increasing redshift; surveys at these wavelengths therefore preferentially select lower redshift galaxies. For wavelengths longer than $\sim 350\ \mu$m, the flux density from galaxies with $z > 1$ ceases to decline rapidly with distance, but instead remains relatively constant with increasing redshift. While the effect becomes more significant at longer wavelengths, the intrinsic flux from submillimeter galaxies begins to decline rapidly. Thus surveys near 1 mm are optimal in sampling the brightest submillimeter galaxies near the peak of their SEDs, roughly independent of redshift. Optical and radio surveys subsequently complement the submillimeter surveys, as they probe different physical signatures of the galaxies (i.e. radio synchrotron radiation) and have much finer angular resolution.

While submillimeter surveys are uniquely capable of detecting high redshift submillimeter galaxies, they are not immune to their own selection effects. Although the negative K-correction mitigates the inverse square law with distance, all surveys (including those in the submillimeter waveband) suffer from cosmological $(1+z)^{-4}$ surface brightness dimming due to the expansion of space, and photon energy and photon arrival

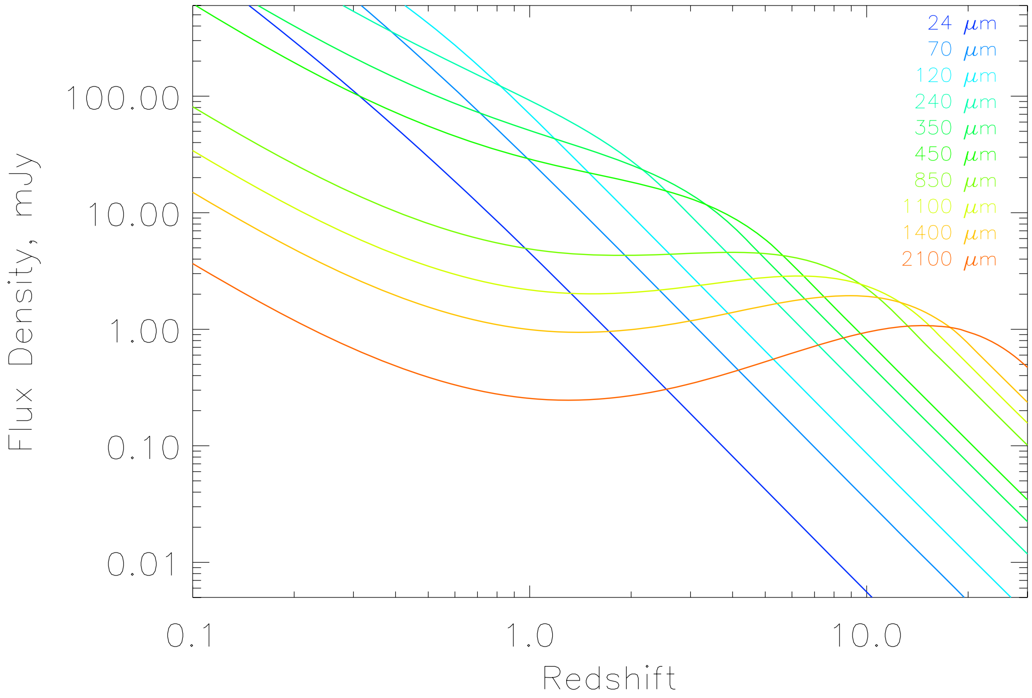

Figure 2.1 Flux density of a submillimeter galaxy as a function redshift for various wavelengths. The modified blackbody spectrum of the galaxy ($L = 5 \times 10^{12} L_{\odot}$, $T =$ 40 K, $\beta = 1.6$, $\alpha =$ -1.7, $\nu_0 =$ 3700 GHz) is based on a composite SED of nearby dusty *IRAS* galaxies, high-redshift submillimeter galaxies, gravitationally lensed high-redshift galaxies, and high-redshift AGNs (Blain et al., 2002, and references therein). The strong negative K-correction in the submillimeter band causes a nearly uniform detection sensitivity over a wide redshift range.

time decreases. A relatively uniform detection sensitivity also requires little evolution in the dust properties of submillimeter galaxies. As the fraction of heavy elements (required to form the dust that absorb and reprocess the optical and UV light) in population II and III stars declines at high redshift, the thermal emission spectrum will begin to evolve. More importantly, submillimeter surveys are highly sensitive to the dust temperature of galaxies, inherently biased against warmer galaxies for a given bolometric luminosity. This effect is due to the steep dependence to luminosity on temperature ($L \sim T^{4+\beta}$), such that if the temperature increases from 30 to 60 K, the luminosity increases by a factor of ~ 50. Conversely, a submillimeter galaxy with a fixed bolometric luminosity and a higher temperature (shifting the peak of the thermal spectrum to higher frequency) will have a much lower submillimeter flux density. Similar (although less significant) selection biases result from submillimeter galaxies with varying dust emissivities (β) and hotter dust components on the Wien side of the spectrum (where $f_\nu \propto \nu^\alpha$).

Despite the absorption of the optical light by dust grains, optical and near-infrared observations are revealing the submillimeter emission to be morphologically complex (e.g., Smail et al., 2002). The large beam sizes of submillimeter instruments ($9''$, $11''$, $14''$ and $31''$ FWHM for SHARC II, MAMBO, SCUBA, and Bolocam, respectively) presents a major obstacle in identifying likely optical and infrared counterparts to the unresolved galaxies. Therefore many follow-up surveys (including spectroscopic observations) are typically limited to submillimeter galaxies with radio counterparts in order to secure precise positions. At least 60% of the radio selected SCUBA submillimeter galaxies show distortion in the optical / infrared, with many showing evidence of being composite systems (red galaxies with relatively blue companions separated by a few arcseconds; Ivison et al., 2002). High resolution HST-STIS imaging of 13 submillimeter galaxies also finds a predominance of irregular and complex morphologies, with 70% extraordinarily large and elongated relative to the field population (Chapman et al., 2003c). These disturbed morphologies are suggestive of merging or interacting systems. Furthermore, comparing these galaxies to optically selected galaxies at $z \sim 2 - 3$ reveals the submillimeter population to be morphologically distinct. Over 50% of the Ivison et al. (2002) sample of galaxies are very red ($I - K > 3.3$) or extremely red ($I - K > 4$), with a large 15 × spread in the infrared fluxes (compared to the 3 × spread in submillimeter flux densities). In fact, comparing submillimeter galaxies with K band counterparts to all galaxies shows that submillimeter galaxies lie along the upper envelope of the general population, being among the reddest objects, independent of magnitude (Webb et al., 2003).

X-ray surveys with ROSAT and XMM-Newton (Lehmann et al., 2001; Mainieri et al., 2002; Ivison et al., 2005) show a small fraction ($\sim 15\%$) of submillimeter galaxies with X-ray counterparts (Ivison et al., 2002). Counterparts are detected at $> 3\sigma$ significance in the hard (2 - 5 keV) bands, but are typically faint or not detected in other energy bands. The deficit of soft X-ray flux may imply the X-ray emission is absorbed by large column densities of dust.

Small survey fields and sparse number counts have made it difficult to ascertain the spatial distribution of submillimeter galaxies. While the clustering properties of submillimeter galaxies remain uncertain, there exists tentative evidence from both two-dimensional angular correlation functions (Greve et al., 2004; Scott et al., 2002; Borys et al., 2003) and clustering analyzed with spectroscopic redshift distributions (Blain et al., 2004) that suggests strong clustering with large correlation lengths (as well as correlation to other classes of high-redshift galaxies, including Lyman break galaxies and X-ray loud AGNs; Almaini et al., 2003). If such associated systems exist, submillimeter galaxies would then trace density regions of the high-redshift universe that could evolve into rich clusters of galaxies at the present epoch.

2.3 Relationship with Other Populations

As resolved images and detailed spectra are limited for the high redshift submillimeter galaxies, we look to well-studied lower redshift galaxies with similar properties to order to gain a better understanding of more distant galaxies. Ultraluminous infrared galaxies (ULIRGs) discovered by the IRAS all sky survey (Sanders & Mirabel, 1996) provide a glimpse into the properties of submillimeter sources. Like submillimeter galaxies, ULIRGs are characterized by extreme bolometric luminosities ($> 10^{12} L_{\odot}$), dominated by dust emission in the mid- and far-infrared. Most ULIRGs, however, are found at low redshift ($z < 0.3$), due mostly to the selection bias of the 8 - 120 μm photometric channels of the IRAS detectors. They are nevertheless rare in the local universe, making up only 0.1% of galaxies by number. Radiative transfer models of the SEDs of the most luminous ($> 10^{13} L_{\odot}$) ULIRGs (those most closely resembling the luminosities of high redshift submillimeter galaxies) show that while most exhibit AGN optical spectra (Sanders, 1999), the bulk of the emission from these galaxies at rest frame wavelengths ≥ 50 μm is caused by $> 10^3$ $\mathrm{M}_{\odot}$ yr^{-1} star formation (Rowan-Robinson, 2000). A starburst of this rate would be sufficient to exhaust the reservoir of gas in a duration of 10^8 yr. Interestingly, while the AGN are not bolometrically important in most cases, the models of Rowan-Robinson (2000) show a correlation between the starburst and AGN luminosities – suggesting a physical link between the triggering of star formation and accretion onto the AGN. Recent X-ray observations and optical spectroscopy of the limited high redshift ($z > 1$) sample of ULIRGS confirm that star formation is the dominant power source of these galaxies, with AGNs accounting for $<$ 20% of the total bolometric output (Alexander et al., 2004).

Submillimeter galaxies may also be related to high redshift Lyman Break Galaxies (LBGs), which share a similar epoch of $z \sim 2 - 3$ (Steidel & Hamilton, 1993). These galaxies, which are preferentially selected at high redshift where the Lyman break shifts into the optical, form one of the largest high-redshift galaxy samples. LBGs are rapidly forming stars and are also thought to be massive enough to be the progenitors of modern day elliptical galaxies (e.g., Weatherley & Warren, 2003). Their SFRs, however, are much lower (7 - 33 $M_\odot$ yr^{-1}; Barmby et al., 2004) than those of typical submillimeter galaxies, and the emission from these young stars makes up little of the LBG mass (Brinchmann & Ellis, 2000). (Their selection criterion of diminished photons from the blue-side of the Lyman limit ensures very few hot, massive stars that produce energetic photons.) Furthermore, the comoving space density of LBGs at high redshift is an order of magnitude higher than that of submillimeter galaxies (Blain et al., 2004). It may be therefore be possible that the LBGs are somehow related to the faintest of submillimeter galaxies, where their number densities (well into the confusion limit) are believed to rise steeply.

Because of their very red nature in the optical and near-IR, is has been proposed that high redshift submillimeter galaxies may somehow be related to the population of extremely red objects (EROs) detected by deep near-IR surveys (e.g., Thompson et al., 1999; Yan et al., 2000). These sources, defined by red near-IR colors ($R - K \gtrsim 5 - 6$ or $I - K \gtrsim 4 - 5$), includes a extragalactic contribution from galaxies (in addition to cool stars, substellar objects, etc...). The resolved sources consist of both 1) very evolved galaxies that contain only old or intermediate, cool, low mass stars, whose K-correction at $z \sim 1 - 2$ produces very red optical and near-IR colors, and 2) dust starburst galaxies strongly reddened by dust in the rest-frame near-UV. The fraction of EROs that fall into the latter group (which closely resemble submillimeter galaxies) has remained largely unknown, although recent detections of the 1.6 stellar bump in EROs with *Spitzer* IRAC, along with dusty starburst 24 μm emission using MIPS, shows that 2/3 of EROs lie at $z \geq 1.3$ and 22% of these are dust starforming galaxies (Wilson et al., 2004). Indeed most radio follow-up observations show little or no radio emission from most EROs, a signature of ongoing starformation from young supernova remnants. Only recently have statistically significant samples of EROs begun to emerge, yielding surface densities of 144 ± 58 deg^{-2} ($R - K > 6$, $K < 19$), similar to that of submillimeter galaxies. The similar comoving density of starforming EROs (Scott et al., 2002), along with a brighter sample of ($K < 19.2$) that has been shown to exhibit strong clustering (Daddi et al., 2000), suggests that EROs ($z \sim 1.5$) may form an evolutionary sequence with submillimeter galaxies at high redshift ($z > 2.5$) and massive elliptical at $z = 0$.

2.4 Redshifts

Photometric redshift that utilize continuum ratios of the far-infrared / submillimeter and radio bands constrain most submillimeter galaxies to lie at $z > 1$ (Carilli & Yun, 1999; Yun, Reddy, & Condon, 2001). This FIR-to-radio correlation is based on semianalytic relationships between the massive star formation rate, the radio synchrotron luminosity, and far-IR dust emission from active star-forming galaxies. The star formation acts as the physical link, with synchrotron radiation resulting from relativistic electrons accelerated in the vicinity of supernova remnants, and the dust heated by the interstellar radiation field. Photometric redshifts fitting only to the modified blackbody spectrum in the submillimeter (Wiklind, 2003) or using the near-IR stellar continuum hump at a rest wavelength of 1.6 μm (Sawicki, 2002) further confirm the high redshift nature of submillimeter galaxies.

Recent observations of submillimeter galaxies with the Keck Low-Resolution Imaging Spectrograph (LRIS; Chapman et al. 2003a, 2003b, 2005) have shown that redshifts can be obtained for ~70% of bright submillimeter galaxies ($S_{850\mu\mathrm{m}} > 5$ mJy) with bright radio counterparts ($S_{1.4\mathrm{GHz}} > 30$ μJy; Blain et al., 2004) (the fraction of submillimeter galaxies with radio counterparts appears to be ~65%; Ivison et al., 2002). This sample of submillimeter galaxies lies in a distribution peaking at $z = 2.4$ with $\Delta z = 0.65$ (Ivison et al., 2002; Chapman et al., 2003b, 2005). Twelve of these galaxies have had their optical spectroscopic redshifts confirmed by millimeter CO line measurements (Greve et al., 2005; Frayer et al., 1998, 1999; Neri et al., 2003; Sheth et al., 2004). This redshift distribution may be biased with respect to the overall submillimeter galaxy population owing to a number of selection effects: the requirement of precise radio positions prior to spectroscopy, which introduces a bias against cooler galaxies, especially at higher redshifts ($z > 2.5$); limited completeness ($\sim 30\%$) of the spectroscopic observations, which biases the sample against galaxies with weak emission lines; and the redshift gap at $z = 1.2 - 1.8$ due to the "spectroscopic desert," in which no strong rest-frame ultraviolet lines are redshifted into the optical.

Chapter 3

Bolocam Instrument

The recent emergence of ground based submillimeter and millimeter wave instrumentation has provided an opportunity to detect and characterize submillimeter galaxies. Advances in bolometer technology with SCUBA, MAMBO, and Bolocam, combined with the construction of large telescopes in high, dry locations has allowed us to achieve diffraction limited resolution with far greater sensitivity than was available only a decade ago. One of the newest generations of millimeter-wave instruments is Bolocam, a bolometer array detector optimized for mapping large fields to faint flux limits at fast scan rates. Achieving this goal requires careful treatment of instrumental and atmospheric noise contributions.

The heart of Bolocam is an array of 144 silicon nitride micromesh ("spider-web") bolometers organized in a hexagonal pattern. The use of a mesh, rather than a solid absorber, both reduces its heat capacity and minimizes its cross-section to high energy particles such as cosmic rays. The entire array is manufactured from a single silicon wafer overlayed with a thin film of silicon nitride. The silicon is subsequently etched away, leaving Si_3N_4 absorbers that are bonded to thermistors.

To eliminate thermal background noise from the instrument itself, the bolometer array is enclosed within a cryogenic dewar and cooled to 260 mK using LN_2 (77 K), LHe_4 (4.2 K) and a three-stage ($^4He/^3He/^3He$) sorption refrigerator. The dewar itself is placed under vacuum to minimize thermal conductivity of the air, with each cold stage thermally isolated using G-10 fiberglass and Vespel standoffs.

An array of close-packed ($1.5f\lambda$), straight-walled conical feed horns terminating in cylindrical waveguides and integrating cavities formed by a planar backshort couples the bolometers to cryogenic and room-temperature optics. The instrument is mounted at the Cassegrain focus of the Caltech Submillimeter Observatory (CSO) on Mauna Kea. The illumination on the 10.4 m diameter CSO primary mirror is controlled by the combination of the feed horns and a cold (6 K) Lyot stop, resulting in $31''$ beams (FWHM at 1.1 mm) and an $8'$ field-of-view. The use of the Lyot stop to apodize the beam significantly reduces warm loading from the beam sidelobes at the expense of slightly compromising angular resolution. (The illumination of the central 8.5 m of the CSO mirror makes the $31''$ instrument resolution diffraction limited.) A stack of resonant metal-mesh filters form the passband in conjunction with the waveguides. The two available bandpasses are centered on 1.1 and 2.1 mm, with one bandpass available per observing run. The $\lambda = 2.1$ mm configuration is used for observations of the Sunyaev-Zel'dovich effect and secondary anisotropies in the cosmic microwave background radiation. Technical details of Bolocam are given in Glenn et al. (1998, 2003) and Haig et al. (2004); numerical simulations of the integrating cavities are described in Glenn et al. (2002).

A key element of Bolocam is the bolometer bias and readout electronics: an AC biasing scheme (130 Hz) with readout by lock-in amplifiers enables the detectors to be biased well above the $1/f$ knee of the electronics. The electronic readout stability, in conjunction with Bolocam's rigorous sky noise subtraction algorithm, eliminates the need to nutate the CSO subreflector. Another advantage of this AC biasing scheme is that it is easy to monitor the bolometer operating voltage; these voltages are determined by the total atmospheric emission in the telescope beam and the responsivity of the bolometers. Thus, a voltage that is a monotonic function of the in-band atmospheric optical depth and bolometer responsivity is continually measured. Sky subtraction is implemented by either a subtraction of the average bolometer voltages or a principal component analysis (PCA) technique, which is described below.

Chapter 4

Observations

Two sets of observations of the Lockman Hole East (R.A. = $10^{\rm h}\,52^{\rm m}\,08^{\rm s}.82$, decl. = $+57^\circ\,21'\,33''.80$, J2000.0) were made with Bolocam: 2003 January, when the data were taken with a fast raster scan without chopping (hereafter referred to as raster scan observations), and 2003 May, when the data were acquired with a slow raster scan with chopping as a test of this observing mode (referred to as chopped observations). Approximately 82 hr of integration time over 17 nights were obtained on the field during 2003 January, resulting in 259 separate observations, and 41 hr over 19 nights were obtained in 2003 May, resulting in 64 separate observations. The weather was generally good during the 2003 January run and mediocre to poor during the 2003 May run, where we characterize the weather quality by the sky noise variability (rapid variability of the optical depth).[1] One hundred and nineteen bolometer channels were operational during 2003 May; however, only 89 bolometer channels were used in the analysis of the 2003 January data. (The remaining bolometers were not included in making the final Lockman Hole map because of excess noise and/or electronics failures.) Nominally one feed horn per hextant is blocked to enable these dark bolometers to be used for bias and noise monitoring. The 2003 May chopped observations were not deep enough to detect galaxies individually at $> 3\ \sigma$ and were used only for pointing verification by

---

[1] Another weather measurement influencing the Bolocam mapping speed is the CSO 225 GHz heterodyne, narrowband, "tipper tau" monitor, which measures the zenith atmospheric attenuation. The 2003 January and May Lockman Hole observations yielded $\tau_{225\rm GHz}$ ranges and 75th percentiles of $\tau_{225\rm GHz} = 0.028 - 0.129$, $\tau_{75\%} = 0.083$ and $\tau_{225\rm GHz} = 0.014 - 0.307$, $\tau_{75\%} = 0.200$, respectively.

cross-correlation with the raster scan observations.

During 2003 January, observations were made by scanning the telescope at $60'' \text{ s}^{-1}$ in right ascension and stepping in declination by $162''$ ($\sim \frac{1}{3}$ of a field of view) between subscans (defined as a single raster scan across the sky at a fixed declination) to build up the map. Subsequent scans (which we define as the set of subscans needed to cover the entire declination range of the field) were taken with a $\pm 11''$ jitter for each $162''$ step to minimize coverage variations. Combined with a 5° tilt of the bolometer array relative to azimuth and a fixed Dewar angle, such that the rotation relative to scan direction varies over the night, this yielded even coverage and sub-Nyquist sampling in the cross-scan direction (declination). Sub-Nyquist sampling was automatically achieved in the in-scan direction (right ascension) with 50 Hz sampling of the lock-in amplifiers. In 2003 May, the chopped observations were made with raster scans in azimuth and steps in elevation, but with a scan rate of $5'' \text{ s}^{-1}$ and a symmetric chopper throw of $\pm 45''$ in azimuth, with frequencies of 1 and 2 Hz.

A coverage map of the Bolocam Lockman Hole East field from 2003 January is shown in Figure 4.1, where the integration time per $10'' \times 10''$ pixel is shown. Bolocam's $8'$ field of view is not small compared to the map size; thus, there is a large border around the map where the coverage is reduced and nonuniform compared to the central region. Hence, we define a "uniform coverage region" of 324 arcmin^2 in the center where the rms in the integration time per pixel is 12%. Because rms noise varies as the square root of the integration time, the noise dispersion is approximately 6% in the uniform coverage region (2% after the map has been optimally filtered as discussed in § 5.5). Our analysis is confined to the uniform coverage region. The observational parameters are summarized in Table 4.1.

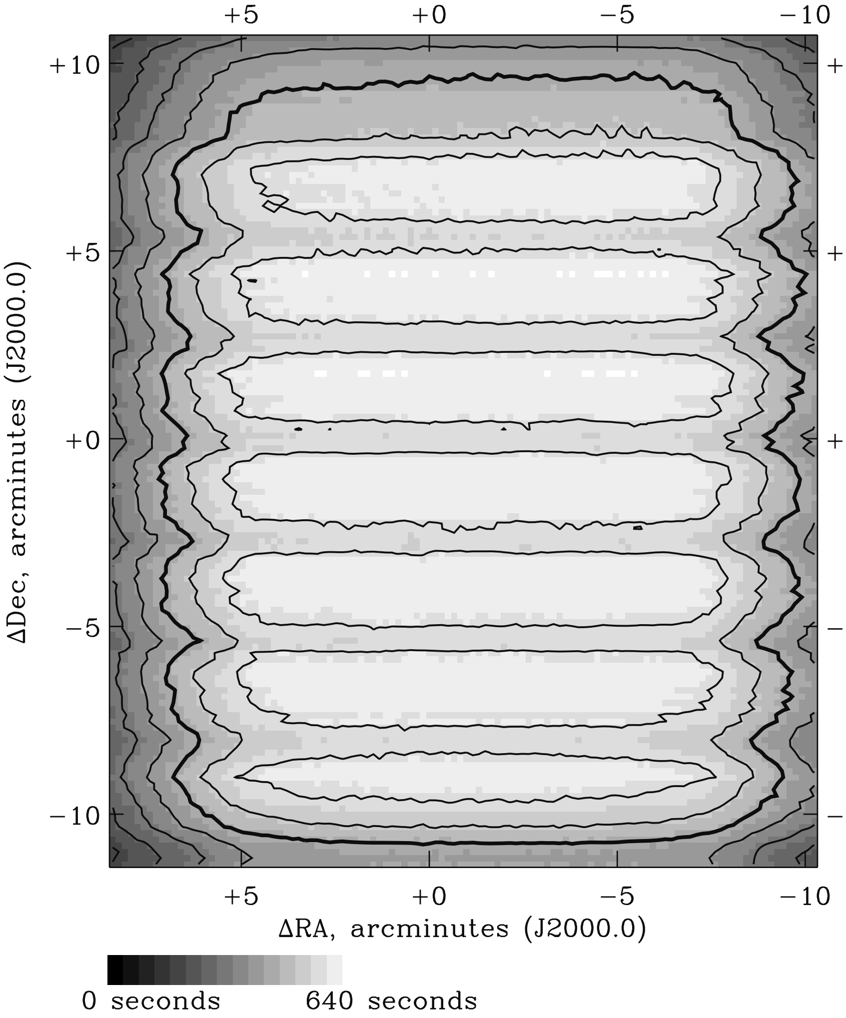

Figure 4.1 Coverage map of the Lockman Hole East, pixelized at 10″ resolution. White corresponds to the highest level of coverage and black to the lowest level of coverage; the contours are 193, 257, 322, 386, 450, 515, and 579 s of integration time per pixel. The "uniform coverage region" corresponds to the thick contour at 450 s pixel^{-1}.

Table 4.1. Observational Parameters

Quantity	Value
Field of View	$8'$
Beam Size (FWHM)	$31''$
1.1 mm Band Center	265 GHz
Bandwidth	42 GHz
Raster Scan Speed[a]	$60''$ s^{-1}
Chopped Observation Scan Speed[b]	$5''$ s^{-1}
Chopper Throw[c]	$90''$
Subscan Step Size	$162''$
Subscan Substep Size	$\pm 11''$

[a] Raster scans were scanned in right ascension with steps between subscans in declination.

[b] Chopped observations were scanned in azimuth with steps between subscans in elevation.

[c] For chopped observations only.

Chapter 5

Data Reduction

5.1 Basic Pipeline

The Lockman Hole observations were reduced with a custom IDL-based software pipeline. The raw files were cleaned with a PCA sky subtraction, where an atmospheric and instrumental noise template was generated through an eigenvector decomposition of the time stream data (§ 5.2). In the case of the chopped observations, which are characterized by both positive and negative beams, the time streams were first demodulated followed by a convolution with the expected source crossing structure (first the positive beam, then the negative beam). This results in a positive net peak at the nominal source position with the full source amplitude and symmetric negative beams with half the source amplitude.

Once the cleaned time streams were obtained, a map was generated by co-adding individual time streams, weighted by their power spectral densities (PSDs) integrated over the spectral response to a point source. Pointing offsets were applied to individual observations from the global pointing model generated from observations of submillimeter pointing sources (§ 5.3). Time streams were calibrated from lock-in amplifier voltages to millijanskys using observations of primary and secondary flux calibrators (§ 5.4). The final map was generated in right ascension and declination using sub-beam-sized pixelization (§ 5.5) and Wiener filtered to maximize signal-to-noise ratio (S/N) for detections of point sources.

5.2 Cleaning and Sky Subtraction

To facilitate removal of fluctuating atmospheric water vapor emission (sky noise) from the bolometer signals, Bolocam was designed such that the feed horn beams overlap maximally on the primary mirror of the telescope and therefore sample very similar columns of atmosphere. Thus, the sky noise, which dominates the fundamental instrument noise by a factor of $\sim$100, is a nearly common-mode signal. To remove this correlated $1/f$ noise with maximum effectiveness, a PCA technique was developed. The formalism of the PCA analysis is standard (see, e.g., Murtagh & Heck, 1987) and complete details of its implementation can be found in Appendix A. In summary, the covariance matrix is built from the n bolometers by m time elements matrix for each subscan. Eigenfunctions of the orthogonal decomposition that have "large" eigenvalues, corresponding to large contributions to the correlated noise, are nulled and the resulting functions are transformed back into individual bolometer time streams. This technique is applicable for the dim ($\lesssim$10 mJy) submillimeter galaxies of the Lockman Hole (and other blank-field surveys) because the source signal contributes negligibly to the sky templates and is largely uncorrelated from bolometer to bolometer. The PCA technique is not appropriate for extended sources, however, in which case the bolometers see correlated astrophysical signals, which are then attenuated. The PCA decomposition was applied to raster scan and chopped data, after chop demodulation in the latter case. Cosmic-ray strikes (spikes in the time streams) are flagged and not included in constructing the eigenfunctions.

The precise level of the cut on the large eigenvalues is somewhat arbitrary. The greater the number of eigenfunctions that are nulled, the lower the resulting noise in the cleaned time stream, but the correspondingly greater source flux density removed. Empirically, an iterative cut with the nulling of eigenfunctions with eigenvalues $> 3\ \sigma$ from the mean of the eigenvalue distribution produced a balance between sky emission removal and source flux density reduction in simulated observations by maximizing the S/N. Because the distribution of eigenvalues for each observation is characterized by a few outliers (typically $4-7$) at large σ-values, the overall variance of the time stream is largely dominated by these eigenvalues, resulting in a S/N that is insensitive to the cut threshold for $2-5\ \sigma$. Furthermore, the distribution of source candidates in the combined Lockman Hole map was invariant under variations in the cut threshold in this range.

The PCA sky subtraction attenuates the signal from point sources in addition to the atmospheric signal because it removes low-frequency power from the time streams. The amount of flux density attenuation is determined by the number of PCA components that are removed from the raw time streams, which is controlled by the cut on the eigenvalues: a more aggressive cut results in greater attenuation. Monte Carlo simulations were done to determine the amount by which the flux density of galaxy candidates was reduced by the cleaning. The simulations were done in the following manner: A fake source (Gaussian, $31''$ FWHM) was injected into a blank Lockman Hole map. A simulated bolometer time stream was generated from the map of the fake source and was added to the raw bolometer time streams of an individual Lockman Hole observation. The time stream data were then cleaned with PCA and mapped in the ordinary manner. The resulting source was fitted by a two-dimensional Gaussian to determine the attenuation of the injected source flux density. This simulation was repeated 1014 times with fake sources injected into random observations at random positions and ranging in flux density from 0.1 to above 1000 mJy (Fig. 5.1). The average reduction in flux density is 0.19 with an rms dispersion of 0.04, independent of flux density to 1 Jy.

Above 1 Jy, typical for bright pointing and flux calibrators, the amount of attenuation by PCA was found to depend on the brightness of the fake source. Thus, a different cleaning technique was used for these sources. An atmospheric noise template was generated by simply taking an average of all n bolometers for each time element. The

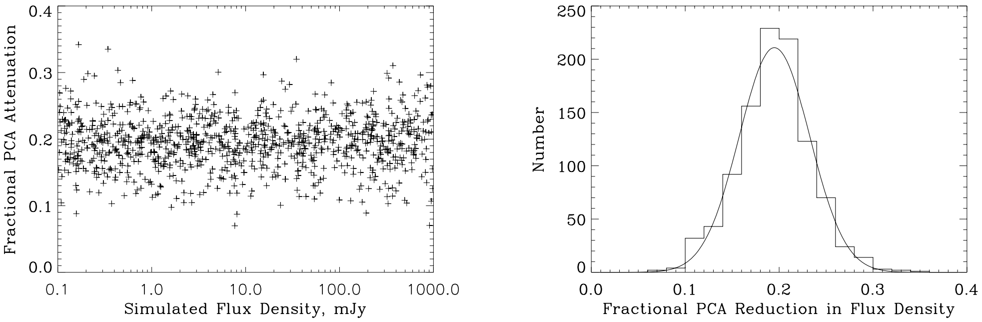

Figure 5.1 Source attenuation by PCA cleaning as a function of injected flux density (*left*) and histogram with Gaussian fit (*right*). Sources were injected into the raw time streams, which were then cleaned using the PCA. The resulting source amplitudes were compared to the injected source amplitudes (their ratio is the fractional reduction in source flux density). The attenuation of sources by PCA is 19% with a dispersion of 4%, independent of flux density from 0.1 mJy to 1 Jy.

mean-subtracted sky template was then correlated to each of the individual bolometer time streams and the correlated component was subtracted. To prevent the correlation coefficient from being contaminated by the calibrators, multiple scans (including telescope turnaround time between scans) were concatenated and used together to correlate the average sky template to each individual bolometer signal, thus ensuring a small contribution from the point source. A similar analysis to that for PCA flux reduction was performed for the simple average sky subtraction technique, yielding an average flux density reduction of 0.07, independent of source flux, with an rms dispersion of 0.02.

5.3 Pointing

Observations of planets, quasars, protostellar sources, H_{II} regions, and evolved stars were used to construct separate pointing models for the 2003 January and May observing runs. Observations of the pointing sources were taken at the same scanning speeds as the Lockman Hole observations. The pointing fields were generally small (scan areas of $\sim 4'$x$4'$), although several larger maps ($10'$x$10'$) were made of Mars so that the source would pass over the entire bolometer array for measuring relative responsivities and beam maps. Pointing observations are generally small because source crossings are only needed in a small subset (15 or so) of bolometers to determine the pointing offsets. These observations were used to map and correct the distortion over the field of view, which is in broad agreement with the distortion predicted by a Zemax® ray-tracing model. The residual rms in the raster-scanned pointing model for the ensemble of all 2003 January sources is $9.1''$, although the local pointing registered to a nearby pointing source is superior.[1] This random pointing error results in an 18% flux density reduction of the Lockman Hole galaxy candidates (analytically derived from a convolution of the $31''$ Bolocam beam with a $9.1''$ Gaussian random pointing error), which is corrected for in the reported flux densities (and uncertainties in these fluxes) of Table 6.1.

---

[1] A subsequent pointing model for a localized region of sky yields an rms of $4.5''$.

While the 2003 January pointing observations were used to construct a pointing model that was applied to the entire sky, the region of the celestial sphere near the Lockman Hole was not well sampled. A pointing correction derived from sources far away ($> 30^\circ$) from the Lockman Hole is therefore susceptible to a systematic offset. Pointing observations were made much more frequently (once per hour) during the 2003 May run and sources near the Lockman Hole were emphasized to create an improved local pointing model; consequently, the 2003 May pointing model near the Lockman Hole was superior to the 2003 January pointing model. No galaxy candidates were detected at $\geq 3\ \sigma$ significance in the 2003 May chopped Lockman Hole map owing to poor weather; however, it was cross-correlated with the 2003 January map to compare the pointing models. The cross-correlation yielded a shift of $25''$ in right ascension of the 2003 January data with respect to the 2003 May data (Fig. 5.2). Because the pointing on the sky near the Lockman Hole was substantially better and more frequently sampled for the 2003 May run, we attribute this shift to a systematic offset in the 2003 January pointing model. Thus, a systematic $25''$ shift in right ascension was applied to the 2003 January Lockman Hole map. The need for the shift is also apparent in a comparison between the Bolocam map and the 8 mJy SCUBA 850 μm and MAMBO 1.2 mm surveys, as several of the Bolocam galaxy candidates become coincident with SCUBA and MAMBO sources in the overlap region of the surveys.

Because no pointing observations were taken near the Lockman Hole, it is difficult to quantify the uncertainty in the $9.1''$ pointing rms. An independent measurement of our pointing uncertainty was performed by examining both 10 VLA[2] radio positions coincident with Bolocam Lockman Hole galaxy candidates and the subset of 5 sources with additional SCUBA and/or MAMBO counterparts (see § 6.3). The rms errors between the Bolocam and radio positions are $10.2^{+3.1}_{-2.4}$ and $9.3^{+4.4}_{-3.0}$ arcsec for the entire

---

[2] The National Radio Astronomy Observatory is a facility of the National Science Foundation operated under cooperative agreement by Associated Universities, Inc.

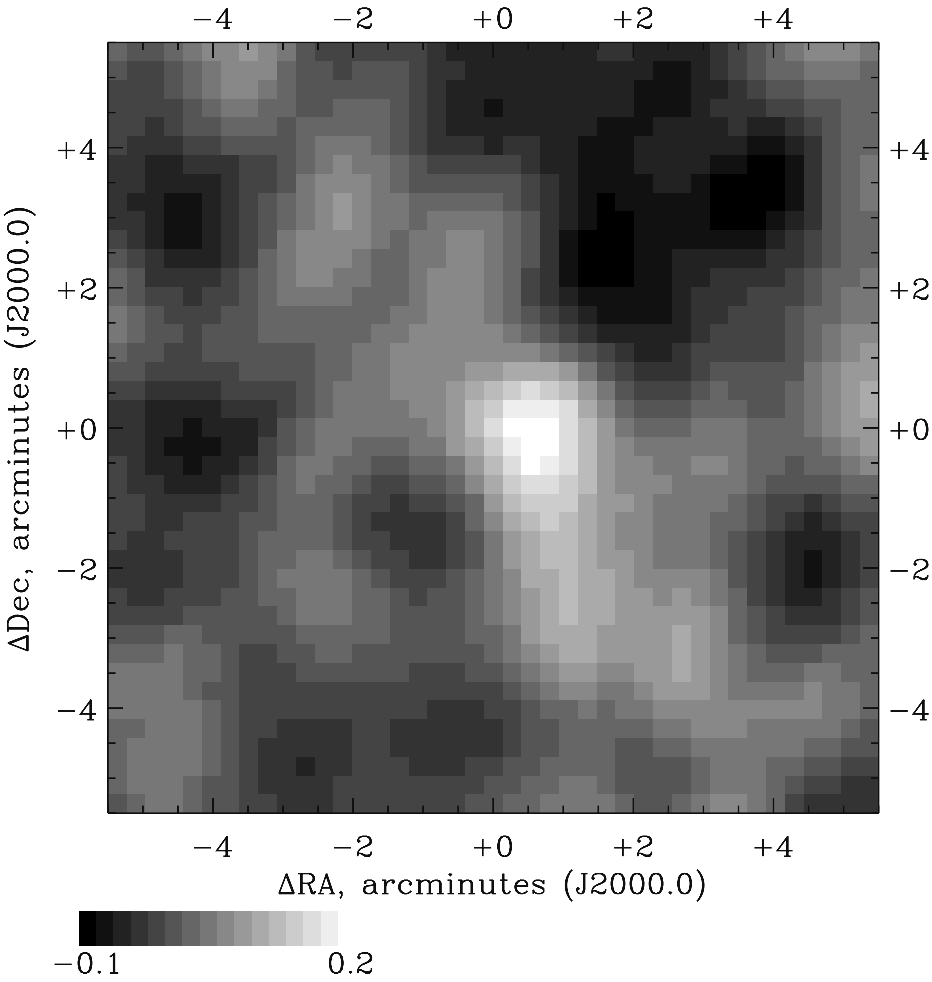

Figure 5.2 Cross-correlation of the 2003 January and May Lockman Hole maps, pixelized at 10″ resolution. While the weather was too poor during the 2003 May observations to yield any $> 3\ \sigma$ detections, the local pointing near the Lockman Hole was sampled substantially better than for the 2003 January run. The 25″ pointing offset corresponding to the peak in the cross-correlation map was subsequently applied to the 2003 January data.

10-source sample and 5-source subset, respectively. The quoted uncertainties are the minimum length 90% confidence intervals for 10 and 5 degrees of freedom (for both $\delta_{\mathrm{R.A.}}$ and $\delta_{\mathrm{decl.}}$, each of which independently determines the pointing error), respectively.

5.4 Flux Calibration

Observations of primary calibrators (planets) and secondary calibrators (protostellar sources, H_{II} regions, and evolved stars) were used for flux calibration (see Appendix B for details). Reference planetary flux densities were obtained from the James Clerk Maxwell Telescope (JCMT) calibration Web site,[3] and flux densities of secondary calibrators were obtained from JCMT calibrators (Sandell, 1994; Jenness et al., 2002). The flux density of IRC +10216 is periodic; the flux density was adjusted to the epoch of observation using the 850 μm SCUBA phase. The reference flux densities were corrected for the Bolocam bandpass, which is centered at 265 GHz (the flux densities in the Bolocam band are 5% larger than the those quoted by the JCMT for the SCUBA 1.1 mm band). During 2003 January, Saturn had a semidiameter of $10''$; this is not small compared to the $31''$ Bolocam beam, so corrections for the angular extent of Saturn were required.

The standard technique for flux calibration is to calibrate a given science observation using the flux calibrator observations taken nearest in time, which were presumably taken at similar atmospheric opacity and air mass. With Bolocam, we are able to use a more sophisticated technique via continuous monitoring of the bolometer operating resistance using the DC level of the lock-in amplifier output signal. The technique uses the following logic. The atmospheric optical loading increases as the atmospheric optical transmission decreases, which may occur because of changes in zenith opacity (i.e., weather) or intentional changes in telescope elevation. The bolometer resistance decreases monotonically as the atmospheric optical loading increases. Simultaneously, the

---

[3] See http://www.jach.hawaii.edu/jac-bin/planetflux.pl.

bolometer responsivity decreases monotonically as the bolometer resistance decreases. Thus, the flux calibration (in nV Jy^{-1}, where the voltage drop across the bolometer is proportional to its resistance), which is proportional to the product of atmospheric transmission and bolometer responsivity, is expected to be a monotonic function of the bolometer resistance. This relation is measured empirically, as shown in Figure 5.3, by plotting the flux calibration (voltage at the bolometer in nV Jy^{-1} of source flux) from each of the ensemble of calibrator observations against the median DC lock-in amplifier voltage measured during the observation. This relation is then combined with the continuously monitored DC lock-in signal to apply the appropriate flux calibration value during science observations. Note that the curve is measured only using sources dim enough to ensure linear bolometer response; Jupiter was dropped for this reason.

The flux density calibration derived from Figure 5.3 is biased relative to the blank-field sources by the combination of three effects: reduction in the flux density of calibration sources due to average cleaning, reduction in the flux density of blank-field sources due to PCA cleaning, and reduction in the flux density of blank-field sources due to pointing errors. The first two effects cause the calibration curve of Figure 5.3 to be shifted up by the factor $\epsilon_{\mathrm{avg}}/\epsilon_{\mathrm{PCA}}$, where the flux reduction factors ϵ_{avg} and ϵ_{PCA} are as determined in § 5.2. The effect of Gaussian random pointing errors of rms σ_p on the peak flux density of a source observed with a Gaussian beam of width σ_b is equivalent to a convolution of the beam with a Gaussian of rms σ_p. The resulting reduction in peak height can be analytically calculated as

$$\epsilon_p = \frac{\sigma_b}{\sqrt{\sigma_b^2 + \sigma_p^2}} = 0.82^{+0.09}_{-0.12}$$

for a $31''$ FWHM beam and a random pointing error of $9.1''$. The uncertainty quoted for ϵ_p is the minimum length 90% confidence interval obtained from the rms pointing error between the Bolocam galaxy candidates and coincident radio sources (see § 6.3). (While the local pointing observations around a specific altitude and azimuth are clustered,

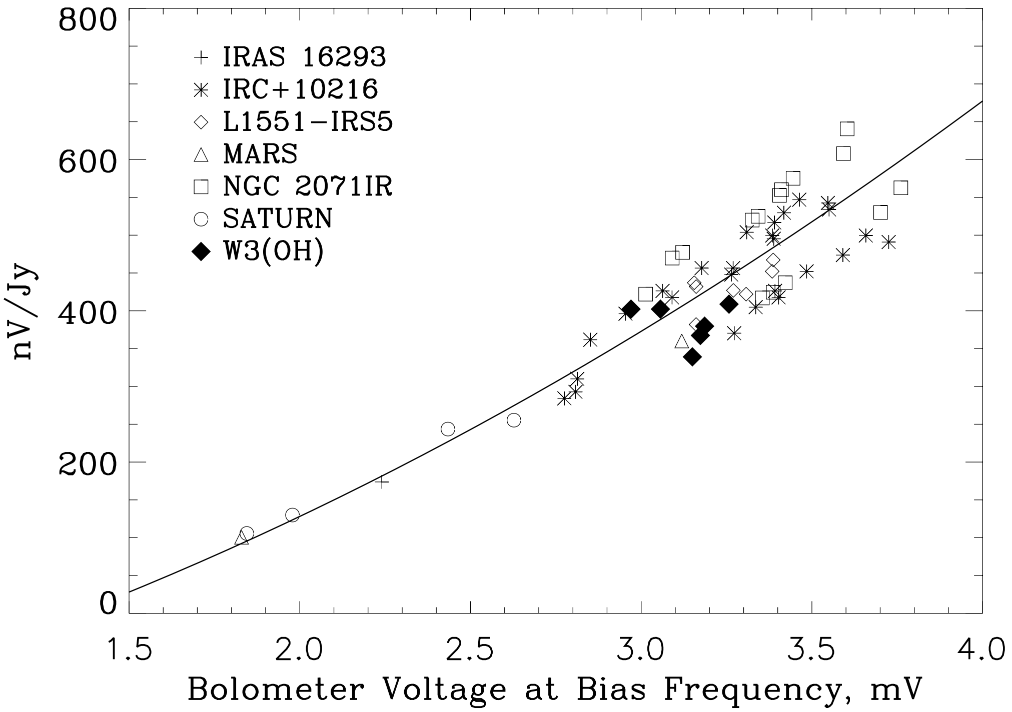

Figure 5.3 Calibration in nV Jy^{-1} (nV at the bolometer) as a function of the demodulated lock-in voltage at the AC bias frequency, which is approximately inversely proportional to the bolometer loading. The quadratic fit is a minimization of the fractional error between observed and expected flux densities. The rms of the residual dispersion in flux density is 9.7%.

each with a smaller pointing error rms, the Lockman Hole observations were taken over a large range of zenith and azimuthal angles and thus have an overall pointing error defined by the ensemble of pointing observations.)

Thus, the final bias in flux density is

$$\epsilon = \frac{\epsilon_p \epsilon_{\mathrm{PCA}}}{\epsilon_{\mathrm{avg}}} = 0.71^{+0.08}_{-0.10}.$$

All flux densities (as well as uncertainties in these fluxes) quoted in this paper, including the simulations of § 7, have been corrected for this flux bias. The uncertainty in the flux bias is a systematic effect that produces a correlated shift in all source fluxes.

5.5 Mapping and Optimal Filtering

Bolocam maps are built up by co-adding subscans weighted by their time stream PSDs integrated over the spectral (temporal frequency) band of a point source at the raster scan speed (see Appendix C for details). Data points were binned into $10'' \times 10''$ pixels, with approximately 30,000 hits per pixel. Each hit represents a 20 ms integration per bolometer channel. Four maps were created: a coverage map with the number of hits per pixel (Fig. 4.1); the PCA-cleaned, optimally filtered astrophysical map; a coverage-normalized map; and a within-pixel rms map. In the coverage-normalized map, each pixel was multiplied by the square root of the number of hits (effectively the integration time) in that pixel to account for the nonuniform coverage in the map when comparing pixels. The dispersion of the bolometer voltages (from each of the hits) within each pixel was recorded in the within-pixel rms map.

Because the signal band of interest (point sources) does not fall throughout the entire temporal (or spatial) frequency range of the PSD of the data, we filter the co-added map with an optimal (Wiener) filter, $g(q)$, to attenuate $1/f$ noise at low frequencies and high-frequency noise above the signal frequency:

$$g(q) = \frac{s^*(q)/J(q)}{\int |s(q)|^2/J(q) d^2q}, \tag{5.1}$$

where $J(q)$ is the average PSD, $s(q)$ is the Fourier transform of the Bolocam beam shape from map space to spatial frequency $(1/x)$ space, q, and the asterisk indicates complex conjugation. The factor in the denominator is the appropriate normalization factor so that when convolved with a map, peak heights of beam-shaped sources are preserved. $J(q)$ is obtained by transforming the time stream PSDs (averaged over all of the Lockman Hole observations) to a spatial PSD assuming azimuthal symmetry. A two-dimensional map of equation (5.1) was thus convolved with the co-added map to maximize S/N for detections of point sources. An analogous filter was applied directly to the demodulated time streams of the chopped observations, with $s(t)$ represented by a positive and negative beam separated by the chop throw ($90''$).

The cleaned, co-added, optimally filtered map is presented in Figure 5.4. There is a perimeter a few arcminutes wide around the map that does not lie within the uniform coverage region (cf. Fig. 4.1). There are 17 galaxy candidates at $> 3\ \sigma$, apparent as unresolved bright spots, numbered in order of decreasing brightness. Six false detections are expected from simulations (discussed in detail in § 7). There are no negative sidelobes associated with the source candidates because the observations are not chopped. The 850 μm SCUBA 8 mJy (Scott et al., 2002) and 1.2 mm MAMBO (Greve et al., 2004) surveys cover patches with radii of $\sim 5'$ and $\sim 7'$ in the center of the map (central 122 and 197 arcmin^2, respectively). A comparison of the maps is given in § 6.

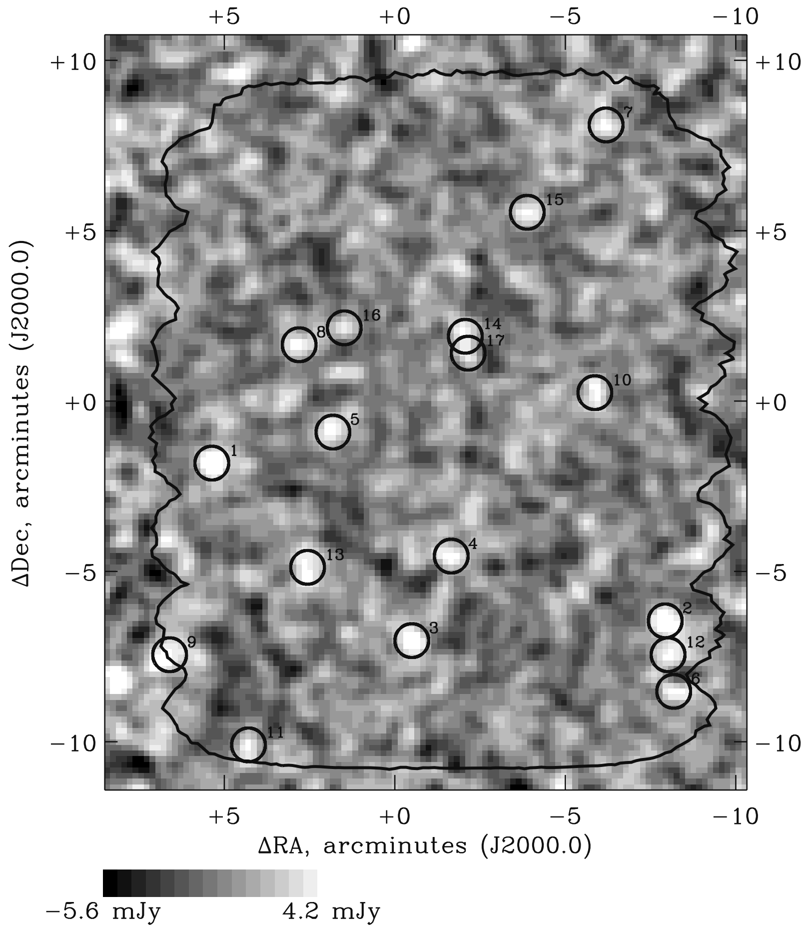

Figure 5.4 Bolocam map of the Lockman Hole East. The field is centered on R.A. = $10^{h}52^{m}08^{s}.82$, decl. = $+57°21'33''.80$ (J2000.0). The map pixels are $10''\times10''$ and the map rms is 1.4 mJy. The uniform, high-coverage region of the map is the inner 324 arcmin^2. This map has been cleaned and optimally filtered for point sources. The 17 Bolocam sources detected at $> 3\ \sigma$ are indicated by thick circles. The bright spot at +8', -8' is not listed as a detection because it falls outside of the uniform coverage region (*black contour*).

Chapter 6

Source List

6.1 Source Extraction

Source extraction was performed on the PCA-cleaned, optimally filtered, coverage-normalized map consisting of all the raster scan observations co-added together. The algorithm was begun by doing a cut on the uniform coverage region, defined as the set of those pixels for which (1) the coverage is $\geq 70\%$ of the maximum per pixel coverage and (2) the within-pixel rms is less than 2 σ from the mean within-pixel rms. The uniform coverage region is a contiguous region in the center of the map.

Next, an rms in sensitivity units (the flux density of each pixel times the square root of the integration time for that pixel in units of mJy $\mathrm{s}^{1/2}$) was computed in the uniform coverage region. This rms is valid for the entire uniform coverage region since variations in coverage have been accounted for by the $t_i^{1/2}$ coverage normalization, where t_i is the total integration time for pixel i. All pixels with coverage-normalized flux densities exceeding 3 σ ("hot pixels") were flagged as potential sources. Then hot pixels were grouped into multi-pixel sources by making the maximal group of adjacent hot pixels, including those within $\sqrt{2}$ pixels (i.e., diagonally adjacent). The right ascension and declination of the source candidates were computed by centroiding two-dimensional Gaussians on the groups. Because convolution of the map with the Wiener filter properly weights the flux contribution from each pixel, the best estimate of the source flux density in the optimally filtered map is given by the peak value in the group.

A histogram of the pixel values in the uniform coverage region is shown in Figure 6.1. The quantity that is plotted is the pixel sensitivity, with the scaling by $t_i^{1/2}$ accounting for the nonuniform coverage in the map. Note that the sensitivity histogram should not be interpreted as instrument sensitivity as the histogram uses an optimally filtered (smoothed) map but scales by sub-beam-sized integration times. The negative side of the histogram, plotted logarithmically, is extremely Gaussian. A Gaussian fit to the Bolocam noise-only (jackknife) distribution is overplotted by a solid line (see § 6.2), indicating a clear excess on the positive side with respect to the Gaussian. The galaxy candidates make up this excess. Since the pixels are $10'' \times 10''$ in size and the beam size is 0.30 arcmin^2, there are approximately 11 pixels per source candidate.

The source candidate list is presented in Table 6.1, where the flux densities are listed in order of decreasing brightness in the fifth column. Seventeen galaxy candidates were detected at $> 3\ \sigma$ significance, with the brightest being 6.8 mJy. Seven of the candidates were detected at $> 3.5\ \sigma$ significance. The flux densities of the source candidates were attenuated by the PCA cleaning; their corrected flux densities are listed (see § 5.2). The source candidate list is compared to the 850 μm SCUBA 8 mJy and 1.1 mm MAMBO surveys in § 6.3.

6.2 Tests for Robustness of Galaxy Candidates

Two tests were carried out to check the robustness of the galaxy candidates. The first test was a jackknife test in which 50% of the observations were randomly chosen and co-added together into a map and the remaining 50% of the observations were co-added into a second map. If the source candidates are real and coherent over multiple observations, then the positive-side excess of the histogram in Figure 6.1 should disappear when the two maps are differenced. Conversely, if the source candidates arise from spurious events in individual observations, such as cosmic-ray strikes, then the excess would not disappear when the two maps are differenced. This algorithm was repeated 21 times

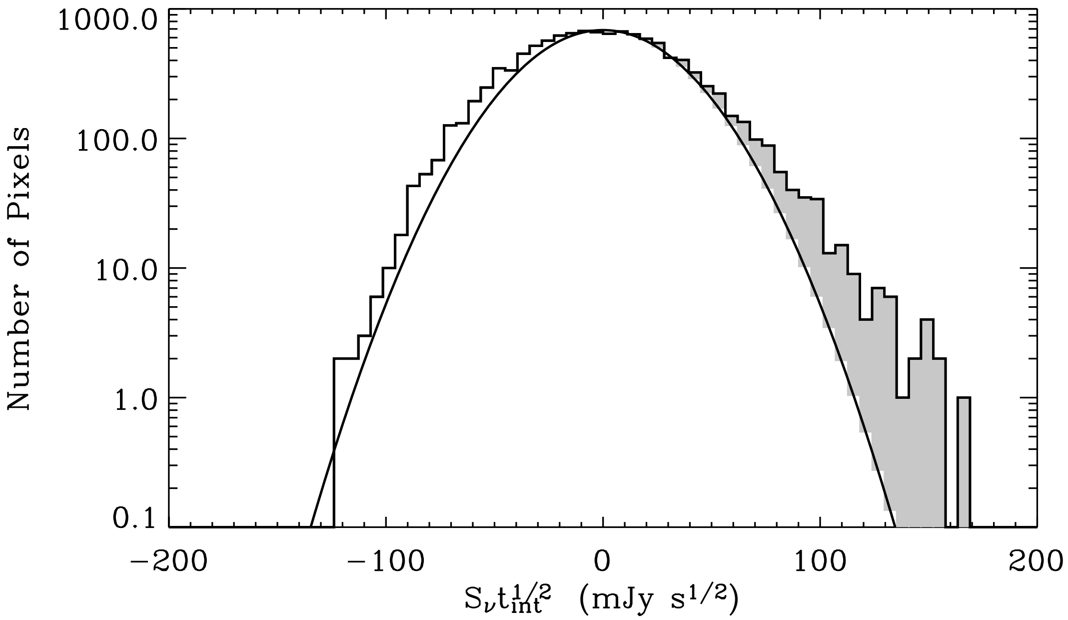

Figure 6.1 Histogram of the pixel sensitivities, defined as the pixel flux density, S_ν, times the integration time per pixel, $t_{int}^{1/2}$. The solid line is a Gaussian fit to the jackknifed histogram of Fig. 6.2. The shaded area indicates the emission due to galaxy candidates in excess of that expected from map noise. The negative side of the histogram is slightly broader than the fit to the jackknifed histogram owing to the presence of the galaxies (confusion noise) on both the positive and negative side. The small negative offset of the peak of the distribution is expected, as the mean of the entire map (and therefore the histogram) is constrained to have mean zero from both the high-pass filter in the Bolocam electronics and sky subtraction.

Table 6.1. Galaxy Candidates

Source	R.A. (J2000.0)	decl. (J2000.0)	S/N	Corrected S_ν	Corrected σ
1	10:52:55.5	57:21:03	5.0	6.8	1.4
2	10:51:16.7	57:16:33	4.8	6.5	1.4
3	10:52:12.2	57:15:53	4.5	6.0	1.4
4	10:52:03.6	57:18:23	4.0	5.2	1.4
5	10:52:29.5	57:22:03	3.9	5.1	1.3
6	10:51:15.6	57:14:23	3.5	5.0	1.5
7	10:51:30.0	57:31:03	3.4	4.9	1.5
8	10:52:37.0	57:24:33	3.7	4.8	1.3
9	10:53:05.2	57:15:23	3.1	4.8	1.5
10	10:51:31.4	57:23:13	3.5	4.7	1.4
11	10:52:48.0	57:12:43	3.2	4.6	1.5
12	10:51:15.5	57:15:23	3.2	4.6	1.4
13	10:52:35.7	57:17:53	3.3	4.5	1.4
14	10:52:01.1	57:25:03	3.3	4.4	1.3
15	10:51:47.4	57:28:33	3.2	4.4	1.4
16	10:52:27.1	57:25:13	3.1	4.1	1.4
17	10:51:59.9	57:24:23	3.1	4.0	1.3

Note. — Units of right ascension are hours, minutes, and seconds, and units of declination are degrees, arcminutes, and arcseconds.

with the first 50% of the observations randomly selected independently each time, and the histograms were averaged. For such an algorithm, one expects the noise realizations to be approximately independent; the actual correlation was measured to be ~4%. The result is shown in Figure 6.2. A Gaussian distribution fits the jackknife histogram extremely well. The absence of a positive-side excess indicates that the source candidates in the Wiener-filtered map common to all observations. The negative side of the real map histogram (cf. Fig. 6.1) is slightly broader because confusion noise from sources below our threshold is absent in the jackknife histogram. Similar histograms result from jackknife tests of scan direction (+R.A. vs. -R.A.), intranight variations (cuts on local sidereal time), and night-to-night variations, indicating that the galaxy candidates are not caused by systematic effects, such as scan-synchronous or elevation-dependent noise. This strong statistical test indicates that the Bolocam source candidates are real.

A second test was performed to verify that the source candidates arise from the co-addition of many observations rather than from spurious events. In this test, individual maps were made from each of the 259 observations. These maps were then co-added with fixed-amplitude offsets with random directions (phases). The expectation of this null test is that sources coherent over multiple observations are smeared out onto rings of a fixed radius, resulting in the disappearance of the positive-side excess. (The positive-side excess will be distributed over many pixels and therefore spread over many bins of the histogram.) Source candidates arising from isolated spurious events or characterized by length scales much larger than the Bolocam beam will merely be moved or negligibly broadened, leaving the histogram unchanged. Sixteen iterations were performed at each jitter amplitude ranging from $15''$ to $70''$ (Fig. 6.3). The rms of the jittered histograms in excess of the rms of the jackknife distribution of Figure 6.2 continues to decline out to a random jitter of $70''$. The excess does not go to zero at large amplitudes because the sources are spread out onto annuli with finite radii and will still be present at a low level. Since the area of the annulus increases as r, the excess should drop as r^{-1} (at large

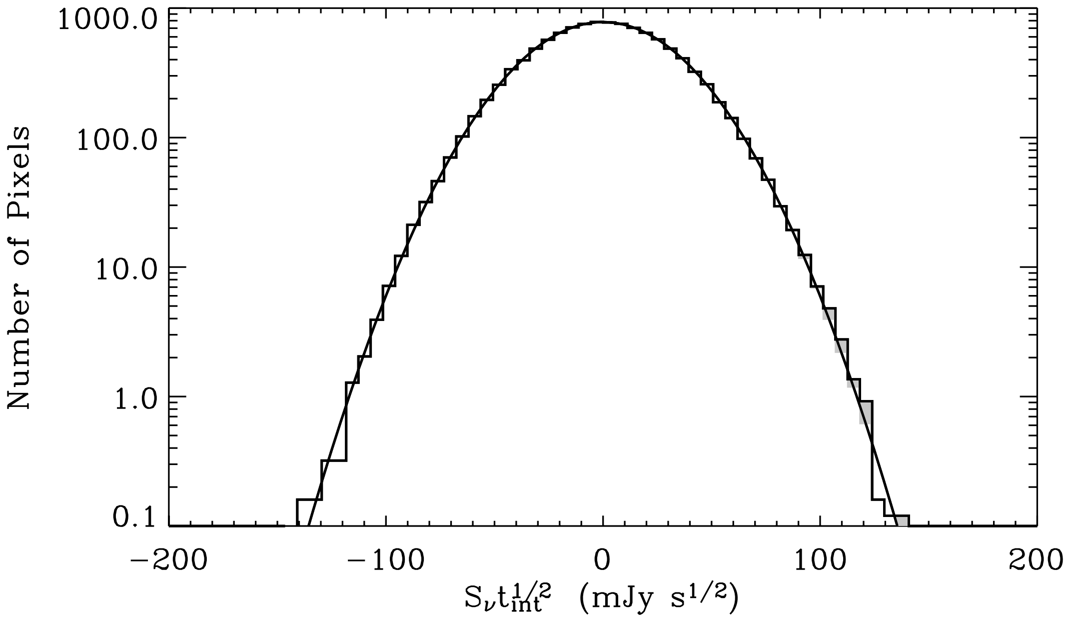

Figure 6.2 Jackknife histogram. In the jackknife test, 50% of the observations were randomly chosen and co-added together, while the remaining 50% of the observations were co-added into a second map. The two maps were then differenced. This was repeated 21 times with the observations randomly selected independently each time, and the histograms were averaged. The thick solid line corresponds to a Gaussian fit to the jackknifed histogram. The shaded region indicates the positive excess, which is insignificant.

jitter amplitudes where the beams do not overlap), as indicated by Figure 6.3. This null test confirms that the excess variance (the positive-side excess in the histogram of Fig. 6.1 from source candidates) is contributed to by the ensemble of observations and has a small characteristic length scale (corresponding to point sources).

6.3 Comparison With Other Submillimeter and Millimeter-Wave Surveys

The Bolocam galaxy survey provides a unique contribution to the current state of submillimeter galaxy surveys. The 850 μm JCMT SCUBA 8 mJy survey (Scott et al. 2002; hereafter SCUBA survey), with a $14''$ beam, implemented a jiggle map strategy with a $30''$ chop throw over 122 arcmin^2 to an rms of 2.5 mJy beam^{-1}. The 1.2 mm IRAM MAMBO survey (Greve et al. 2004; hereafter MAMBO survey), with a $10.7''$ beam, scanned at $5''$ s^{-1} with a chop throw of $36''-45''$ and a chop frequency of 2 Hz over 197 arcmin^2 to an rms of $0.6-1.5$ mJy beam^{-1}. Bolocam's $60''$ s^{-1} raster scan strategy (without chopping) facilitated a large 324 arcmin^2 survey to a uniform rms of 1.4 mJy beam^{-1} (Wiener filtered for detection of point sources). Using a model SED based on nearby, dusty, star-forming galaxies (see § 12.3) gives relative flux densities of $1:2.0:0.8$ and relative rms of $1:0.9:0.6-1.4$ for the Bolocam, SCUBA, and MAMBO surveys, respectively, for a galaxy redshift of $z = 2.4$ (with the range given for MAMBO due to nonuniform noise).

Figure 6.4 provides a cumulative overview of recent infrared, submillimeter, and radio observations of the Lockman Hole. The circles of Bolocam, SCUBA, and MAMBO observations correspond to 2 σ confidence regions of position, including both beam sizes and stated pointing errors. The 6 cm VLA radio sources of Ciliegi et al. (2003) and unpublished 21 cm VLA sources of Yun et al. (2005), with average noise levels of 11 and $10-15$ μJy beam^{-1}, respectively, are identified. The Yun et al. (2005) radio field covers the entire Bolocam good coverage region, while the center of Ciliegi et al. (2003)

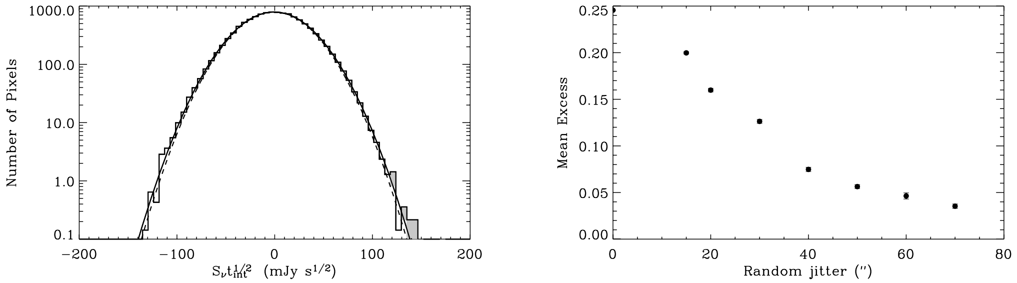

Figure 6.3 *Left*: Pointing-jittered histogram. In the pointing jitter test, individual maps were made from each observation, then co-added with 60″ amplitude offsets with random directions (phases). The solid line is a Gaussian fit to the negative side of the histogram and mirror imaged to the right side of the histogram, indicating that the galaxy candidates have disappeared. The dashed line corresponds to a Gaussian fit to the jackknifed histogram of Fig. 6.2. *Right*: Decreasing positive-side excess as a function of random jitter amplitude. In this case, the amplitude of the jitter was varied from 15″ to 70″. The excess is defined as the fractional increase in the rms of the jittered histogram compared to the rms of the jackknife distribution of Fig. 6.2. Sixteen iterations were performed at each jitter amplitude with the average plotted in the figure. The statistical uncertainty in each mean excess is smaller than the size of the plotted point.

observations is offset to the northwest, with an overlap of approximately 130 arcmin^2. Also shown are the 20 published radio sources from deep 21 cm VLA observations (average noise level of 4.8 μJy beam^{-1}) from Ivison et al. (2002) that are coincident with SCUBA sources, as well as deep unpublished 21 cm VLA observations coincident with the Bolocam sources (Biggs & Ivison, 2006). An additional 21 cm VLA source discovered by Egami et al. (2004) from the reexamination of the Ivison et al. (2002) map and recent *Spitzer* detections of SCUBA sources (Egami et al., 2004) are also identified. Five SCUBA sources from the Scott et al. (2002) catalog (LE850.9, 10, 11, 15, 20) were retracted by Ivison et al. (2002) on the basis of large $\sigma_{850\mu\text{m}}$ values (and lack of radio identifications) and are depicted by crosses through them.

Examination of Figure 6.4 shows discrepancies in detections between the surveys. Table 6.2 summarizes the coincident detections between Bolocam 1.1 mm, SCUBA 850 μm, MAMBO 1.2 mm, and VLA radio observations. Each row in the table corresponds to the fractional number of counterparts detected by each survey. The five SCUBA sources retracted by Ivison et al. (2002) are not included in this comparison. The coverage of each survey was taken into account, with only the overlapping uniform coverage regions considered. The surveys have a wide range of agreement, ranging from 23% (7 of 31 SCUBA sources detected by Bolocam) to 75% (6 of 8 Bolocam sources detected by SCUBA). Six of the 17 Bolocam detections are galaxies previously detected by the SCUBA 8 mJy survey. Of the remaining 11 Bolocam sources, 9 of them lie outside the SCUBA 8 mJy survey region. Similarly, 7 of the 11 Bolocam sources present within the MAMBO good coverage region were detected with MAMBO at 1.2 mm. Two of the 4 Bolocam source candidates not detected by MAMBO have expected 1.2 mm flux densities (from the model SED of § 12.3) below the MAMBO detection threshold for $z = 2.4$. The large fraction of Bolocam sources detected by SCUBA and MAMBO suggests that these submillimeter galaxy candidates are real. The impact of the converse of this statement is less clear: The majority of SCUBA and MAMBO sources were not detected by

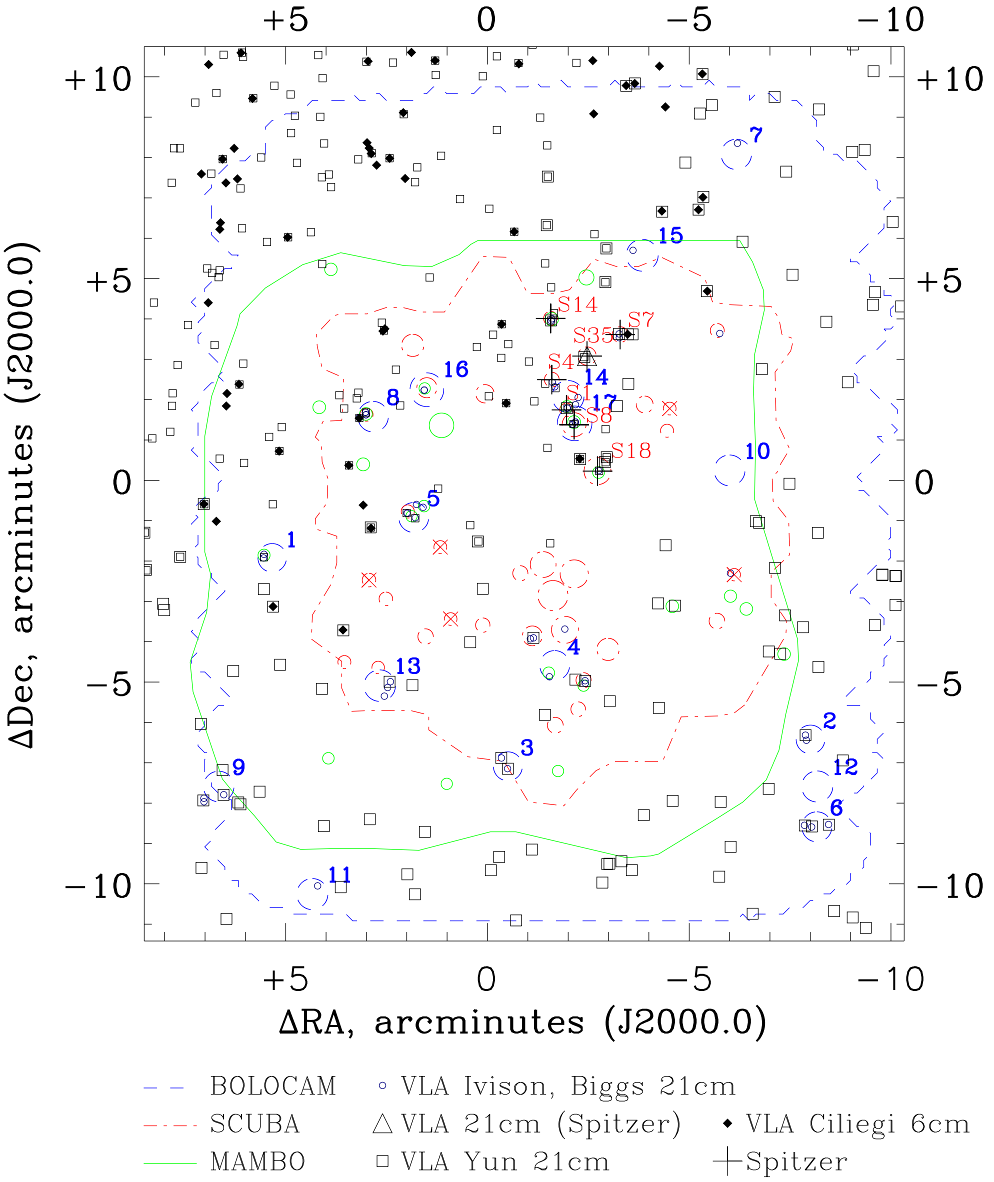

Figure 6.4 Galaxy surveys in the Lockman Hole East region. The 17 Bolocam submillimeter galaxy candidates have been labeled in order of brightness. The circle radii of Bolocam, SCUBA (Scott et al., 2002), and MAMBO (Greve et al., 2004) detections correspond to twice the beam sizes and stated pointing errors added in quadrature to indicate an approximate region of astrometric uncertainty and source confusion. The good coverage regions of Bolocam, SCUBA and MAMBO are shown. VLA radio sources are identified by filled diamonds (Ciliegi et al., 2003), open squares (Yun et al., 2005), and small blue circles (Ivison et al., 2002; Biggs & Ivison, 2006). The five crossed-out SCUBA sources are those retracted by Ivison et al. (2002). Plus signs correspond to SCUBA sources detected by *Spitzer* IRAC and/or MIPS observations (Egami et al., 2004). Reexamination of the 20 cm Ivison et al. (2002) VLA radio map by the *Spitzer* group (Egami et al., 2004) reveals a source (*triangle*) coincident with SCUBA source LE850.35.

Bolocam, although 17 out of 24 nondetected SCUBA sources and 7 out of 15 nondetected MAMBO sources have expected 1.1 mm flux densities (from the aforementioned model SED) below the Bolocam detection threshold, nor is there a strong correlation between SCUBA and MAMBO sources. Some of these sources may not be real or may not be modeled well by the assumed SED. Furthermore, the vast majority (88%) of Bolocam source candidates have at least one radio coincidence, although a minimum[1] 20% accidental detection rate is expected. (This accidental detection rate is the Poisson likelihood that one or more of these known radio sources, randomly distributed, fall within the 2 σ confidence region of the Bolocam beam.) To help verify the $9.1''$ pointing rms of § 5.3, the rms positional error of the Bolocam galaxy candidates compared to the VLA radio positions was calculated for both all Bolocam sources with radio counterparts and the subset of sources (1, 5, 8, 16, and 17) with additional SCUBA and/or MAMBO detections. (Bolocam galaxy candidate 14 was excluded owing to source confusion.)

Two of the Bolocam source candidates (10, 12) show no counterparts in the other submillimeter or radio surveys. These may be false detections, although one of these candidates is outside of the SCUBA and MAMBO good coverage regions, which explains the lack of additional submillimeter detections. It is possible that one or both of these Bolocam source candidates without radio counterparts may instead be sources at high redshift ($z > 3$), where the positive K-correction (sharp drop in flux density with increasing redshift) causes dim radio counterparts. Four SCUBA detections that have at least two detections from MAMBO, *Spitzer*, and VLA were not detected by Bolocam, although the corresponding pixels in the Bolocam map have flux values just below the 4.2 mJy detection threshold for two of these nondetections. A description of each Bolocam detection (as well as nondetections) follows in the next section.

The Bolocam 1.1 mm beam solid angle is 0.30 arcmin^2 and the uniform coverage

---

[1] As only the VLA observations from Yun et al. (2005) and Ciliegi et al. (2003) include an entire source catalog, we are limited to estimating accidental detection rates for these two surveys.

Table 6.2. Summary of Coincident Detections

	Fraction of Galaxy Candidates Detected				
Survey	Bolocam	SCUBA	MAMBO	Radio	Accidental Radio
Bolocam/CSO	-	6/8	7/11	15/17	$\geq$3
SCUBA/JCMT	7/31	-	8/31	15/31	3
MAMBO/IRAM	8/23	8/17	-	11/23	1

Note. — Each row corresponds to the fraction of sources detected **by** each survey (i.e. 6 of 8 Bolocam galaxy candidates in the overlap region were detected by SCUBA, whereas Bolocam detected 7 of 31 SCUBA sources). Column of radio detections include detections by Ivison et al. (2002), Ciliegi et al. (2003) Yun et al. (2005) and/or Biggs & Ivison (2006). The accidental detection rate is that expected from a random distribution of these known radio sources within the 2 σ confidence regions of Fig. 6.4. Several Bolocam sources have radio counterparts detected only by Biggs & Ivison (2006), and as this data set does not include an entire source catalog, we are unable to accurately estimate the accidental detection rate.

region of the map is 324 arcmin^2. There are thus approximately 1000 beams in the map. With 17 source candidates, or $\sim$ 50 beams per source, source confusion is not a serious issue. We define "source confusion" here as a high spatial density of detected sources that makes it difficult to distinguish individual sources. This should not be confused with "confusion noise" from sources below the detection threshold (discussed in detail in § 7.4). Nevertheless, source confusion exists at some level because several Bolocam sources are either closely spaced or near multiple SCUBA detections. While the clustering properties of submillimeter galaxies remain uncertain, there exists tentative evidence from both two-dimensional angular correlation functions (Greve et al., 2004; Scott et al., 2002; Borys et al., 2003) and clustering analyzed with spectroscopic redshift distributions (Blain et al., 2004) that suggests strong clustering with large correlation lengths (as well as correlation to other classes of high-redshift galaxies, including Lyman break galaxies and X-ray loud AGNs; Almaini et al., 2003). We do not attempt to quantify source confusion here but address it in a paper in preparation.

There are 24 8 mJy SCUBA 850 μm and 15 MAMBO 1.2 mm sources within our survey region that we did not detect. Statistically, however, we detect the aggregate average of these at significances of 3.3 and 4.0 σ, respectively, at $\lambda = 1.1$ mm. This was done by measuring the distribution of "sensitivity" values (scaled by $t_i^{1/2}$) for the Wiener-filtered map pixels that coincide with SCUBA or MAMBO sources for which we found no excursion above our detection threshold. If no subthreshold "counterparts" are present in these pixels, the sensitivity values should follow the noise distribution of the map (albeit truncated at 3 σ). Such a distribution has a mean value of -0.004 σ. In the data, we find that the sensitivity values for these map pixels have mean values of 1.0 ± 0.3 and 0.8 ± 0.2 σ for the SCUBA and MAMBO nondetections, respectively. Assuming that uncertainties are Gaussian distributed, the probabilities of such large nonzero means to have arisen from pure noise are very low, 1.7×10^{-4} and 2.5×10^{-4}, respectively. Thus, we have statistically detected the ensemble of SCUBA and MAMBO sources below our threshold at the 3.3 and 4.0 σ confidence levels, respectively.

6.4 Bolocam Nondetections

The Bolocam nondetections are as follows:

SCUBA.LE850.14, 18.—These galaxy candidates have SCUBA and MAMBO detections, with *Spitzer* IRAC and MIPS and VLA (Ivison et al. 2002, Yun et al. 2005) counterparts. SCUBA source 14 is discernible in the Bolocam observations at 3.9 mJy, just below the 4.2 mJy, 3 σ detection threshold. The Bolocam pixel coincident with SCUBA source 18 has a flux density of 1.6 mJy, well below the detection threshold.

SCUBA.LE850.7, 35.—These sources are detected by SCUBA, *Spitzer* IRAC and MIPS, and VLA (7, Ivison et al. 2002; 7, 35 Yun et al. 2005; 7, Ciliegi et al. 2003; 35, Egami et al. 2004). The flux density in the Bolocam map coinciding with SCUBA source 7 is 3.4 mJy, below the 3 σ detection threshold. At a Bolocam flux density of 0.9 mJy, SCUBA source 35 is well into the Bolocam noise.

Chapter 7

Number Counts from Observed Sources

In this section we discuss the extraction of the number (per unit flux density per unit solid angle) versus flux density relation ("number counts") from the observed sources. Because of the presence of noise (due to the instrument, the atmosphere, and confused background sources), there is a bias in both the observed flux densities and the observed histogram of number of sources versus flux density. This bias, first noted by Eddington (1913, 1940), is quite generic when attempting to measure a statistical distribution in the presence of noise. Further, because our S/N with respect to these noise sources is not large, this bias is an effect comparable in size to the statistical Poisson errors in determining the number counts.

There are two broad approaches to extracting the number counts in the regime where bias is significant. The first is to directly correct the observed number versus flux histogram using some knowledge of the statistics of the survey. The other approach is to assume a model and attempt to match its parameters to the data using a fit, aided by simulation. The direct correction approach does not appear promising for this survey. Eddington (1940) showed that, in the presence of Gaussian measurement noise, one could apply an asymptotic series correction to the observed distribution to obtain a better estimate of the underlying distribution. This correction involves even-numbered derivatives of the observed distribution, and so, with our observed distribution containing only 17 sources, this method is impractical. Another approach might be to individually correct each source by its expected bias, but Eddington (1940) also showed that using the distribution of corrected fluxes as a measure of the underlying distribution is fundamentally incorrect. Thus, we have elected to fit a model to the data.

The formalism for relating a given underlying number count distribution to the observed number counts is given in § 7.1. This provides the definition of the survey bias, completeness, and false detection rate. The simulations used to determine these quantities are described in § 7.2, and their actual calculation is given in § 7.3. The effect of confusion noise on the survey is discussed in § 7.4. The method of extracting the underlying counts is given in § 7.5. Caveats and difficulties in extracting the underlying number counts, as well as suggestions for improvements in a future analysis, are discussed in § 7.6.

7.1 Formalism

For a given observing frequency band, we denote the differential number count (DNC) distribution of galaxies per unit flux density interval per solid angle as $N'(S)$. The cumulative number count (CNC) distribution will be denoted $N(S)$, with units of number per solid angle. The relation between the true N' and the observed distribution n' must account for the effects of random noise, the presence of a detection threshold, and confusion noise (i.e., a contribution to the variance of the map due to sources below the detection threshold). As a result of all forms of noise, a source having flux density S is in general observed with a different flux density s. Let $B(s, S; N')$ be the probability density that a source with true flux density S is observed at a flux density s; the implicit dependence on the confusion noise is included by the parametric dependence on N'. $B(s, S; N')$ is normalized such that

$$\int_{-\infty}^{\infty} B(s, S; N')\, ds = 1 \qquad (7.1)$$

for all values of S. The quantity $B(s, S; N')$ will be referred to as the "survey bias". By normalizing according to equation (7.1), one assumes that a source of true flux S will be found at some flux s with probability unity. In the presence of a detection threshold, however, sources whose observed flux fluctuates below the threshold will not be included in n'. In this case, the integral in equation (7.1) is not 1, but $C(S; N')$, the "survey completeness," namely, the probability that the source is found at all. Note that this also depends on the confusion noise through N'. In addition, there may be *false detections* of noise fluctuations, $F(s)$, which contribute to the observed number counts. Thus, the expression for the observed DNC distribution is

$$n'(s) = F(s) + \int_0^\infty B(s, S; N')C(S; N')N'\, dS. \tag{7.2}$$

In the following, the dependence of B and C on N' will not be written explicitly.

Under the assumptions of uniform Gaussian noise with rms σ, negligible contribution from confusion noise, and a fixed detection threshold $n\sigma$, analytical expressions for $C(S)$, $B(s, S)$, and $F(s)$ can be derived. For future reference, these are

$$C(S) = \frac{1}{\sqrt{2\pi}\sigma} \int_{m\sigma}^\infty \exp\left[\frac{-(s-S)^2}{2\sigma^2}\right] ds, \tag{7.3}$$

$$B(s, S) = \frac{1}{C(S)} \frac{1}{\sqrt{2\pi}\sigma} \exp\left[\frac{-(s-S)^2}{2\sigma^2}\right] \Theta(s - m\sigma), \tag{7.4}$$

$$F(s) = \frac{\mathcal{N}}{\sqrt{2\pi}\sigma} \exp\left[\frac{-s^2}{2\sigma^2}\right] \Theta(s - m\sigma), \tag{7.5}$$

where $\Theta(x)$ is the unit step function ($\Theta = 1$ for $x > 0$, $\Theta = 0$ for $x < 0$) and $\mathcal{N}$ is a normalization factor for $\mathcal{N}$ independent noise elements.

7.2 Simulation of Noise Maps

Two types of simulations were done to determine the survey bias, completeness, and false detection rate. Both methods simulate only the instrument and atmospheric noise (the "random noise") and do not include the effect of confusion noise. This is appropriate for the case in which the random noise dominates. The validity of this assumption is discussed in § 7.4.

In the first suite of simulations, the observational data were used to generate 100 fake maps (noise realizations) by jittering the individual time streams $60''$ in right ascension/declination coordinates with a random phase before they were co-added to make maps. This had the effect of washing out the point sources as discussed in § 6.2. Note that realizations of these jittered maps are not fully independent because the noise is somewhat correlated between realizations; the average correlation coefficient between maps is 4%. Statistical error bars on the completeness and bias determined from this simulation method include the contribution from the correlation. The pointing jitter dilutes the variance of sources present in the jittered map to 20% or less of its value in the unjittered map (see Fig. 6.3), effectively removing confusion noise.

Because of the large amount of time required to generate many realizations of maps from real time stream data (as in the case of the jittered maps) and the difficulties of fully simulating time stream realizations of instrument and atmospheric noise, a second simulation method was developed. In this method, the noise properties are derived from the jackknife maps, which represent realizations of signal-free instrument noise. The noise model for the map (before optimal filtering) assumes that the noise map, $n(\mathbf{x})$, can be described as an independent noise per pixel that scales as $1/\sqrt{t_i}$, where t_i is the integration time in pixel i, combined with a mild pixel-to-pixel correlation. This correlation is assumed to be stationary over the map and can thus be described by the two-dimensional PSD of the noise map $\xi^2(\mathbf{k})$, normalized so that its integral has unit variance. These assumptions are justified because, as shown in § 6, the coverage variation accounts for most of the point-to-point variation in the noise, and examination of the jackknife map PSD shows that the $1/k$ contribution to the PSD is small compared to the white term, leading to largely uncorrelated pixels. The noise model for the map after Wiener filtering is straightforwardly obtained by convolving the noise map with the Wiener filter.

The assumptions above are equivalent to writing the covariance matrix **C** for the unfiltered map as

$$\mathbf{C} = \mathbf{D}^{1/2}\mathcal{F}^{-1}\xi^2\mathcal{F}\mathbf{D}^{1/2},$$

where **D** is diagonal in pixel space and describes the coverage variations, ξ is diagonal in **k**-space and describes the pixel noise correlations, and $\mathcal{F}$ is the discrete Fourier transform. The elements of **D** can be written as

$$D_{ij}^{1/2} = \sqrt{\frac{A}{t_i}}\sigma\delta_{ij}.$$

where σ^2 is the sample variance of the noise and A is a normalization that ensures that the sum of the pixel variances $\sum_i A\sigma^2/t_i$ is equal to $(N-1)\sigma^2$, the total noise variance in the map. The noise map should satisfy $< nn^T >= \mathbf{C}$; a given realization is

$$n = \mathbf{D}^{1/2}\mathcal{F}^{-1}\xi\mathcal{F}w,$$

where w is a realization of uncorrelated, Gaussian, mean zero, unit variance noise. Determining the noise model then reduces to determining the form of $\xi(\mathbf{k})$ and the value of σ. The PSD ξ^2 is computed directly from the uniform coverage region of the unfiltered jackknife maps using the discrete Fourier transform; multiple jackknife realizations (which are nearly independent) and adjacent **k**-space bins are averaged to reduce the noise on the measurement of the PSD. The overall noise normalization σ is determined by requiring that the variance of $n(\mathbf{x})$, when considered in the good coverage region, Wiener filtered, and multiplied by $\sqrt{t_i}$, is equal to the variance similarly determined from the jackknife maps (§ 6.2 and Fig. 6.2). One thousand noise realizations were generated in this way.

7.3 Calculations of False Detection Rate, Bias, and Completeness

The false detections were determined by simply running the source detection algorithm on each of the simulated maps for both types of simulations and recording the number and recovered flux density of the detections. Figure 7.1 shows the results for both methods. Also plotted is the theoretical prediction, assuming that the normalization $\mathcal{N}$ is either $N_{\rm beams}$ or $N_{\rm pixels}$, which should bracket the possibilities. It is seen that neither Gaussian model describes the simulated false detection rate well, although both methods of simulation agree well with each other. The Gaussian model does not describe the simulation data well in either amplitude or shape. The amplitude discrepancy occurs because $\mathcal{N}$ is the number of effective independent noise elements, which depends on both the correlations in the noise and the detection algorithm, which does not count all pixels above threshold as source candidates but considers all pixels within a merged group to be a single source. The shape of the Gaussian model fits poorly owing to three effects: First, because of the coverage variation, the threshold is not sharply defined in flux density units, causing some false detections **below** the threshold. Second, the grouping algorithm merges closely spaced false detections in the Wiener-filtered map and assigns a single flux density to the brightest pixel, a conditional probability that is flux dependent. Finally, the pixels are not independent, since both $1/f$ noise and the Wiener filter correlate them. Because of the difficulty in deriving an analytic expression for all these effects, the false detection rate as determined by simulation is used in further analysis (see § 7.5) instead of the Gaussian prediction. The mean number of false detections in the Lockman Hole map as determined from simulation is 6 (Poisson distributed).

To find the completeness and bias, sources of known flux density were injected into the noise maps. First, a source-only map was created by adding 30 $31''$ FWHM two-dimensional Gaussians at a specified flux density level to a blank map. The sources were injected at random into the uniform coverage region but were spaced far enough apart that the source detection algorithm could distinguish each of them; this circumvented potential complications involving source confusion. Then, the source-only map was added to a noise map to simulate a sky map post cleaning and mapping. Next, this

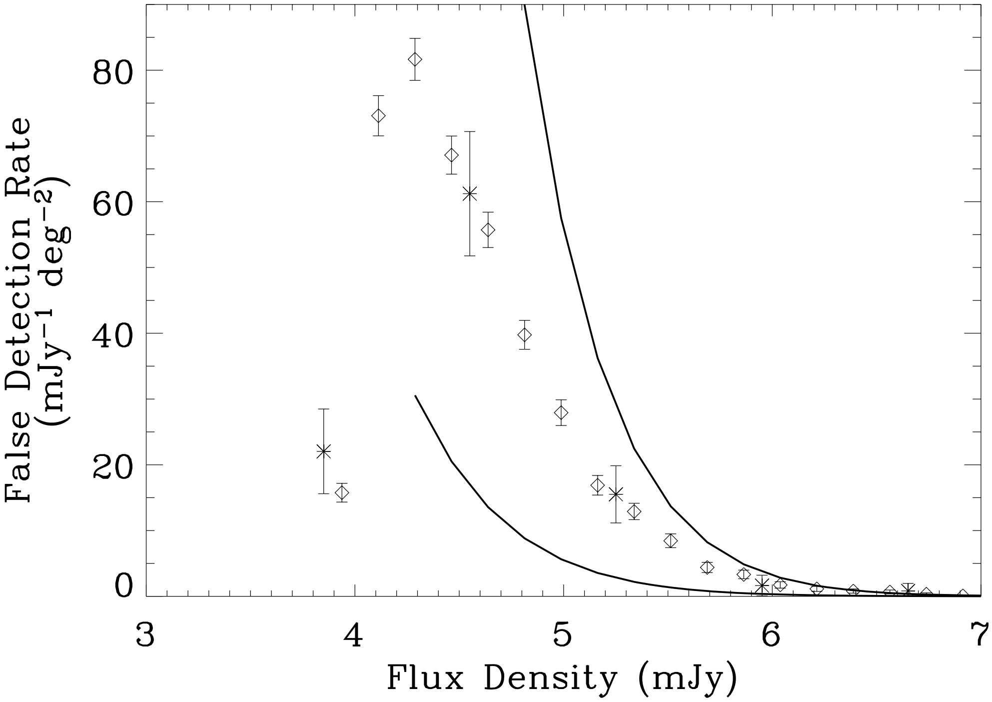

Figure 7.1 False detection rate plotted vs. flux density. Diamonds are simulations from the map statistics, and asterisks are simulations from the data, shown with error bars for the finite number of simulation realizations. The two solid curves show the theoretical bounds on this quantity, the lower curve assuming that the number of independent statistical elements is the number of beams in the map, and the upper assuming that it is the number of pixels in the map.

map was Wiener filtered and run through the source extraction algorithm, which enabled us to determine which sources were detected and their resulting flux densities. Each extracted detection was centroided to determine its position, and then its position was compared with the position of the nearest injected source. If the positions were within $15''$ (roughly the distance between two adjacent, diagonal pixels), the extracted detection was considered real. The flux density was determined by the maximum value of detected pixels, as is appropriate for the Wiener-filtering algorithm.

With these mechanics in place, the completeness was calculated by computing the ratio of the number of detections at a given flux to the number of injected sources. This was repeated for source flux densities ranging from 2.8 to 9.8 mJy for simulations from map statistics and from 1.4 to 9.8 mJy for jittered data simulations in 0.7 mJy intervals, with the results plotted in Figure 7.2. The two types of simulations agree well. The survey completeness is 50% at the 3 σ detection threshold, as expected, because half of the sources at the threshold will be bumped upward by noise and half will be bumped downward. The simulations also agree with the theoretical prediction for Gaussian noise.

The bias was computed by determining the distribution of measured flux densities as a function of injected flux densities. At relatively large flux densities, the bias distribution should approach a Gaussian distribution centered at the injected flux density, with σ equal to the map rms. This is seen to be the case in Figure 7.3 for injected flux densities ≥ 7 mJy. The figure gives the distribution of the expected observed flux densities (probability density per flux bin, normalized to an integral of unity) for a range of injected flux densities. For low injected flux densities approaching the detection threshold, the distributions become increasingly asymmetric owing to the presence of the threshold. The distributions do not drop abruptly to zero below the threshold because there are variations in the map coverage. Note that sources with true flux below the detection threshold may be detected. The average bias for a source is shown in Figure

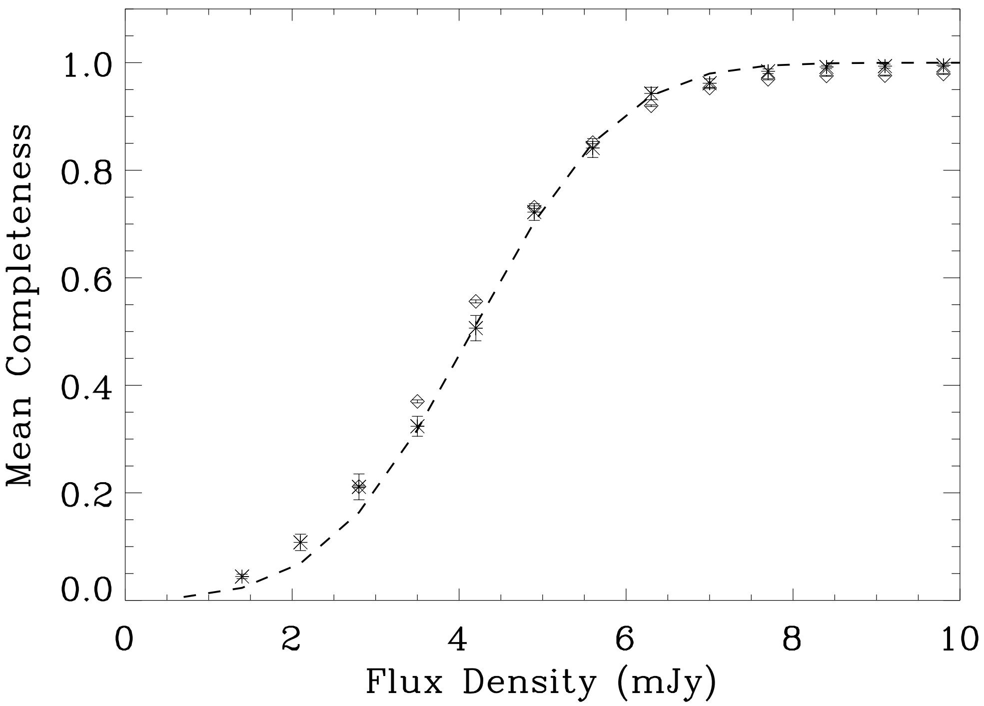

Figure 7.2 The survey completeness as a function of flux density. Diamonds are simulations from the map statistics, and asterisks are simulations from the jittered data, shown with error bars for the finite number of simulation realizations. The dashed curve shows the theoretical prediction for the Gaussian case with $\sigma = 1.4$ mJy (the mean noise level of the cleaned Lockman Hole map). The error bars are statistical only and do not reflect systematic differences in the two simulation methods.

7.3; this rises steeply for sources with fluxes near or below the detection threshold.

The preceding discussion (in particular the agreement of the simulated bias and completeness with the Gaussian theoretical prediction) indicates that, in spite of coverage variations and correlated noise, the noise in this survey behaves substantially like uniform Gaussian noise. Comparison of the results of the map simulation method with the jitter technique also shows good agreement, indicating that the assumptions that went into the map simulation method are justified and that we have a reasonable model for the survey noise. This gives added confidence to the determination of the false detection rate, which depends only on the noise properties.

7.4 Effects of Confusion Noise on the Bias and Completeness Functions

The completeness and bias function estimates as determined in §§ 7.2 and 7.3 do not include the effects of confusion noise. The effect of confusion noise is illustrated by considering two extremes: instrument noise dominant over confusion noise and vice versa. When instrument noise is dominant, the bias function for this survey is correctly described by equation (7.4). In the confusion-dominated limit, the bias function takes on the shape of the source count distribution, reflecting the fact that it is the underlying distribution of sources that may bias the flux of a given source. In between these two extremes, the Gaussian bias function acquires additional width and a long positive tail from the source counts distribution. This tail increases the probability that a low flux source will fluctuate above the detection threshold. Consequently, the completeness at low flux densities is increased over the case of Gaussian noise. Note that small changes in the bias tail can cause large changes in the subthreshold completeness. The case at hand falls in this in-between regime. Understanding the modification to the bias function by confusion noise is necessary for accurately estimating how confusion transforms a model source count distribution to an observed one, as in equation (7.2). It

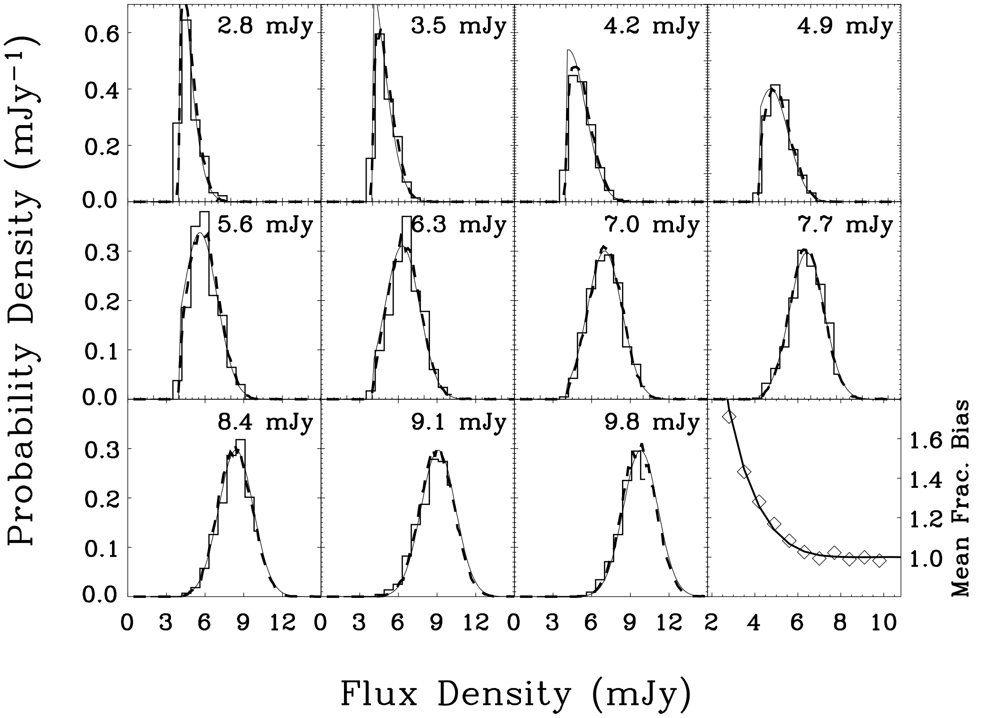

Figure 7.3 Survey bias as a function of observed flux density for a variety of input flux densities. The bias is normalized as a probability density as a function of observed flux density. The flux densities of the sources injected in the simulation are shown in the upper right of each panel. The solid histograms are simulations from the jittered data, the dashed curves are simulations from the map statistics, and the solid curves (which lie nearly on top of the map statistics simulation) are the Gaussian predictions for $\sigma = 1.4$ mJy (the mean noise level of the cleaned Lockman Hole map). The bottom right panel shows the mean fractional bias as a function of input flux density for the simulations from the map statistics. The solid curve is the Gaussian prediction for $\sigma = 1.4$ mJy.

is difficult to precisely model the effects of confusion on bias and completeness because they depend on the source count distribution that one is trying to measure.

We can estimate the size of the confusion noise present in our maps by finding the relative contributions of the noise and signal variances. The sample (per pixel) variance of the optimally filtered Lockman map in the good coverage region is found to be 2.37 mJy^2. The variance of the optimally filtered jackknife maps in the same region is 1.81 mJy^2, leaving 0.56 mJy^2 due to sources. The variance contributed by all the sources in Table 6.1 is approximately 0.33 mJy^2, of which 0.10 mJy^2 is expected to be due to false detections of random noise peaks. This leaves 0.33 mJy^2 due to undetected sources. This represents an S/N per pixel of 0.37 in rms units; considered in quadrature with the 1.81 mJy^2 of the noise, it increases the noise estimates and the rms of the bias function by about 9%.

To estimate the effect of confusion noise on the survey completeness and bias, particularly in the tail, sources were injected one at a time into the real map and extracted using the source extraction algorithm, with the completeness and bias calculated as in the noise-only case. This has the effect of making only a small change in the observed distribution of pixel values, effectively preserving that distribution. No effort was taken to avoid the positions of source candidates, as this would bias the procedure by failing to take into account the tail of the distribution. This test showed that the bias acquired a high flux density tail, as expected, and the completeness was increased above its Gaussian noise value. It should be emphasized, however, that this method provides an upper limit because it effectively "double-counts" confusion: the map into which the sources are injected is already confused. Positions of high flux in the true map may already consist of two coincident lower flux sources, and so the probability of a third source lying on top of them is not truly as high as the probability we would calculate by this procedure. The determination of the completeness and bias in this way is also limited by the statistics of only having one realization of the confusion noise. Applying these new bias and completeness functions, as well as the Gaussian noise-only bias and completeness (eqs. [7.3] and [7.4]), to a power-law model of the number counts (the best-fit model of § 7.5), the change in the observed counts is of order the size of the 68% confidence interval for Poisson errors in the observed counts. Thus, confusion noise is not wholly negligible nor does it dominate. In extracting the number counts, we ignore the confusion noise but discuss how to treat it correctly in § 7.6.

7.5 Fitting a Model to the Differential Number Counts

To extract number counts from this data set, we use equation (7.2) with the simulation-derived false detections and the completeness and bias of equations (7.3) and (7.4). A model for N' is also required. Because of the small number of detections, the model must have as few free parameters as possible so that the data will be able to constrain the model parameters. This pushes us away from detailed, physically motivated models and toward a simple model in combination with several, somewhat arbitrary, constraints. We use a two-parameter power-law model for N' given by

$$N'(S;\mathbf{p}) = A\left(\frac{S_0}{S}\right)^{\delta}, \tag{7.6}$$

where $\mathbf{p} = [A, \delta]$ and S_0 is a fixed constant (not a parameter of the model). The choice of this form for $S_0 \neq 1$ reduces the degeneracy between A and δ that prevails over narrow ranges of S, such as in this survey. We have set $S_0 = 4$ mJy.

The unaltered model of equation (7.6) is unsatisfactory at both high and low flux values. At low fluxes, the model diverges, requiring a cutoff on which the result depends. The issue of the low-flux cutoff is discussed further in § 7.6. For now, we simply impose a low-flux cutoff $S_l = 1$ mJy in the integral over S in equation (7.2). In addition, if the model is extended indefinitely to high fluxes, it may produce too many sources to be consistent with the lack of observed sources. This constraint nevertheless does not determine the shape of number counts above the highest flux observed. Thus, one must either implement a high-flux cutoff or assume something about the shape of the number counts beyond the region where they are measured. To address this, a single bin of the same width as the other bins has been added to the data at high fluxes, where the data are zero and the model nonzero; beyond $S_h = 7.4$ mJy, the model is zero. Fixing the upper cutoff as above and allowing the lower to float to its best-fit value produces $S_l = 1.3$ mJy. Two additional possibilities were also tried for a high-flux cutoff: (1) setting the model to zero beyond the highest filled bin resulted in a very shallow index ($\delta < 2$), and (2) allowing the highest bin to extend to infinity produced a very steep power law ($\delta > 10$). While both of these cases are unphysical, they illustrate the sensitivity of the power-law model on the high-flux cutoff. Thus, the constraints that have been adopted, while arbitrary, serve to restrict the range of possible models sufficiently to extract reasonable values of $[A, \delta]$. However, in light of this arbitrariness, the resulting constraint on the parameters of the power-law model must be treated with skepticism.

To fit to the model, the data are first binned. The number of sources with observed flux between s_k and s_{k+1} is denoted by n_k. We assume that the number of sources counted in any interval ds follows an approximate Poisson process and therefore that each n_k is a Poisson-distributed random variable that is independent of n_j for $k \neq j$. The same would not be true of the cumulative counts, and so the differential counts are preferred for this analysis. The likelihood of observing the data $\{n_k\}$ if the model is $\{N_k\}$ is then

$$\mathcal{L} = \prod_k \frac{N_k^{n_k} \exp\left[-N_k\right]}{n_k!} \tag{7.7}$$

because it is assumed that the bins are independent. The value of the model in a given observed bin is defined as

$$N_k(\mathbf{p}) = \frac{1}{\Delta s} \int_{s_k}^{s_{k+1}} \left(F(s) + \int_0^\infty B(s, S) C(S) N'(S; \mathbf{p}) \, dS \right) ds. \tag{7.8}$$

The function $-\ln \mathcal{L}$ is minimized with respect to $\mathbf{p}$ to find the maximum likelihood value of $\mathbf{p}$.

Two modifications of the likelihood equation (7.7) were made for this analysis. The first is that a prior was applied to constrain $\delta > 2$, so that both the integral of the number counts and the integral of the total flux density remained finite for $S > 0$. Thus,

$$\mathcal{L}' = \mathcal{L}\Theta(\delta - 2).$$

Second, to extract confidence regions for the fitted parameters, it was necessary to normalize $\mathcal{L}'$, such that

$$\int \mathcal{L}'(\mathbf{p})\, d\mathbf{p} = 1.$$

This normalization was done by numerical evaluation of the likelihood and its integral over the region where it is appreciably nonzero (see Fig. 7.5 below).

The various components of this fit are shown in Figure 7.4. The data are shown with 68% confidence interval error bars, based on the observed number of sources in each bin, scaled to an area of a square degree. The error bars were computed according to the prescription of Feldman & Cousins (1998) for small number Poisson statistics (which unifies the treatment of upper confidence limits and two-sided confidence intervals). The error bar on the highest flux density bin is an upper limit. The model is clearly consistent with the data given the error bars. (All six model bins falling within the 68% confidence interval error bars of the data **may** imply that the errors have been overestimated, although this has a 10% probability of occurring.) Examining the fit in stages, one finds that the product of the survey completeness and the best-fit number counts shows that the survey incompleteness reduces the number of sources observed at low flux densities as expected; above ~7 mJy, the survey is essentially complete. The effect of the bias, however, combined with the steepness of the number counts, increases the number of sources observed in all bins substantially above that of the underlying source distribution and contributes to the observed number of sources in all bins. In fact, based on the best-fit DNC and computing over the range of fluxes observed, 67% of real sources will have a true flux density **below** the detection threshold. Note that the best-fit number counts lie below the Poisson errors for the raw counts, demonstrating again that the survey bias is a nonnegligible effect. Given the maximum likelihood values of A and δ (52.0 and 3.16, respectively), the cumulative source count at $S_{1.1\mathrm{mm}} > 2.75$ mJy is 192^{+108}_{-88} deg^{-2}. This is consistent with the 1.2 mm MAMBO number count result (378^{+136}_{-113} deg^{-2}) for the combined Lockman Hole and European Large-Area ISO Survey (ELAIS) N2 regions (Greve at al. 2004).

Contours of the likelihood function for this fit are shown in Figure 7.5. In calculating the likelihood, the upper and lower flux limits were assumed to be a correct model, and as such, the likelihood does not account for violations of this assumption. The shaded region was obtained by integrating the normalized likelihood $\mathcal{L}'$ for values $\mathcal{L}' > \mathcal{L}_{thresh}$, such that the integral was equal to 0.68. These are Bayesian errors that incorporate the prior belief that $\delta > 2$.

7.6 Difficulties and Caveats

As the above discussion indicates, the extraction of number counts from this data set is subject to a number of difficulties and caveats. In addition to the small-number statistics and the difficulty in modeling the dependence of the survey bias and completeness on the confusion noise that have already been discussed, a separate discussion of the principal limitations of the preceding analysis is in order. These are the low S/N of the detections and the sensitivity of the result to the lowest flux objects assumed to contribute to the observed counts. These limitations may be overcome with a more sophisticated future analysis, as we discuss.

The survey bias, combined with an underlying number counts distribution rising at low fluxes, has a strong effect on the fluxes of sources observed at low S/N. This problem is exacerbated in the presence of confusion noise, but it is present in surveys in which random noise dominates over the confusion noise as well. This point has been appreciated in the historical confusion literature. Crawford et al. (1970) showed how to use a maximum likelihood method to extract a power-law slope from observed flux densities, and Murdoch et al. (1973) extended this to the case of sources observed with Gaussian noise. Because of the divergence at low fluxes of a power law, a lower limit in flux must be imposed in order to obtain finite answers. The principal conclusion of Murdoch et al. (1973) was that the power-law slope of the number counts determined by the maximum likelihood method depends sensitively on this lower cutoff if the S/N of the sources used in the survey is less than 5, whereas above this point the slope determination, while biased, is not dependent on the lower cutoff. This sensitivity to the lower flux cutoff also applies to the amplitude of the power law as well, a point that is clearly described by Marshall (1985). Although the Murdoch et al. (1973) result is for the rather unphysical case of a power law with an abrupt cutoff, the general result that derived number counts based on low-S/N sources will depend sensitively on the assumed behavior of the underlying number counts far below threshold is more general. This may be seen by considering the behavior of $C(S)N'$ as $S \rightarrow 0$. As long as this function is increasing, the bias will continue to push some sources of low intrinsic flux up above the detection threshold, and so the low-S/N regime will contain sources from well below threshold. [Note that this is consistent with the behavior of $B(s,S)$, since for s greater than threshold, B is positive for all values of S.] One can see from Figure 7.2 that the completeness drops off rather slowly for Gaussian noise (and even more slowly when confusion noise is added) and never vanishes. In fact, the product of the Gaussian completeness times any $S^{-\delta}$, $\delta > 0$, diverges as $S \rightarrow 0$, so for many otherwise reasonable number counts models, this problem will occur. Thus, in the presence of any sort of bias, whether due to confusion or noise, deriving accurate counts above threshold requires a nontrivial amount of information about the counts well below threshold if the

S/N of the detections is low. Since all of our sources have S/N ≤ 5, any constraint placed on the power-law amplitude and slope will likely depend sensitively on the lower cutoff chosen.

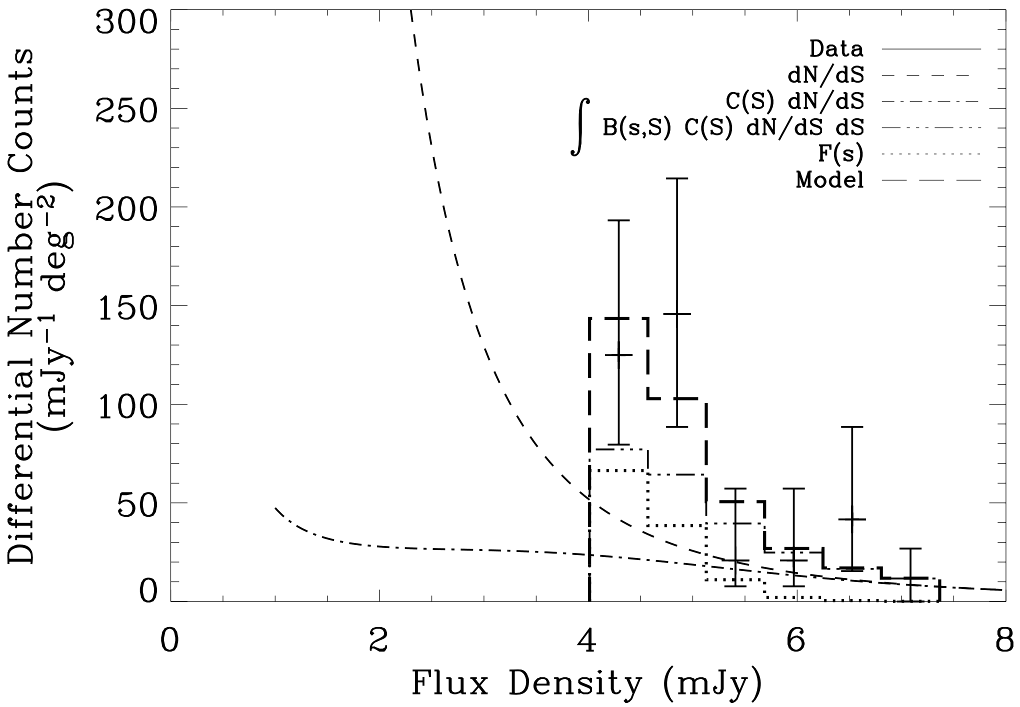

Figure 7.4 Model of the submillimeter number count distribution as a function of flux density (results of finding the maximum likelihood value of the model eq. [7.6]). The functions N' and $C(S)N'$ are shown as continuous functions of true flux density, S, and the data, false detection rate, $\int B(s,S)C(S)(N')\,dS$, and model are shown binned in the coarse bins of observed flux density, s, used for the raw data. (Note that the abscissa is used for two different flux densities, S and s.) The ordinate was scaled from the 324 arcmin^2 of the survey to 1 deg^2. The error bars on the data are Poisson errors as described in the text.

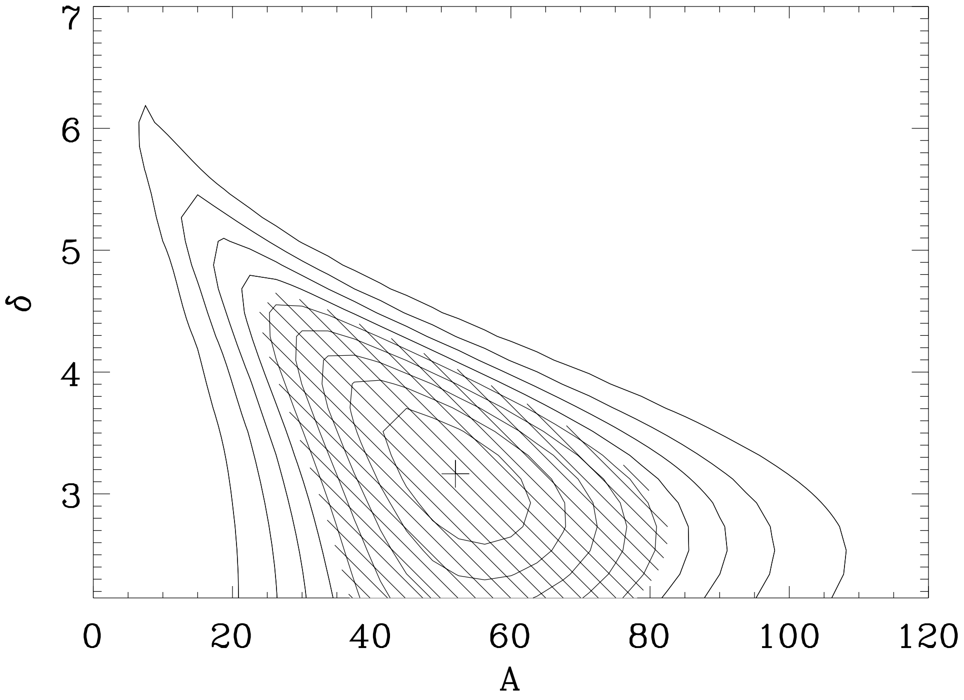

Figure 7.5 Contours of the likelihood function (eq. [7.7]) in the $[A, \delta]$-plane. Contours are shown for 10%, 20%, . . . , 90% of the peak height. The location of the peak is shown by a cross, and the hatched area indicates the 68% confidence region. The maximum likelihood values are $A = 52.0$ and $\delta = 3.16$.

Chapter 8

P(D) Fluctuation Analysis

While I was not the principle investigator of the $P(D)$ analysis (see Maloney et al., 2005), this research stems from the simulations and software that I played a key role in developing and are relevant in confirming the results of the previous section. The key results are therefore summarized here for completeness.

8.1 Introduction

An alternative analysis technique that overcomes the shortcomings mentioned in § 7.6 is the so-called fluctuation or "$P(D)$" (probability of deflection) analysis (Scheuer, 1957, 1974; Condon, 1974). This approach was applied to the 1.1 mm Bolocam Lockman Hole survey (Maloney et al., 2005) both to independently verify the simulation results of the previous section as well as to probe further into the faint end of the number count distribution. The fluctuation analysis has the significant advantage of not requiring the identification and extraction of point sources as all of the available data are used: a direct comparison of the entire observed pixel flux density distribution ($P(D)$) is made to the theoretical distribution assuming a particular number-count model. Because the entire distribution of pixel values in the map are used in this analysis, it is possible to derive information of the number count distribution well below the formal 3 σ detection threshold used for source extraction.

8.2 $P(D)$ Applicability

In principle, the fluctuation analysis provides information of the source distribution down to a flux density level at which there is approximately one source per beam (Scheuer, 1974) provided that the noise level is sufficiently low. This assumes, however, that the noise in the map is uniform and well characterized. Fortunately, the Bolocam Lockman Hole satisfies these requirements, as characterized by the jackknife simulations of § 6.2 (cf. Figure 6.2). As the jackknife maps yield a pixel distribution devoid of sources (which are coherent over all observations and are therefore removed), they may be used to determine the actual PSD of the noise in the Lockman Hole map, independent of the signal contribution. We choose to use the the optimally filtered jackknife maps (which minimizes the contribution of $1/f$ noise by applying a low-frequency roll-off) because with an RMS noise level of 1.4 mJy, we are able to probe the number count distribution to approximately this level. As the optimal filter is a linear mathematical operator that improves the S/N of beam-sized sources independent of signal strength (at the expense of spatial resolution and source confusion), its use preserves the underlying source distribution and therefore does not jeopardize the characterization of the noise in the fluctuation analysis.

The applicability of the fluctuation analysis to probe the distribution of submillimeter galaxies also assumes that the Bolocam Lockman Hole observations are not contaminated by other signals, namely primary and secondary microwave background (CMB) fluctuations, and Galactic foreground emission. The spatial filter of the Bolocam software pipeline, which is needed to quantify the instrument response function to each of these sources, was empirically determined by running simulations of white noise maps through the pipeline. Maloney et al. (2005) conclude by using the current best-fit model to the observed CMB anisotropies (Stompor et al., 2001) and model predictions for the S-Z power spectrum (Zhang, Pen, & Wang, 2002; Bond et al., 2005) that the

RMS contributions to the unfiltered Lockman map are $\simeq 0.24$ mJy each. This is small compared to the 1.8 mJy RMS in the Lockman Hole map before optimal filtering (with the fractional RMS reducing even further once filtered). While we have not explicitly calculated it, Masi et al. (2001) find from the analysis of the dust contribution to BOOMERANG maps that the Galactic dust contribution is negligible compared to the CMB at 275 GHz in low column density regions such as the Lockman Hole.

8.3 $P(D)$ Approach

The measured $P(D)$ of the optimally filtered Lockman Hole map is simply the observed pixel flux density distribution shown in Figure 8.1. Note that the small negative offset of the peak of the distribution is expected due to the presence of sources in the map combined with the constraint of the map to have mean zero (both from the high-pass filter in the Bolocam electronics and sky subtraction). Because the shape of the optimal filter (cf. § 5.5) is not analytic, and due to minor (6%) variations in the noise level (due to variations in coverage per pixel), a direct calculation of the theoretical $P(D)$ distribution to compare with the observed distribution was not possible. Instead, the theoretical $P(D)$ distribution was determined from simulated noise maps by using the sourceless jackknife maps, as discussed in § 7.2. The source distribution added to the noise-only maps is featureless power-law, with a differential number count distribution

$$n(S) = n_o S^{-\delta} \text{ mJy}^{-1}\text{deg}^{-2},$$

where S is the source peak flux density. The injected flux densities (randomly drawn from the above power law) ranged from 0.1 to 10 mJy. Further reducing the lower limit had no significant effect on the results, while the upper limit was set to ensure that no sources much brighter than those found in the Lockman Hole map were present. The sources were uniformly randomly placed (i.e. zero angular correlation) over the Lockman map as Gaussian sources with a pointing-smeared Bolocam beam size of $36.7''$.

Each power law trial was repeated between 50 and 150 times to minimize shot noise uncertainty. A maximum likelihood analysis was performed to compare the observed pixel distribution to the predicted $P(D)$ from the simulations for a broad range of power-law models.

Figure 8.1 shows the theoretical $P(D)$ produced by noise-only simulations as well as the simulated best-fitting model, with maximum likelihood values (and 95% confidence limits) of $\delta = 2.7^{+0.18}_{-0.15}$ and $n_o = 1595^{+85}_{-238}$ mJy^{-1} deg^{-2}. As the number of sources per beam at the 0.1 mJy level is only about 0.1, the fluctuation analysis is limited by the noise level in the map rather than by source confusion, which yields ~ 1 source per beam at $S_\nu \approx 0.3$ mJy. The integral number count distribution, N, above 1 mJy is related to n_o by

$$n_o = (\delta - 1)N(> S)S^{\delta-1}. \tag{8.1}$$

Figure 8.2 shows the χ^2 map of the power-law parameter space, with the location of the minimum of $N(>1 \text{ mJy}) \simeq 940^{+50}_{-140}$ deg^{-2}.

In order to properly compare the fluctuation analysis results to the point source extraction number counts model of § 7.5, it is necessary to convert the $P(D)$ number counts constraint from 1 mJy to 4 mJy. This is because the latter model implements a 3 σ detection threshold, and consequently provides information on the number counts only above an observed flux density of $S_\nu \approx 4$ mJy. We therefore scale Equation 8.1 by a factor of $4^{1-\delta}$, and convert the normalization parameter A to the integral number counts with $N(> 4 \text{ mJy}) = 4A/(\delta - 1)$ for $\delta > 1$. Figure 8.1 shows the two number count models are in good agreement with each other, with the $P(D)$ minimum lying within the 68% confidence contour of the point source extraction method. The smaller value of the power-law index, δ, from the fluctuation analysis is likely the result of the greater dynamic range of flux densities that are included. Because of steepness of the power law index ($\delta \sim 3$), the factor of four decrease in flux density considered by the

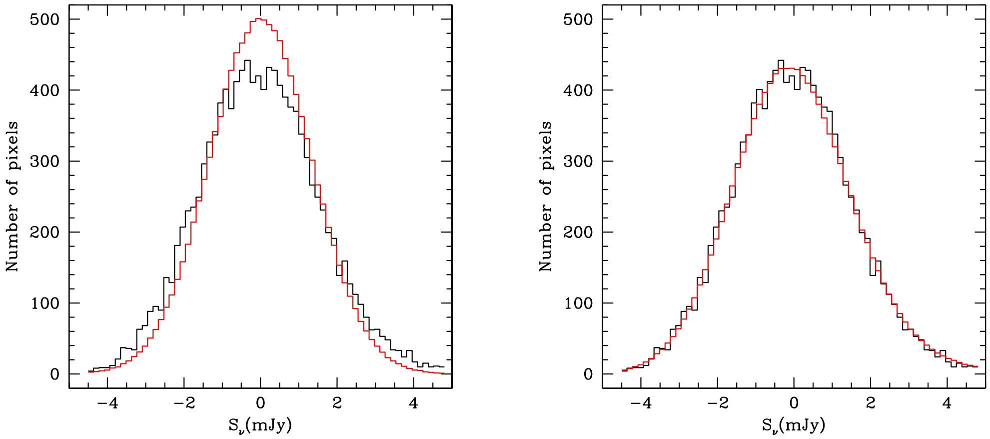

Figure 8.1 *Left:* Pixel flux density distribution ($P(D)$) of the Lockman Hole map shown in Figure 5.4 (black), overplotted with the pixel distribution produced by 100 realizations of a noise-only map (red). There are 66 bins in flux density, ranging from -4.5 to +4.8 mJy. The marked discrepancies between the two are a consequence of the signal in the actual map. *Right:* The actual ($P(D)$) as in the left panel (black), overplotted with the theoretical $P(D)$ produced by the best-fitting power-law model (red), with $\delta = 2.7$ and $n_o = 1595$ mJy^{-1} deg^{-2}. This model has $\chi^2 = 51.5$, with 59 degrees of freedom.

$P(D)$ analysis results in an order of magnitude increase in the integrated number of sources, which accounts for the much smaller uncertainties in the values of N and δ.

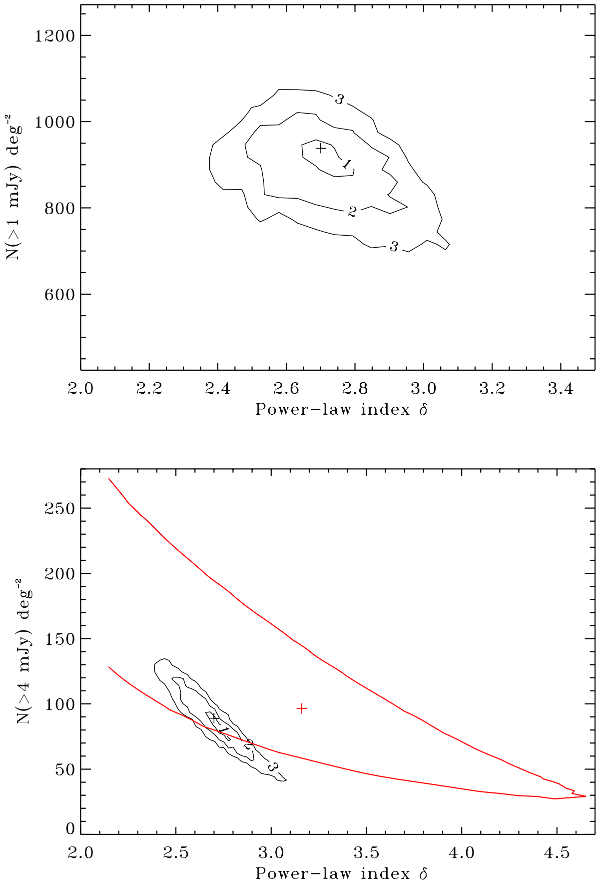

Figure 8.2 *Top:* Joint confidence limits for the fit of power-law integral number counts ($N > 1$ mJy) to the observed Lockman Hole $P(D)$ distribution. The minimum χ^2 value of 51.5, marked with a cross, is located at $\delta \simeq 2.7^{+0.18}_{-0.15}$ and $N(> 1 \text{ mJy}) \simeq 940^{+50}_{-140}$ deg^{-2}. The contours in $\Delta\chi^2$ represent 1, 2, and 3 σ confidence regions and correspond to $\Delta\chi^2$ values of 2.3, 6.17, and 11.8, respectively. *Bottom:* Joint confidence limits for the fit of the power-law integral number counts for $N > 4$ mJy (black), with a minimum χ^2 location of $\delta \simeq 2.7$ and $N(> 4 \text{ mJy}) \simeq 88.9$ deg^{-2}. Overplotted in red is the χ^2 minimum ($\delta = 3.2$, $N(> 4 \text{ mJy}) \simeq 96.3$ deg^{-2}) and 68% confidence region result from the point source extraction number counts model of § 7.5.

Chapter 9

Discussion

9.1 Comparison with Previous Number Count Results

A number of other groups have previously published number counts of submillimeter galaxies. Figure 9.1 shows selected recent results. These include surveys of blank-fields by SCUBA on the JCMT at 850 μm (Barger et al., 1999; Borys et al., 2003; Scott et al., 2002), observations of galaxies lensed by clusters, also using SCUBA at 850 μm (Blain et al., 1999; Chapman et al., 2002; Cowie et al., 2002; Smail et al., 2002), and blank-field surveys by MAMBO on the IRAM telescope (Greve et al., 2004). The Bolocam results are plotted as both the maximum likelihood cumulative number counts (computed from the DNC described in § 7.5), evaluated from 1 mJy to the maximum observed flux density (6.8 mJy), as well as the $P(D)$ maximum likelihood results of § 8.3. We also show the results of Blain et al. (2002), which model hierarchical galaxy formation and incorporate the effect of obscuration by dust. The number counts in the figure are not adjusted for the wavelength differences of the surveys.

The Bolocam result is in broad agreement with previous measurements; the maximum likelihood cumulative number counts are consistent with the 1200 μm measurement and below the 850 μm measurements, as expected if the same population of objects is being measured. The region of 68% probability in parameter space has been translated to cumulative number counts and is shown by the region between the dashed curves. This region does not correspond to the naive expectation of Poisson errors based on the number of detected sources. This is due to both the strong effect of the bias and the flux cutoffs imposed on the model. Because of the bias, it is inappropriate to assume that the number of observed sources in a bin can be used as a measure of the uncertainty in the underlying number counts in that bin. The effect of assuming an upper flux cutoff is particularly evident in the figure in the rapid drop of the cumulative counts as the cutoff is approached. This causes the error bars to be artificially small, as any model is constrained to be zero beyond this point. The maximum likelihood number count model presented here, as well as its errors, depends strongly on the exact low- and high-flux cutoffs assumed for the underlying distribution and consequently cannot be treated as definitive.

In addition to the caveats above, it should be borne in mind that the uncertainty of the flux bias discussed in § 5.4 (derived from the rms pointing error between the Bolocam galaxy candidates and coincident radio sources) introduces a systematic shift in the simple model of equation (7.6): the parameter A changes by an amount $(1 \pm \sigma_\epsilon/\epsilon)^{-\delta}$. This gives a steep dependence of the amplitude of the number counts on the calibration error and the presumed power-law index.

At high flux densities, where the survey is nearly complete and the effect of the bias is smallest, model-independent constraints may be obtained. In particular, the lack of any observed sources with flux density greater than 8 mJy has been used to place a 90% upper confidence limit on the cumulative number counts above 8 mJy; this is shown by the dashed horizontal line in the figure. This constraint depends only linearly on the calibration error. Bolocam appears to be measuring near the region where the number counts, based on both the 850 and 1200 μm measurements, would be expected to turn over, but because of the limited survey area, we do not strongly constrain the number counts at the bright end of the luminosity function.

9.2 Integrated Flux Density

The fraction of the FIRAS integrated far-infrared background light (Fixsen et al., 1998) measured by this survey can be computed in several ways. Summing the flux densities of all observed sources gives 85 mJy, or 3.9% of the FIRAS background over the survey area at 1.1 mm (8.0×10^{-22} W m^{-2} ster^{-1} Hz^{-1}). Subtracting out the expected mean flux of false detections gives 58 mJy, or 2.7% of the FIRAS background. Integrating the maximum likelihood DNC of the number count model from observed sources between 1 and 6.8 mJy (the maximum observed) gives 276 mJy, or $\sim$ 13% of the FIRAS background. Similarly, integrating the fluctuation analysis number count model from 1 to 10 mJy yields 7% of the FIRAS background. Since it seems plausible that the number counts do in fact steepen beyond the upper range of our observations, we conclude that at least $\sim$ 95% of the light from submillimeter sources lies below the 3 σ detection threshold of this survey and $\sim$ 90% below the minimum fluxes derived from our number counts models.[1]

---

[1] If we extrapolate the $P(D)$ results to below 1 mJy, we find that 20% of the 1.1 mm background would be resolved at the 0.3 mJy confusion limit of one source per beam, and 45% at 0.1 mJy.

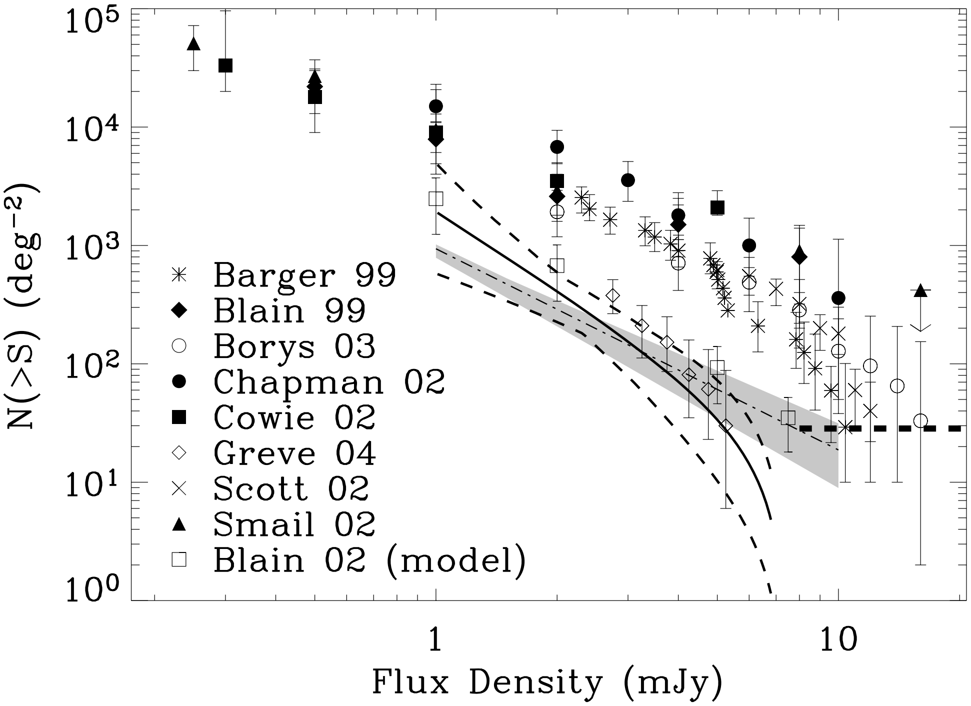

Figure 9.1 Previous measurements of the number counts of submillimeter galaxies, along with the new measurement with Bolocam. Previous surveys that used lensing by clusters are indicated by filled symbols; all other symbols indicate blank-field surveys. The solid line shows the integral of the Bolocam maximum likelihood differential number counts; the region between the dashed curves is the 68% confidence region of Fig. 7.5 translated into the range of possible cumulative number counts. The dash-dot line and shaded region represents the integral number counts and 95% confidence region from the $P(D)$ fluctuation analysis. The thick horizontal dashed line is the 90% upper confidence limit for sources brighter than 8 mJy for this survey. All surveys are at 850 μm, except for Bolocam at 1100 μm and Greve et al. (2004) (IRAM MAMBO) at 1200 μm. See §§ 7.5 and 7.6 for a description of the limitations of this model.

Chapter 10

SHARC II 350 μm Follow-up

10.1 The 350 μm SHARC II Galaxy Survey

Observations at multiple submillimeter wavelengths are vital both to confirm the Bolocam sources (as 6 false detections are expected from Monte-Carlo simulations) and to make photometric redshift and temperature estimates. The 350 μm SHARC-II observations combined with the Bolocam 1.1 mm galaxy survey provides a flux density ratio that is strongly dependent on redshift for a given temperature. This is because the rest wavelength corresponding to the observed wavelength of 350 μm with SHARC-II is near the peak of the grey-body spectrum (for a $z \sim 2$ galaxy at 40 K), and Bolocam's 1.1 mm observations climb the steep $\nu^{2+\beta}$ ($\beta \approx 1.5$) modified Rayleigh-Jeans side of the spectral energy distribution.

Follow-up observations of each of the Bolocam Lockman Hole galaxy candidates were taken with the Submillimeter High Angular Resolution Camera (SHARC II) at the Caltech Submillimeter Observatory. The observations were taken on three observing runs: 2004 March-April, 2005 January, and 2005 February. The brightest Bolocam sources (1 and 2) were observed over 8 hours of total integration time during the 2004 March-April run, although most of the run was lost due to poor weather. Bolocam sources 1 and 16 were observed over 18 hours of integration time during the 2005 January run, again with much of the run lost due to poor weather. The 2005 February run was characterized by much better weather, and all the Bolocam sources except for 1, 5, 8 and 16 were observed over 35 hours of integration time[1] . When combined with the observations of Bolocam sources 5 and 8 by Kovács et al. (2005), the entire Bolocam sample was observed over these observing runs.

Observations with SHARC II were taken in the point source observing mode, with a Lissajous (parametric sinusoidal curve) scan pattern using the SWEEP command of telescope. The Lissajous pattern was scanned in altitude and azimuth, with amplitudes of $30''$ and $20''$, respectively. When combined with the $2.6' \times 1.0'$ SHARC II field-of-view and $9''$ FWHM instrument beam size, this resulted in a uniform coverage region of $95'' \times 18''$, with a border of additional coverage ($60'' \times 40''$) outside this region. Each observation had a fixed length of 10 minutes to ensure uniform coverage even on individual scans. Integration times and the resulting depths of each of the SHARC II fields are listed in Table 10.1.

The reduction of the raw SHARC II data was accomplished with the use of the "deep" cleaning utility of the Comprehensive Reduction Utility for SHARC II[2] (CRUSH). Observations of pointlike galaxies, quasars, protostellar sources, H_{II} regions, and evolved stars were used to construct pointing models for each of the observing runs. Observations of the pointing sources were taken with a scan strategy identical to that of the science fields. A subset of the pointing sources were used for flux density calibration, with reference 350 μm flux densities obtained from the SHARC II website[3] .

Source extraction was performed on the CRUSH-cleaned maps, with each map (corresponding to a single Bolocam candidate) consisting of all of the individual scans co-added together. The algorithm was begun by doing a cut on the uniform coverage region, defined as the set of pixels for which the coverage is $\geq 60\%$ of the maximum per-pixel

---

[1] The primary weather measurement correlated with the SHARC II mapping speed is the CSO 225 GHz heterodyne, narrowband, "tipper tau" monitor, which measures the zenith atmospheric attenuation. The 2004 March-April, 2005 January, and 2005 February Lockman Hole observations yielded $\tau_{225\mathrm{GHz}}$ ranges and 75th percentiles of $\tau_{225\mathrm{GHz}} = 0.046 - 0.087$, $\tau_{75\%} = 0.076$, $\tau_{225\mathrm{GHz}} = 0.044 - 0.120$, $\tau_{75\%} = 0.093$ and $\tau_{225\mathrm{GHz}} = 0.030 - 0.074$, $\tau_{75\%} = 0.047$, respectively.

[2] http://www.submm.caltech.edu/~sharc/crush/index.htm

[3] http://www.submm.caltech.edu/~sharc/

Table 10.1. SHARC II Photometry and New Galaxy Candidates

Bolocam Source	SHARC II Source	SHARC II # 10 min. Scans	SHARC II/Bolocam Offset (")	Bolocam 2 σ Error Circle (")	SHARC II R.A (J2000.0)	SHARC II Dec (J2000.0)	S/N	S_ν (mJy)	σ (mJy)
1	7	30,16	13.2	21	10:52:57.1	57:21:01	3.7	38.0	14.0
2	8	17,23	15.8	21	10:51:18.6	57:16:36	3.5	20.9	7.9
3	10	20	9.1	21	10:52:13.0	57:15:46	3.2	14.0	5.6
”	11	20	17.3	21	10:52:14.0	57:16:02	3.1	15.1	6.2
4	21	20	(18.3)	22	10:52:04.8	57:18:39		≤ 15.4	
5	6 (Kovács 4)		15.0	22	10:52:30.9	57:22:06	5.9	40.4	8.6
6	1	5	12.0	22	10:51:14.1	57:14:21	6.8	63.6	18.4
”	9	5	18.0	22	10:51:17.8	57:14:20	3.3	27.6	10.8
7	20	15	(16.7)	22	10:51:28.6	57:30:50		≤ 10.7	
8	5 (Kovács 5)		16.3	23	10:52:38.8	57:24:38	6.2	40.5	8.1
9	18	14	(15.4)	23	10:53:05.0	57:15:08		≤ 19.6	
10	16	36	(22.4)	23	10:51:31.0	57:23:35		≤ 25.1	
11	19	13	(19.9)	23	10:52:49.0	57:13:01		≤ 18.9	
12	14	18	(1.5)	23	10:51:15.5	57:15:22		≤ 20.5	
13	17	13	(20.5)	23	10:52:34.9	57:18:13		≤ 23.7	
14	2	16	20.5	24	10:52:01.7	57:24:43	5.9	24.1	7.3
15	15	15	(24.0)	24	10:51:47.9	57:28:57		≤ 20.0	
16	13	93	1.6	25	10:52:27.3	57:25:13	3.0	44.0	18.3
17	12	16	6.0	26	10:52:00.6	57:24:21	3.1	15.5	6.3
(9)	3	14	-	23	10:53:08.3	57:15:01	4.8	28.4	9.2
(16)	4	93	-	25	10:52:32.3	57:24:48	3.8	37.0	13.4

Note. — SHARC II detections and 3 σ upper limits at each of the Bolocam sources, in order of descending brightness at 1.1 mm. The Bolocam sources in parentheses correspond to SHARC II detections well outside of the Bolocam 2 σ positional error circle, and are therefore believed not to be associated with the Bolocam source. Two SHARC II detections from Kovács et al. (2005) are also included. The SHARC II source numbers are listed in order of 350 μm S/N.

coverage. The uniform coverage region is a contiguous region in the center of each map. Next, an RMS in sensitivity units (the flux density of each pixel times the square root of the integration time for that pixel in units of mJy $s^{1/2}$) was computed in the uniform coverage region. This RMS is valid for the entire uniform coverage region since variations in coverage have been accounted for by the $t_i^{1/2}$ coverage normalization, where t_i is the total integration time for pixel i. All pixels with coverage-normalized flux densities exceeding 3 σ ("hot pixels") were flagged as potential sources. Then hot pixels were grouped into multi-pixel sources by making the maximal group of adjacent hot pixels, including those within $\sqrt{2}$ pixels (i.e., diagonally adjacent). The peak flux density, right ascension and declination of the source candidates were computed by centroiding two-dimensional Gaussians on the groups. The uncertainty in the flux density of each source is given by the pixel-to-pixel RMS at the centroid location of the source.

10.2 Positional Uncertainties

The large beam sizes of submillimeter and millimeter wave instruments (31″, 14″, 11″, and 9″ FWHM for Bolocam, SCUBA, MAMBO, and SHARC II, respectively) makes it difficult to identify likely optical and radio counterparts to the galaxy candidates. Despite the large beam sizes, however, individual sources can be centroided to much higher precision than the quoted beam size. To help constrain this issue of source matching between the various surveys, a positional error circle was estimated for each of the submillimeter and millimeter band detections. For the Bolocam detections, Monte Carlo simulations were performed by injecting sources into the timestream and running the reduction pipeline and source extraction algorithm. This simulation was repeated for a range of source flux densities. The resulting centroiding error as a function of flux density (5.4 - 9.1″) was added in quadrature with the RMS telescope pointing error (9.1″) to yield a range of 2 σ positional error circles of 21 - 26″. A similar approach was used to estimate the centroiding errors for SCUBA (Scott et al., 2002) and MAMBO

(Greve et al., 2004), yielding 2.2 - 10.4″ and 1.2 - 4.3″ respectively. When added in quadrature to the quoted pointing errors (4″ and 3″, respectively), this yields 2 σ positional errors of 9.2 - 22″ and 6.5 - 13″, respectively. As the centroiding error as a function of flux density for the SHARC II observations was not available, values of 3.0 - 4.0″ were empirically determined from the SHARC II centroiding fits of the Bolocam sources, which, when added in quadrature with the pointing error of 3.8″, yields 2 σ positional errors of 9.8 - 11″. These error circles were used to correlate the sources between the different surveys to find coincident detections.

10.3 Results

10.3.1 SHARC II 350 μm Detections

Postage stamp images of each of the SHARC II fields are shown in Figure 10.1. Each image has been cropped to 60″ × 60″, centered on the Bolocam source positions (dotted circle). The SHARC II source candidate list is presented in Table 10.1, where the sources are listed in order of Bolocam source number. Seven Bolocam galaxy candidates were detected by SHARC II at $> 3\sigma$ (Bolocam 1, 2, 3, 6, 14, 16, 17). Two of these sources (Bolocam 3, 6) were found to have two SHARC II counterparts. Two Bolocam candidates (5 and 8) were observed by Kovács et al. (2005) and are also included in the list. An additional two sources were detected in the survey (in the fields of Bolocam 2 and 9); they are not associated with the Bolocam source because their locations are well outside of the Bolocam positional error circles (see § 10.2). 3 σ upper limits are given for each of the Bolocam fields with no positive detections. Note that the flux density uncertainties in the last column of Table 10.1 include uncertainties of $\sim$ 20% due to calibration error (as determined by the dispersion of the calibration source flux densities). The correlation between the two source lists based upon the positional error circles and detection offsets is lower than expected, as only 2 of the 7 Bolocam sources with a single SHARC II counterpart have errors within 1 σ (5 are expected from a normal distribution). This may be due to underestimating the Bolocam pointing error (cf. § 5.3 and § 10.2).

10.3.2 Bolocam / SHARC-II Correspondence

In addition to the Bolocam 1.1 mm and SHARC II 350 μm detections, existing multiwavelength coverage (submillimeter, radio, infrared, optical, and X-ray) of the Lockman Hole was used to identify likely counterparts and characterize coincident sources. A detailed description of each of these surveys is found in Appendix D.1. A comprehensive summary of the counterparts to the Bolocam detections (including the coverage by each survey) is listed in Table D.1. Given the large size of the Bolocam beam, identifying likely counterparts requires a certain amount of judgement. Detailed maps of the sources can be found in Figure 10.2. Additional notes on individual objects are discussed below.

Bolocam.LE.1100.1 – We conclude that Bolocam source 1 is likely to be a submillimeter galaxy given the coincident Bolocam, MAMBO, and SHARC II detections. In addition, highly plausible radio, *Spitzer*, and faint optical counterparts exist.

Bolocam.LE.1100.2 – The SHARC II detection falls 16″ to the ENE, but contains both radio sources in its error circle. The two 20 cm radio sources (Yun et al., 2005; Biggs & Ivison, 2006) are unrelated due to their separation. We treat each of the radio sources separately when fitting photometric redshifts. The coincident northern radio source with bright optical counterparts has a low photometric redshift (see next section) and is likely to be a low-redshift galaxy as the SDSS survey concludes. Bolocam and SHARC II may also be detecting the Biggs & Ivison (2006) southern radio source, which has a very faint optical counterpart.

Bolocam.LE.1100.3 – The position of this 6.0 mJy Bolocam source is at the edge of the good coverage region of the SCUBA survey. All of the optical counterparts

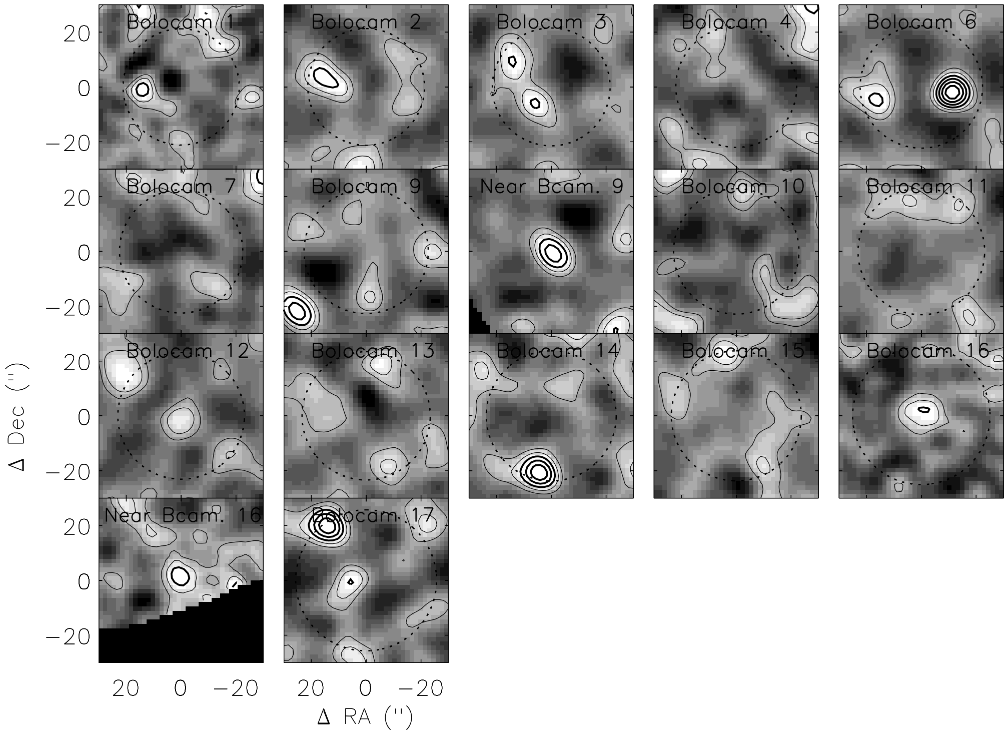

Figure 10.1 Postage stamp images (in sensitivity units of mJy $s^{1/2}$) of each SHARC II field, centered on the Bolocam source positions. Images have been cropped to $60'' \times 60''$. The dotted circles represent the 2 σ positional error circles of each Bolocam galaxy candidate. Overlayed are contours of signal-to-noise, with levels of 1, 2, 3, 4, 5, and 6. Contours of positive SHARC II detections ($S/N \geq 3$) are thicker than the others for clarity. Bolocam sources 5 and 8 are not included, as they were observed by Kovács et al. (2005).

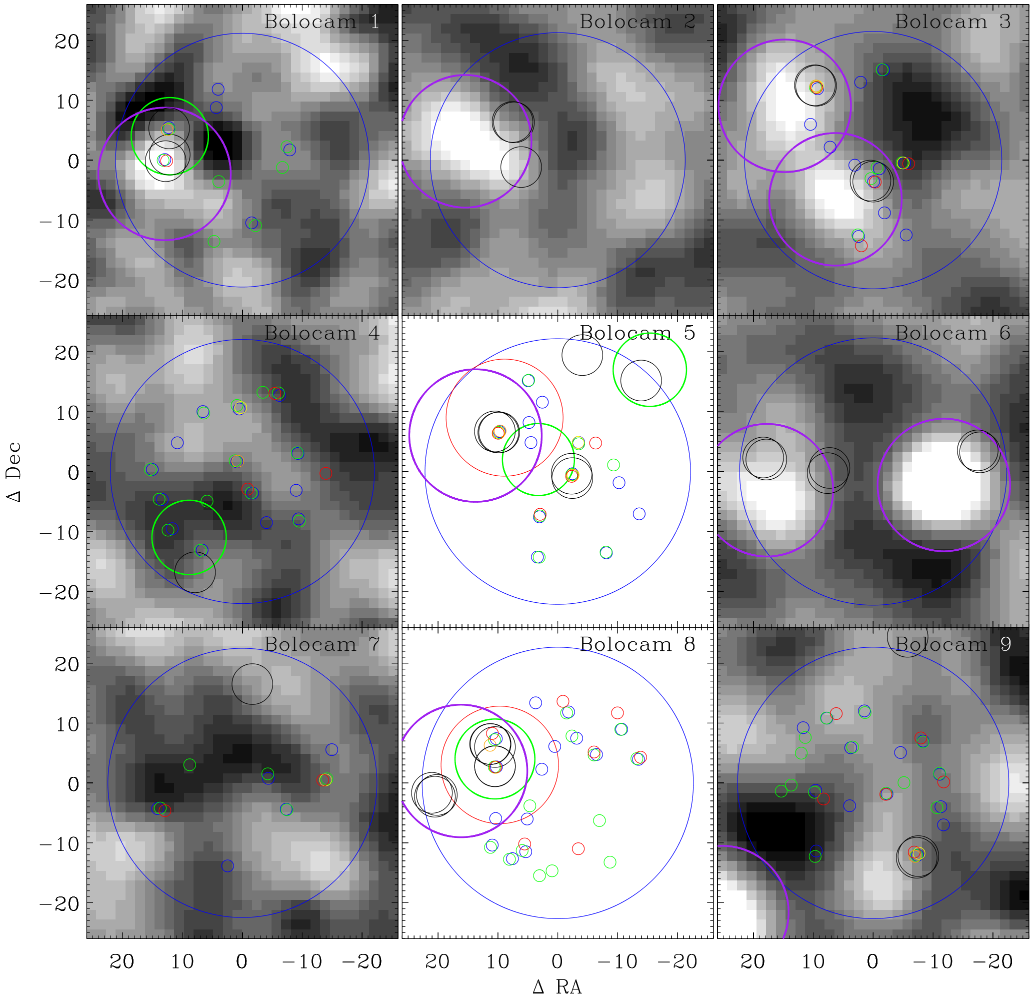

Figure 10.2 Plot of coincident multiwavelength detections of all 17 Bolocam sources, centered on the Bolocam positions. Sizes of the Bolocam, SCUBA, MAMBO, and SHARC II circles correspond to the 2 σ positional error circles. Black circles correspond to VLA radio detections by Yun et al. (2005), Ivison et al. (2002), Ciliegi et al. (2003), and Biggs & Ivison (2006). Smaller diameter circles correspond to the *Spitzer* 2.6, 4.5, 5.8, 8.0 IRAC and 24 μm MIPS bands.

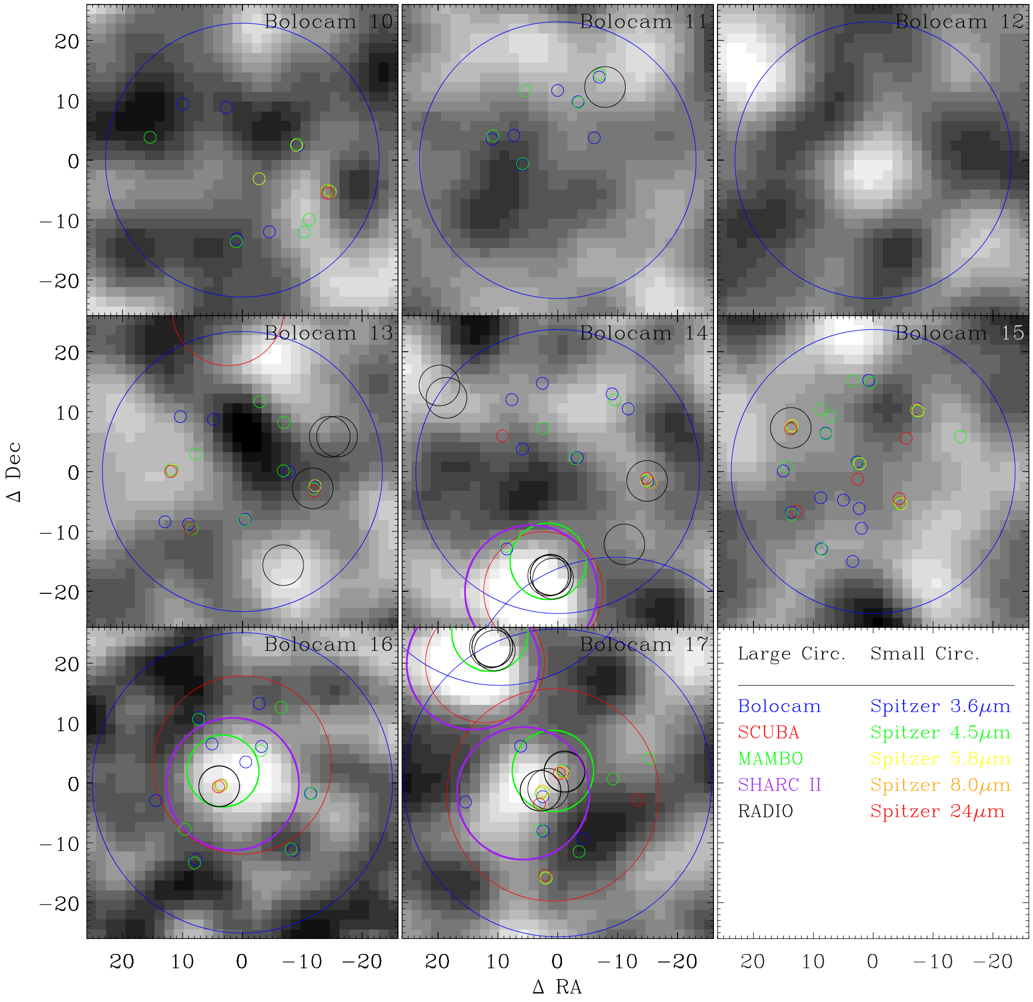

Figure 10.2 (continued) Plot of coincident multiwavelength detections of all 17 Bolocam sources, centered on the Bolocam positions. Sizes of the Bolocam, SCUBA, MAMBO, and SHARC II circles correspond to the 2 σ positional error circles. Black circles correspond to VLA radio detections by Yun et al. (2005), Ivison et al. (2002), Ciliegi et al. (2003), and Biggs & Ivison (2006). Smaller diameter circles correspond to the *Spitzer* 2.6, 4.5, 5.8, 8.0 IRAC and 24 μm MIPS bands.

to the radio sources are relatively bright (22 - 24 magnitude), although curiously, the SDSS catalog classifies the optical counterpart to the northeast radio source as a star. (Given the radio and 350 μm SHARC II counterparts, we conclude that the SDSS classification may be incorrect.) Given that both of the SHARC II sources have radio, *Spitzer*, and optical counterparts, each (or both) are likely candidates as submillimeter galaxies and each could contribute to the flux density of the Bolocam source. Note that when estimating photometric redshifts where source confusion may be present (for this Bolocam source and elsewhere), no attempt was made to partition the Bolocam flux density among multiple submillimeter sources (due to the large uncertainties in position).

Bolocam.LE.1100.5 – Four radio detections fall within the Bolocam positional error circle: one within the SCUBA and SHARC II error circles and just outside the edge of the MAMBO error circle, one on the edge of the MAMBO error circle, and the other two near the edge of the Bolocam positional error circle. The southwest radio source has 5-color SDSS photometry and is classified as a galaxy (extended). The fact that three of the radio sources lie outside both the SCUBA and SHARC II error circles makes them unlikely to be the correct counterpart of the submillimeter detections. We therefore choose the northeast radio source to be the more likely counterpart (which is confirmed by the fact that Chapman et al. 2005 were able to obtain a spectroscopic reshift for this submillimeter galaxy at this radio position, as discussed in § D.2).
A MAMBO detection located just outside the Bolocam error circle was not detected by SHARC II or SCUBA (3 σ upper limit of 35.4 mJy), but has a Chapman et al. (2005) spectroscopic redshift of 1.956. Due to the large size of the Bolocam beam, the Bolocam flux densities and positions may be influenced by source confusion.

Bolocam.LE.1100.6 – Two SHARC II counterparts fall within the Bolocam positional error circle, each with radio counterparts (with the eastern source containing two radio counterparts). The SDSS survey classifies both the radio source associated with the western SHARC II source and the eastern radio source associated with the eastern SHARC II source as galaxies. Each of the three radio sources may be contributing to the Bolocam flux density due to source confusion. We treat each of the radio sources separately when fitting photometric redshifts.

Bolocam.LE.1100.8 – Given the fact that the southern radio source (of the pair of two radio sources oriented N-S) has Bolocam, SCUBA, MAMBO, SHARC II, and *Spitzer* detections, along with a spectroscopic redshift, we conclude that this Bolocam source is real. Nevertheless, the northern radio source cannot be ruled out as a galaxy also contributing to the submillimeter fluxes.

Bolocam.LE.1100.14 – This 4.4 mJy Bolocam detection is likely influenced by source confusion, given three closely spaced submillimeter sources (SCUBA sources 1, 4, and 8, with the latter two lying near, but outside of the Bolocam positional error circle). The location of the southern radio source relative to the Bolocam position is greater than the 16″ radius used for the *Spitzer* counterparts catalog, and thus no *Spitzer* data is available. This set of coincident sources is the most likely counterpart to the Bolocam source. Just outside of the Bolocam error circle lies another 850 μm SCUBA detection (LE850.4) to the northeast, with a coincident Ivison et al. (2002) 20 cm radio source as well as published 3.6, 4.5, 5.8, and 8.0 μm *Spitzer* counterparts.

The SCUBA source that coincides with Bolocam source 14 (LH850.1) is also the brightest SCUBA source and has been the target of many published multi-wavelength studies. In addition to the extensive radio, infrared, optical and X-ray surveys discussed in § D.1, a faint (K $\simeq$ 23.5) galaxy counterpart was positively identified (Lutz et al., 2001) at the radio position. The source was found to be extended (20-30 kpc), clumpy (on subarcsecond scales) and very red (I - $K > 6.2$).

Bolocam.LE.1100.16 – We conclude that this Bolocam source is in fact a submillimeter galaxy, given the large number of multiwavelength detections and a radio source with a confirmed spectroscopic redshift.

Bolocam.LE.1100.17 – This 4.0 mJy Bolocam detection is likely influenced by source confusion, given two nearby submillimeter sources. The 850 μm SCUBA, 1.1 mm MAMBO, and 850 μm SHARC II coincident detections to the northeast are the likely counterparts to Bolocam source 14 and are discussed in detail in Bolocam.LE.1100.14. The SDSS catalog curiously classifies the northwest radio source as a star. We conclude that both the southeast and northwest radio sources associated with the Bolocam source may be submillimeter galaxies, given the large number of multiwavelength detections. While a confirmed spectroscopic redshift exists near the southeast radio source, self-consistent photometric redshifts and multiple optical counterparts at the radio position suggest that the spectroscopic redshift may not correspond to the radio / submillimeter sources (see § 11.4).

10.3.3 SHARC II Non-Detections

From extensive Monte-Carlo simulations of the Bolocam data set (see § 6.2), 6 false detections (Poisson distributed) are expected. This represents a large fraction (6/17) of the overall source catalog and is a consequence of the relatively low 3 σ detection threshold used in the source detection algorithm. Eight of the Bolocam sources (4, 7, 9, 10, 11, 12, 13, and 15) were found to show no secure counterparts at 350 μm, although two of the sources (Bolocam 9, 12) exhibit flux densities just below the 3 σ detection threshold (with a coincident radio detection for Bolocam source 9). Here we describe each of the SHARC II non-detections of the Bolocam sources in detail.

Bolocam.LE.1100.4 – A single radio counterpart (Biggs & Ivison, 2006) lies near the edge of the MAMBO positional error circle, with an SDSS classification of the optical counterpart as a galaxy. While well within the Bolocam positional error circle, the location of the radio source relative to the Bolocam position is greater than the 16$''$ radius used for the *Spitzer* counterparts catalog, and thus no *Spitzer* data is available. Given the coincident Bolocam and Mambo detections, along with a lack of SHARC

II and SCUBA detections, this source could possibly be a very high redshift galaxy ($z > 4$), such that the SED falls below the 3 σ detection threshold of the SCUBA 850 μm survey.

Bolocam.LE.1100.7 – The lack of multiwavelength observations makes it difficult to determine whether this Bolocam detection is real (and associated with the coincident radio detection). The lack of *Spitzer* and SHARC II counterparts to the radio source, however, leads us to believe that the Bolocam source may be a spurious detection.

Bolocam.LE.1100.9 – It is interesting to point out that the SHARC II upper limit in the Bolocam error circle is just below the 3 σ detection flux density threshold and coincides with the radio position. The lack of multiwavelength observations makes it difficult to determine whether this Bolocam detection is real. The presence of *Spitzer* counterparts and a possible dim SHARC II detection, however, leads us to believe that the Bolocam source may be real.

Bolocam.LE.1100.10 – Given the lack of counterparts, we conclude that there is little evidence to suggest that this detection represents a submillimeter galaxy and is likely a spurious detection.

Bolocam.LE.1100.11 – The lack of more multiwavelength data makes it difficult to determine whether this Bolocam detection is real. While lacking a SHARC II detection, the radio source with an SDSS classification as a galaxy (extended object) leads us to believe that the Bolocam source may be real.

Bolocam.LE.1100.12 – A portion of the Bolocam error circle lies outside the deep Ivison et al. (2005) optical Subaru R-band field. Similar to Bolocam source 9, we point out that the SHARC II upper limit in the Bolocam error circle is just below the 3 σ detection flux density threshold. The lack of more multiwavelength data makes it difficult to confirm whether this Bolocam detection is real.

Bolocam.LE.1100.13 – This Bolocam source lacks 850 μm SCUBA detections (although a SCUBA source is located just outside of the Bolocam positional error circle). We suggest that there is little evidence that the Bolocam detection represents a submillimeter galaxy and is likely a spurious detection.

Bolocam.LE.1100.15 – The lack of MAMBO and SHARC II counterparts makes it difficult to confirm the Bolocam detection. Nevertheless, the SDSS classification of the position coincident with the radio source as a galaxy (extended) leads us to believe that the Bolocam source may be real.

10.3.4 Submillimeter Spectral Energy Distributions

The submillimeter spectral energy distributions (SEDs) of the coincident SHARC / Bolocam detections is shown in Figure 10.3. Five of the 17 Bolocam galaxy candidates (5, 8, 14, 16, 17) have spectroscopic redshifts from Chapman et al. (2005, see Appendix D.2). In order to properly compare the SEDs, it is necessary to shift each of the SEDs to a common redshift. Thus, each observed SED was brought to a redshift of 2.0 (the mean redshift of the five Bolocam galaxies) using the spectroscopic redshifts. The composite SED of these five Bolocam galaxies can be seen in Figure 10.4.

In addition to redshifting the SEDs to align their rest wavelengths, a cosmological dimming term was applied by assuming a flat ($\Omega_k = 0$), $\Omega_\Lambda = 0.7$ cosmology. Finally, to account for variations in their intrinsic brightnesses, we normalize the flux densities of these five Bolocam galaxies by tying together their SEDs at the observed Bolocam wavelength of 1.1 mm. To account for the spread of the redshifted wavelengths of the 1.1 mm Bolocam observations, the flux densities were normalized to the modified blackbody model of § 12.3 based on the observations cited in the Blain et al. (2002) paper. The model assumes a single dust temperature of 40 K ($\beta = 1.6$) and is overplotted as a solid line in Figure 10.4. Note that only the Bolocam observations are constrained to pass through this model.

Upon inspection, we find that at least four of the five Bolocam galaxies with spectroscopic redshifts (5, 8, 14, 16) exhibit very similar SEDs in the submillimeter and

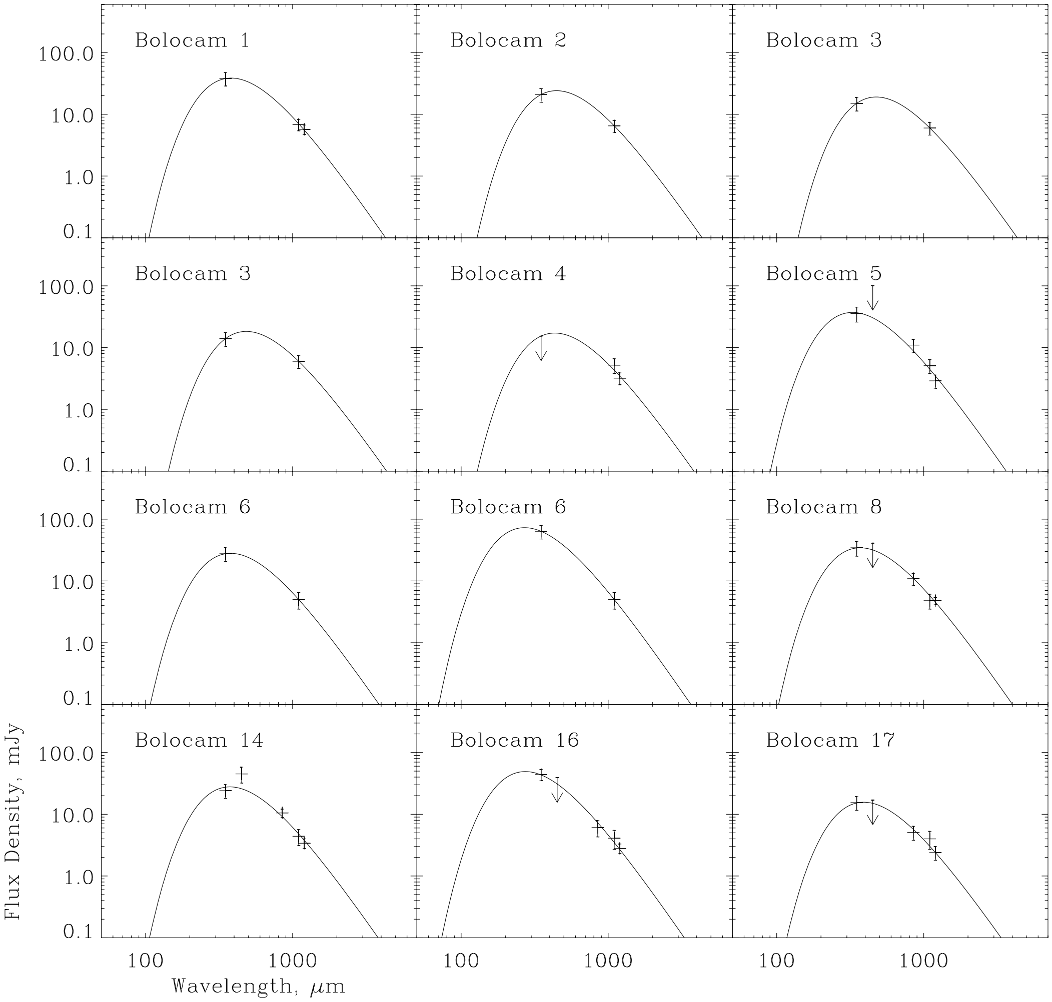

Figure 10.3 Submillimeter SEDs for all Bolocam galaxies detected in at least one other submillimeter waveband. The solid line represents a fit to a modified blackbody spectrum using the parameters of § 12.3.

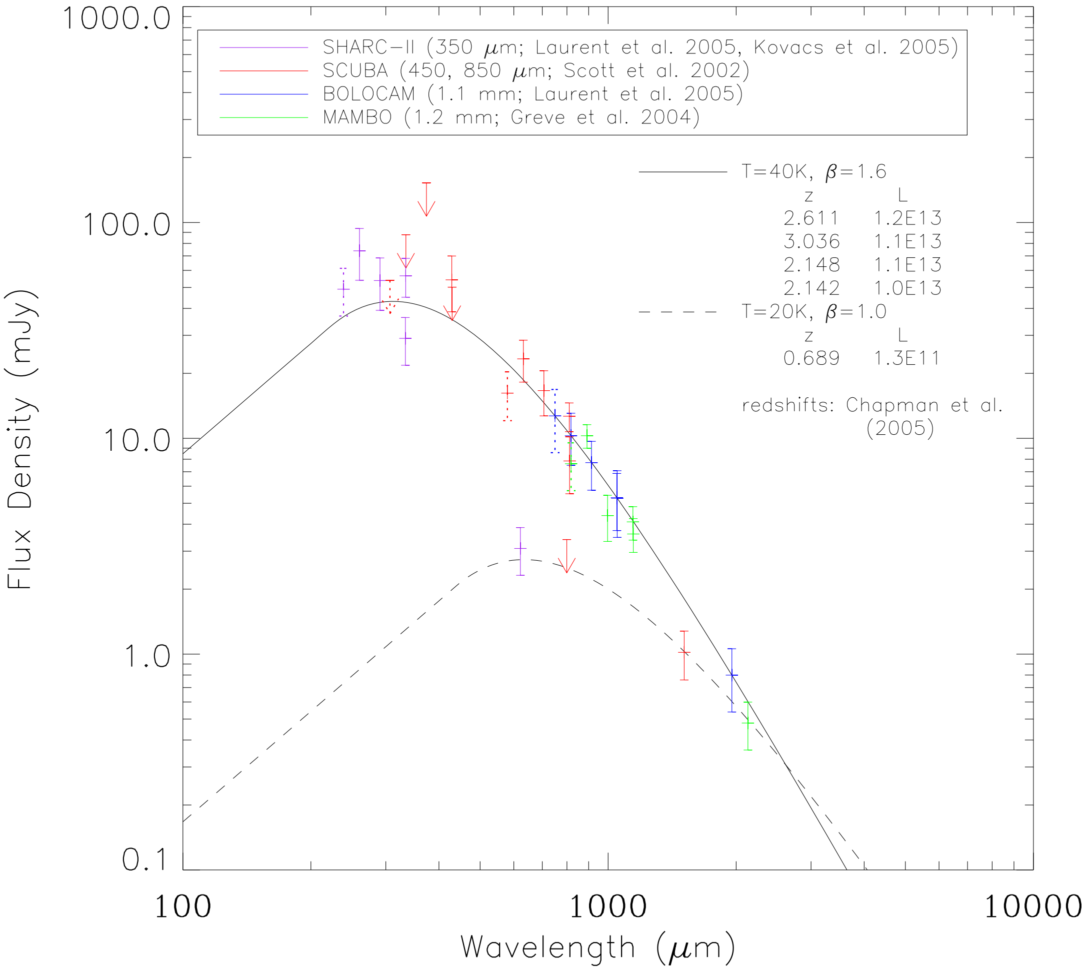

Figure 10.4 Composite submillimeter SED for the five Bolocam galaxies with spectroscopic redshifts (Bolocam 5, 8, 14, 16, and 17). The observed SEDs have all been redshifted to $z = 2.0$ using the spectroscopic redshifts, corrected for cosmological dimming, and their Bolocam 1.1 mm fluxes normalized to the modified blackbody model of § 12.3. The dotted points represent Bolocam source 17 assuming a redshift of 2.4 (the median photometric redshifts from § 11.2). The solid line represents a modified blackbody model (T = 40 K, $\beta = 1.6$) based on the composite SED of Blain et al. (2002, and references therein). The dashed line represents the same model, with T = 20 K and $\beta = 1.0$.

millimeter wavelengths. They are modeled adequately by the 40 K composite SED based on nearby dusty IRAS galaxies, high redshift submillimeter galaxies, gravitationally lensed high-redshift galaxies, and high redshift AGN. The Bolocam galaxy 17, however, appears to peak at a much higher wavelength and lower flux density than the others. We believe that there is enough source confusion to question whether the Chapman et al. (2005) redshift for this galaxy ($z = 0.689$) corresponds to the SED shown (see § 11.4). If the spectroscopic redshift is valid, the SED is modeled much better by a T = 20 K ($\beta = 1.0$) grey-body dust spectrum.

Chapter 11

Redshifts

11.1 Introduction

With the multiwavelength photometry of the Bolocam sources, we fit photometric redshifts using various models based on different portions of the SED. Photometric redshifts based on the far-IR-to-radio correlation were derived using the models of Carilli & Yun (1999) and Yun & Carilli (2002). The shape of the submillimeter and millimeter part of the spectrum was also fit without the radio points, assuming a blackbody emission spectrum modified by a dust emissivity term (Wiklind, 2003; Laurent et al., 2005). A brief description of each of the models, fitting methods, and the redshift results are discussed in the next section.

11.2 Redshift Techniques

This section attempts to briefly describe each of the five photometric redshift techniques used in this paper and the results of the fits when applied to the Bolocam galaxy candidates. The following section will compare the relative merits of each of the photometric redshift fitting techniques and discuss the results of redshift distributions.

1) FIR-Radio Spectral Index – Carilli & Yun (1999) used the semianalytic, linear relationships derived by Condon (1992) between the massive star formation rate and the radio synchrotron luminosity and far-IR dust emission from active star-forming galaxies to show that the spectral index between these two frequencies, $\alpha_{1.4}^{350}$, is a well behaved

function of redshift:

$$\alpha_{1.4}^{350} = -0.24 - [0.42 \times (\alpha_{\rm radio} - \alpha_{\rm submm}) \times \log(1+z)], \tag{11.1}$$

where we adopt the standard value in Condon (1992) of -0.8 for $\alpha_{\rm radio}$, and a value of +3.2 for $\alpha_{\rm submm}$ (an average of the spectral indices between 270 and 850 GHz for M82 and Arp 220. The relation is believed to be a result of relativistic electrons accelerated in supernova remnants (producing synchrotron radiation) and dust heated by the interstellar radiation field (with a thermal peak of $\sim 380\mu$m for a galaxy with $z = 2$ and T = 40 K). Photometric redshifts determined using only the Bolocam and radio flux densities are listed in Table 11.1. Redshift results from Bolocam sources with multiple radio counterparts are listed using the higher S/N detection in the case of coincident detections by independent surveys or are listed together in the case of multiple counterparts detected by a single group.

The error bars listed in Table 11.1 (and elsewhere throughout this paper) were obtained from Monte-Carlo simulations of the fits and represent statistical errors due to measurement uncertainty in the flux densities. The flux densities at each observed wavelength were varied about their mean value assuming a Gaussian distribution of flux errors. Each Monte-Carlo SED was then fit to the photometric redshift models with a standard, least-squares minimization fitting routine. Each simulation was repeated 1000 times, with the error bars quoted being the minimum-length 1 σ confidence intervals from the resulting histogram of redshifts. It should be noted that these confidence intervals represent only the statistical goodness of fit and that uncertainties in the templates themselves are expected to dominate the photometric redshift errors.

2) Entire FIR-Radio SED – Yun & Carilli (2002) utilized the entire Far-IR to radio spectral energy distribution to estimate photometric redshifts and SFRs. The redshift template is based upon the theoretical models of thermal dust emission, thermal bremsstrahlung (free-free) emission, and nonthermal synchrotron emission for dusty

starburst galaxies. Photometric redshift fits of the five Bolocam galaxy candidates (5, 8, 14, 16, 17) with spectroscopic redshifts (Chapman et al., 2005) are shown in Figure 11.1, with best-fit redshifts (and errors) also listed in Table 11.1. The solid lines in the figure represent the best fit spectrum to the submillimeter, millimeter, and radio point shown. The dotted line represents a second fit using the Yun & Carilli (2002) model, this time fixing the spectroscopic redshift and normalizing (varying only the SFR) to the submillimeter points.

3) Modified Blackbody – Wiklind (2003) found that observations of local ULIRGs exhibit a remarkably low dispersion in the far-IR to millimeter wavelengths ($\lambda > 50\mu$m), independent of whether the power source of the thermal emission is due to AGN or intense star formation. Wiklind (2003) fit a simple blackbody emission spectrum (modified by a dust emissivity term) to sample of 37 local ULIRGs from Klaas et al. (2001):

$$f_\nu \propto \epsilon_\nu B_\nu(T) \propto [1 - \exp(-\tau_\nu)] B_\nu(T), \tag{11.2}$$

where $B_\nu(T)$ is the Planck function evaluated at dust temperature, T, and frequency, ν, and τ_ν is the optical depth of the dust:

$$\tau_\nu = \left(\frac{\nu}{\nu_0}\right)^\beta .$$

Wiklind (2003) made no assumption about the Wien side of the spectrum, as only the submillimeter ($\geq 450\ \mu$m) and millimeter points were fit. Using the best-fit parameters from Wiklind (2003): $\beta = 1.8$, $\nu_0 = 1.2 \times 10^{12}$ Hz (250 μm), and $T_d = 68$ K, we fit photometric redshifts to the SHARC II 350 μm, SCUBA 450 and 850 μm, Bolocam 1.1 mm, and MAMBO 1.2 mm flux densities of the galaxies detected in our Bolocam survey. The two parameter fit (redshift and overall flux density normalization) yields redshifts for 9 of the 17 bolocam galaxies with ≥ 2 submillimeter/millimeter points. Seven of the Bolocam galaxies (Bolocam 7, 9, 10, 11, 12, 13, 15) have no counterpart in the submillimeter/millimeter and one (Bolocam 4) has detections only at 1.1 and 1.2 mm,

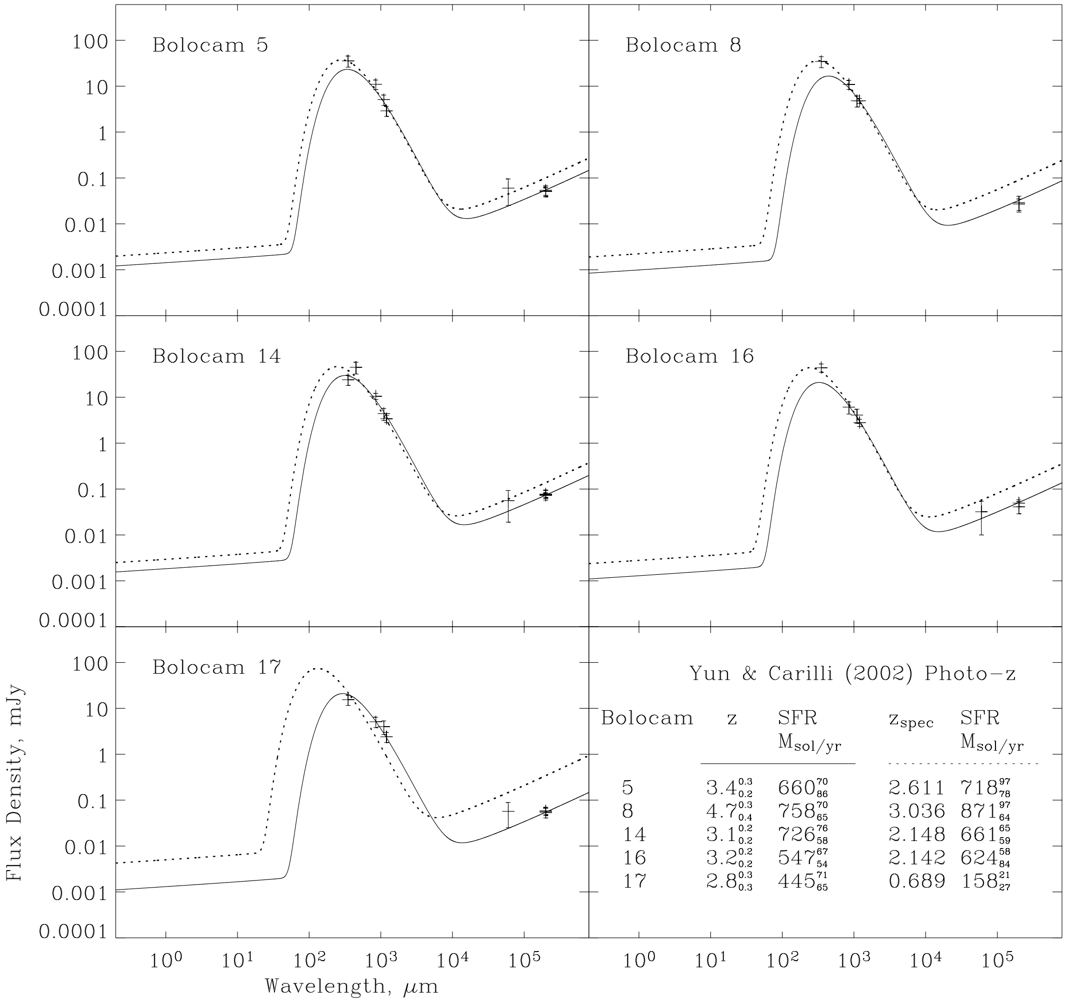

Yun & Carilli (2002) Photo−z

Bolocam	z	SFR $M_{sol/yr}$	z_{spec}	SFR $M_{sol/yr}$
5	$3.4^{0.3}_{0.2}$	660^{70}_{86}	2.611	718^{97}_{78}
8	$4.7^{0.3}_{0.4}$	758^{70}_{65}	3.036	871^{97}_{64}
14	$3.1^{0.2}_{0.2}$	726^{76}_{58}	2.148	661^{65}_{59}
16	$3.2^{0.2}_{0.2}$	547^{67}_{54}	2.142	624^{58}_{84}
17	$2.8^{0.3}_{0.3}$	445^{71}_{65}	0.689	158^{21}_{27}

Figure 11.1 Photometric redshift fits to five of the Bolocam galaxy candidates, using the model of Yun & Carilli (2002). The fits were limited to the submillimeter, millimeter and radio points shown. The solid line represents a two parameter fit, allowing both z and SFR to vary. The dashed line is the result of fixing the redshifts to the spectroscopic redshifts of Chapman et al. (2005), normalized to the submillimeter points. The best fit redshifts and SFRs, along with their error bars (from Monte Carlo simulations) are listed for each source.

Table 11.1. Photometric Redshifts

Bolocam 1.1 mm Number	$\mathrm{N_{Radio}}$	$\mathrm{N_{Submm}}$	$\mathrm{N}_{Spitzer}$	Carilli & Yun 1999 $\mathrm{z_{phot}}$	Yun & Carilli 2002 $\mathrm{z_{phot}}$	Wiklind 2003 $\mathrm{z_{phot}}$	Laurent et al. 2005 $\mathrm{z_{phot}}$	MRK231 $\mathrm{z_{phot}}$	ARP220 $\mathrm{z_{phot}}$	Chapman et al. 2005 $\mathrm{z_{spec}}$
1	2(S)	3	3	$4.6^{+0.3}_{-0.3}$	$4.1^{+0.3}_{-0.3}$	$3.2^{+0.4}_{-0.5}$	$3.2^{+0.3}_{-0.4}$	$15^{+1.4}_{-1.5}$	$3.0^{+0.2}_{-0.3}$	
”	1(N)	”	3	$4.6^{+0.3}_{-0.3}$	$4.1^{+0.3}_{-0.3}$	”	”	$1.8^{+1.0}_{-0.8}$	$2.0^{+0.7}_{-0.7}$	
2	2,1(N,S)	2	0	$2.2^{+0.2}_{-0.2}$, $3.9^{+0.3}_{-0.3}$	$0.6^{+0.1}_{-0.1}$, $2.9^{+0.7}_{-0.8}$	$4.2^{+0.6}_{-0.8}$	$3.9^{+0.4}_{-0.4}$			
3	2(NE)	2	5	$2.6^{+0.2}_{-0.2}$	$0.7^{+0.1}_{-0.1}$	$4.7^{+0.8}_{-0.7}$	$4.2^{+0.4}_{-0.5}$	$0.2^{+0.2}_{-0.2}$	$3.1^{+0.2}_{-0.2}$	
”	2(SW)	2	3	$3.7^{+0.3}_{-0.3}$	$1.6^{+0.3}_{-0.4}$	$4.9^{+0.8}_{-0.7}$	$4.3^{+0.5}_{-0.4}$	$10^{+0.9}_{-0.8}$	$2.3^{+0.7}_{-0.2}$	
4	1	2	0	$5.7^{+0.7}_{-0.8}$	$5.1^{+0.7}_{-0.9}$					
5	3(E)	4	5	$4.3^{+0.4}_{-0.4}$	$3.4^{+0.2}_{-0.3}$	$2.5^{+0.5}_{-0.4}$	$2.6^{+0.4}_{-0.5}$	$1.2^{+0.2}_{-0.2}$	$2.6^{+0.2}_{-0.2}$	2.611
6	2,2(E,W)	2(E)	0	$4.2^{+0.5}_{-0.4}$, $3.1^{+0.3}_{-0.3}$	$3.5^{+0.4}_{-0.5}$, $2.0^{+0.3}_{-0.3}$	$3.2^{+0.7}_{-0.7}$	$3.2^{+0.5}_{-0.6}$			
”	2	2(W)	0	$1.6^{+0.2}_{-0.2}$	$0.8^{+0.1}_{-0.1}$	$1.9^{+0.4}_{-0.5}$	$2.0^{+0.5}_{-0.6}$			
7	1	1	0	$4.2^{+0.6}_{-0.8}$	$3.6^{+0.6}_{-1.0}$					
8	2(N)	4	4	$5.1^{+0.5}_{-0.6}$	$4.7^{+0.3}_{-0.3}$	$3.1^{+0.4}_{-0.6}$	$3.1^{+0.3}_{-0.5}$	$0.6^{+0.3}_{-0.3}$	$2.4^{+0.6}_{-0.2}$	
”	1(S)	”	4	$5.1^{+0.6}_{-0.6}$	$4.7^{+0.4}_{-0.4}$	”	”	$0.7^{+0.4}_{-0.1}$	$3.1^{+0.2}_{-0.6}$	3.036
9	2	1	5	$3.9^{+0.4}_{-0.4}$	$3.2^{+0.5}_{-0.5}$			$1.3^{+0.2}_{-0.2}$	$1.8^{+0.2}_{-0.5}$	
10	0	1	0							
11	1	1	2	$3.2^{+0.4}_{-0.5}$	$2.5^{+0.4}_{-0.6}$			$0.4^{+0.2}_{-0.2}$	$0.8^{+0.3}_{-0.2}$	
12	0	1	0							
13	2,1(NE,SE)	1	0	$3.9^{+0.4}_{-0.4}$, $4.8^{+0.6}_{-0.6}$	$3.2^{+0.5}_{-0.4}$, $4.4^{+0.8}_{-0.8}$					
”	1(E)	”	4	$5.0^{+0.6}_{-0.7}$	$4.6^{+0.8}_{-1.0}$			$0.7^{+0.3}_{-0.2}$	$2.4^{+0.3}_{-0.5}$	
14	4	5	5	$3.7^{+0.4}_{-0.3}$	$3.1^{+0.2}_{-0.2}$	$3.2^{+0.3}_{-0.4}$	$3.2^{+0.3}_{-0.3}$	$7.3^{+0.6}_{-0.2}$	$3.0^{+0.2}_{-0.3}$	2.148
15	1	1	5	$4.1^{+0.5}_{-0.4}$	$3.5^{+0.6}_{-0.5}$			$0.6^{+0.2}_{-0.2}$	$1.0^{+0.2}_{-0.2}$	
16	2	4	5	$4.1^{+0.5}_{-0.5}$	$3.2^{+0.2}_{-0.2}$	$1.9^{+0.3}_{-0.5}$	$2.0^{+0.4}_{-0.4}$	$0.4^{+0.2}_{-0.2}$	$2.3^{+0.3}_{-0.2}$	2.142
17	3(SE)	4	10	$3.8^{+0.5}_{-0.4}$	$2.8^{+0.3}_{-0.3}$	$3.4^{+0.5}_{-0.7}$	$3.3^{+0.4}_{-0.4}$	$3.4^{+0.3}_{-0.3}$	$3.1^{+0.2}_{-0.2}$	0.689
”	1(NW)	”	5	$5.3^{+0.7}_{-0.8}$	$4.1^{+0.4}_{-0.5}$	”	”	$0.3^{+0.2}_{-0.2}$	$3.0^{+0.2}_{-0.6}$	

Note. — Best fit photometric redshifts of the Bolocam galaxy candidates using the models of Carilli & Yun (1999), Yun & Carilli (2002), Wiklind (2003), and Laurent et al. (2005), and cool and warm ULIRGs Arp 220 and MRK 231. $\mathrm{N_{Radio}}$, $\mathrm{N_{Submm}}$, and $\mathrm{N}_{Spitzer}$ are the number of coincident radio, submillimeter and *Spitzer* infrared points, respectively.

which is an insufficient wavelength spread in order to properly constrain the galaxy redshift using this two parameter model. Redshift results for each of the 9 Bolocam galaxies are listed in Table 11.1. The best fit models to the five galaxies with Chapman et al. (2005) redshifts (Bolocam 5, 8, 14, 16, 17) are shown in Figure 11.2.

Similar to the method of Wiklind (2003), Laurent et al. (2005) created a composite SED of nearby dusty *IRAS* galaxies, high-redshift submillimeter galaxies, gravitationally lensed high-redshift galaxies, and high-redshift AGNs (Blain et al., 2002, and references therein), and found fit parameters of $T = 40$ K, $\nu_0 = 3700$ GHz, and $\beta = 1.6$ for Equation 11.2. Redshift results for each of the 9 Bolocam galaxies are listed in Table 11.1. The best fit models to the five galaxies with Chapman et al. (2005) redshifts (Bolocam 5, 8, 14, 16, 17) are shown in Figure 11.2.

4) Near IR Stellar Bump – Egami et al. (2004) used the multiband imaging capabilities of the IRAC and MIPS IR cameras of the *Spitzer Space Telescope* to observe 38 VLA radio sources in the Lockman Hole. They classified the resulting IR SEDs into two types: those showing a clear near-IR stellar continuum hump at a rest wavelength of 1.6 μm (due to the minimum opacity of the H^- ion at 1.6 μm from photo-detachment and free-free transitions, which results in a local maximum in the the SEDs of cool stars, Sawicki 2002), and those with a featureless power-law continuum (from AGN). We fit the *Spitzer* IR counterparts of the Bolocam galaxies with each of these spectra, using the Egami et al. (2004) models of a cool ULIRG Arp 220 (from Silva et al., 1998) and a warm (dominated by an AGN) ULIRG Mrk 231. Only two fit parameters were used: the redshift, and an overall normalization. Photometric redshifts were fit for each of the 12 Bolocam galaxies (Bolocam 1, 3, 5, 8, 9, 10, 11, 13, 14, 15, 16, 17) with ≥ 2 IR *Spitzer* points. Three Bolocam galaxies (Bolocam 2, 6, 12) were outside of the field surveyed by Egami et al. (2004). Two galaxies (Bolocam 4, 7) have *Spitzer* counterparts, but due to the high density of *Spitzer* sources in the field, they could not be uniquely associated with the Bolocam sources (because of a lack of another coincident detection

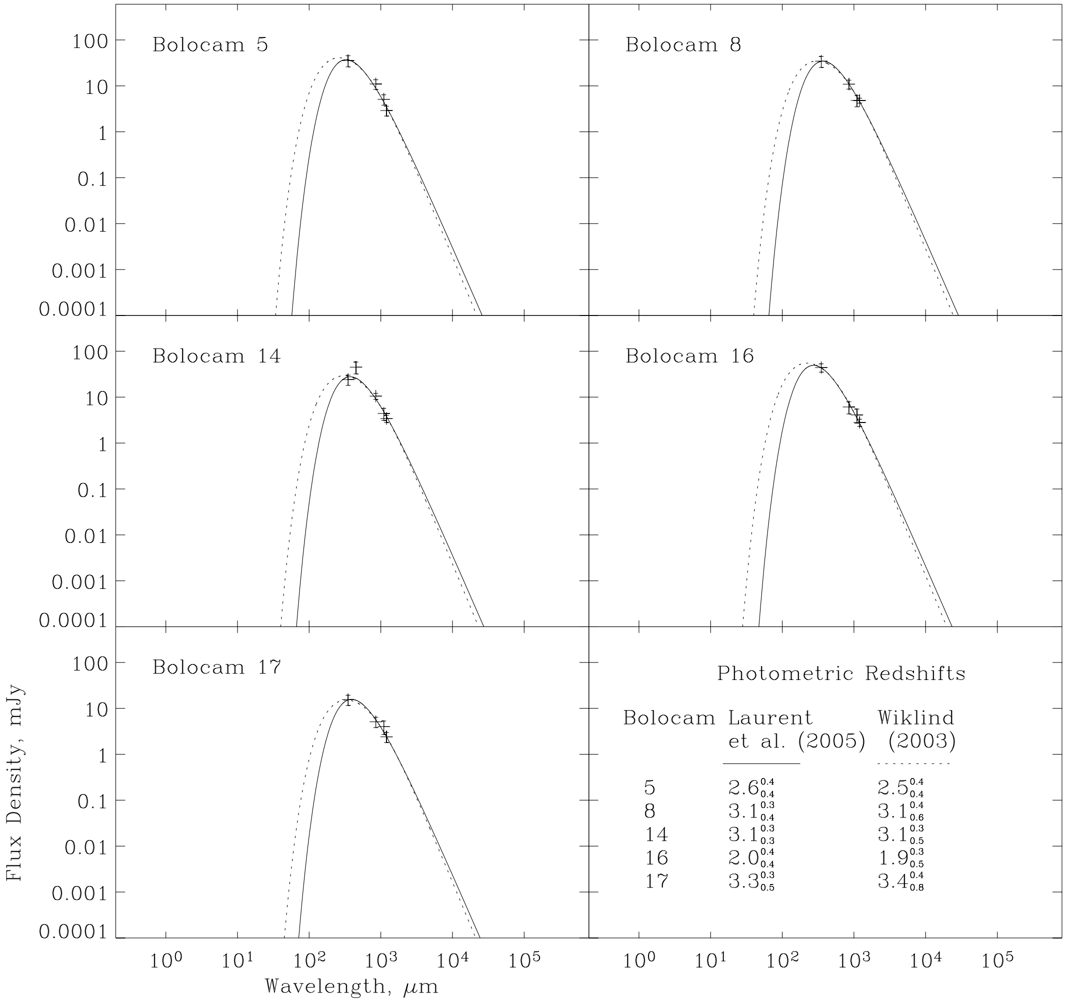

Photometric Redshifts

Bolocam	Laurent et al. (2005)	Wiklind (2003)
5	$2.6^{0.4}_{0.4}$	$2.5^{0.4}_{0.4}$
8	$3.1^{0.3}_{0.4}$	$3.1^{0.4}_{0.6}$
14	$3.1^{0.3}_{0.3}$	$3.1^{0.3}_{0.5}$
16	$2.0^{0.4}_{0.4}$	$1.9^{0.3}_{0.5}$
17	$3.3^{0.3}_{0.5}$	$3.4^{0.4}_{0.8}$

Figure 11.2 Photometric redshift fits to five of the Bolocam galaxy candidates, using the model SEDs of Laurent et al. (2005, solid line) and Wiklind (2003, dotted line). The fits were limited to only the submillimeter and millimeter points shown. The best fit redshifts, along with their error bars (from Monte Carlo simulations) are listed for each source.

in the submillimeter and/or radio). The best-fit photometric redshifts for both Arp 220 and Mrk 231 (fitting only the *Spitzer* near- and mid-infrared points) are shown in Figure 11.3, with the resulting redshifts also listed in Table 11.1.

11.3 Comparison of Photometric Redshift Techniques

Comparing the results of each of the photometric redshift techniques with the spectroscopic redshifts of Chapman et al. (2005) yields widely varying degrees of agreement. Histograms of redshift errors for each of the photometric redshift models (other than Carilli & Yun, 1999, in which coincident radio detections were treated separately) are shown in Figure 11.4. The histogram from fitting models of Arp 220 and Mrk 231 to the *Spitzer* IRAC and MIPS observations are the fits that result in the lowest residual χ^2 (Arp 220 for Bolocam 5, 8, 14, and 16, and Mrk 231 for Bolocam 17).

The Yun & Carilli (2002) model (as well as Carilli & Yun, 1999) yields systematically high photometric redshifts compared to the spectroscopic redshifts by Chapman et al. (2005). The comparison of model SEDs for photometric (solid line) and spectroscopic (dotted line) redshifts in Figure 11.1 suggests that SED data points at the extreme ranges of wavelength coverage strongly influence the model fit and that the systematic tendency to derive a high redshift is primarily driven by the lower than expected radio continuum flux density. This is supported by the fact that fits to only the submillimeter and millimeter-wave points yield much more accurate photometric redshifts (see below). This is perhaps not surprising, given recent evidence (Chapman et al., 2005) suggesting a large degree of dispersion in the radio-to-far-IR correlation at higher redshift. Nevertheless, it is unlikely that the Yun & Carilli (2002) model template, which is derived from the ensemble average of 23 infrared luminous galaxies in the local universe, is systematically biased by radio bright objects because $\geq$98% of all FIR-selected galaxies follow the well known and tight radio-FIR correlation, independent of FIR luminosity (Yun, Reddy, & Condon, 2001). Aside from Bolocam source

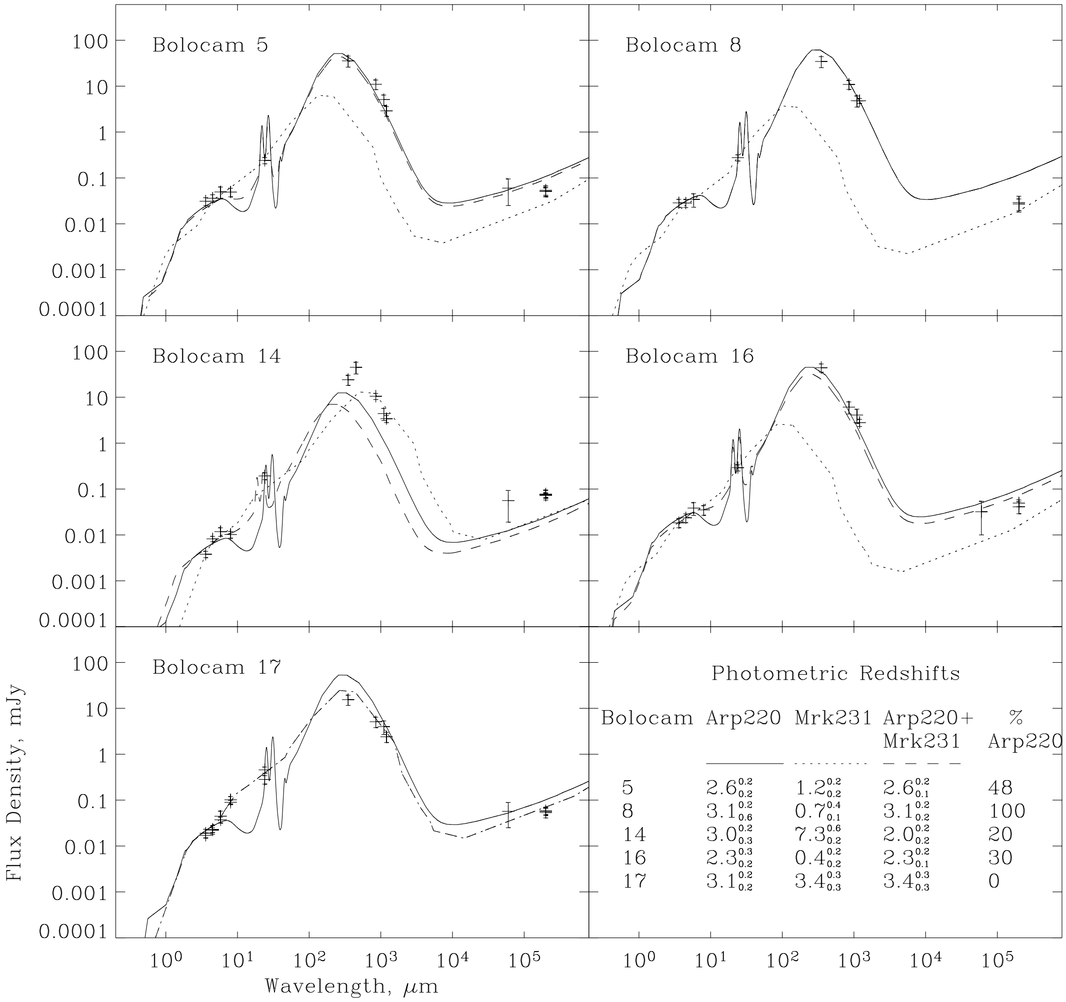

Photometric Redshifts

Bolocam	Arp220	Mrk231	Arp220+ Mrk231	% Arp220
	———	·········	— — — —	
5	$2.6^{0.2}_{0.2}$	$1.2^{0.2}_{0.2}$	$2.6^{0.2}_{0.1}$	48
8	$3.1^{0.2}_{0.6}$	$0.7^{0.4}_{0.1}$	$3.1^{0.2}_{0.2}$	100
14	$3.0^{0.2}_{0.3}$	$7.3^{0.6}_{0.2}$	$2.0^{0.2}_{0.2}$	20
16	$2.3^{0.3}_{0.2}$	$0.4^{0.2}_{0.2}$	$2.3^{0.2}_{0.1}$	30
17	$3.1^{0.2}_{0.2}$	$3.4^{0.3}_{0.3}$	$3.4^{0.3}_{0.3}$	0

Figure 11.3 Photometric redshift fits to five of the Bolocam galaxy candidates, fitting the *Spitzer* near- and mid-infrared points to Egami et al. (2004) models of a cool ULIRG Arp 220 (solid line, from Silva et al., 1998) and a warm (dominated by an AGN) ULIRG Mrk 231 (dotted line). The (sub)millimeter and radio points were not used in the fit and are shown only for reference. The dashed line represents a linear combination of the two models). The best fit redshifts along with their error bars (from Monte Carlo simulations) are listed for each source.

17 whose spectroscopic redshift by Chapman et al. (2005) appears suspect (see § 11.4), these comparisons suggest that the observed radio continuum in Bolocam galaxies is 2-5 times fainter than predicted by the synchrotron flux densities (which dominate thermal brehmsstrahlung by a factor of ~ 13 at 20 cm) from the low-redshift ULIRGs for which the local FIR-radio correlation was derived (see further discussions in 12.2).

In contrast to the far-IR-to-radio correlation photometric redshift techniques, both the Wiklind (2003) and Laurent et al. (2005) modified blackbody curves correctly estimate the redshifts for three of the five Bolocam galaxies with spectroscopic redshifts (within the uncertainties of the photometric redshift techniques). The strength of the submillimeter / millimeter-only photometric redshift technique is twofold. First, while abandoning the radio points limits the number of points (as few as two, in some cases) to which we may fit a model, we ensure that the physics that dominates the region of the spectrum to which we are fitting is directly relevant to star formation-heated dust emission. Synchrotron radiation, by contrast, is dependent upon high energy electrons streaming through interstellar magnetic fields, whose properties may vary as a function of environment (e.g. inverse-Compton losses for cosmic rays with higher CMB energy densities at high redshift – see § 12.2). Indeed, these galaxies are typically at least an order of magnitude more luminous than the low-redshift, infrared-luminous galaxies from which the FIR-radio correlation was derived.

Second, having the Bolocam 1.1 mm flux densities on the Rayleigh-Jeans side of the spectrum and the SHARC II 350 μm flux densities near the peak of the SED makes the 350 μm/1.1 mm flux density ratio a strong function of redshift. This can be seen in Figure 11.5, which shows the flux density ratios between various wavebands based on the Laurent et al. (2005) model SED. The importance of the SHARC II 350 μm waveband is apparent. For intermediate to high ($z < 5$) redshifts, the SHARC II flux density drops rapidly as a power law ($\sim \nu^{-1.7}$ due to the hotter components of dust) with redshift on the Wien side of the spectrum, while the millimeter-wave climbs up the steep Rayleigh-

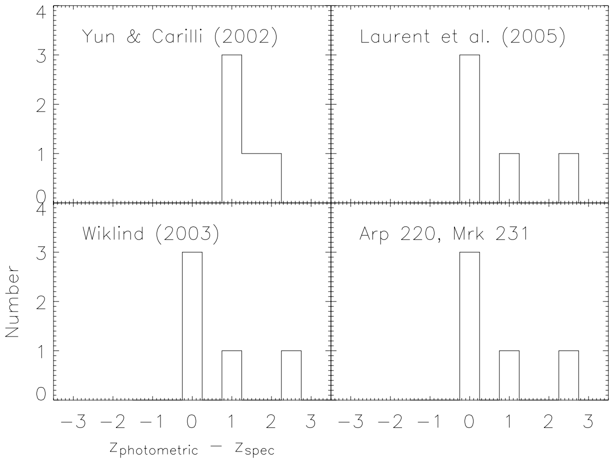

Figure 11.4 Histogram of photometric redshift errors for various models compared to the spectroscopic redshifts of Chapman et al. (2005). Yun & Carilli (2002) assume the far-IR to radio correlation while both Wiklind (2003) and Laurent et al. (2005) model the submillimeter and millimeter portions of the spectrum. The lower right frame is a fit of the near- and mid-infrared points to models of Arp 220 and Mrk 231 (Egami et al., 2004).

Jeans portion of the SED. Photometric redshifts using the 450 or 850 μm wavebands are less sensitive than the 350 μm / 1.1 mm wavebands. Extending this analysis shows the discriminatory power of the BLAST and *Herschel* space telescope 250 μm bands in conjunction with a millimeter waveband, although the far-IR waveband begins to probe a range of hotter dust temperatures. (The flux density ratio of these wavebands may not be well correlated, as discussed in § 12.1.) BLAST (Balloon-borne Large-Aperture Submillimeter Telescope, Devlin et al., 2001) is a balloon-based instrument which incorporates a 2-meter primary mirror and is equipped with large-format bolometer cameras operating at 250, 350, and 500 μm which, when complete, will provide the first sensitive large-area (0.5-40 deg^2) submillimeter surveys at these wavelengths. The bolometer arrays are prototypes of the Spectral and Photometric Imaging Receiver (SPIRE) focal plane cameras for the *Herschel* satellite (Griffin, Swinyard & Vigroux, 2001), which will further investigate the formation and evolution of AGNs and star formation in high redshift submillimeter galaxies.

It is important to note that while both the Wiklind (2003) and Laurent et al. (2005) modified blackbody curves both produce reasonably accurate photometric redshifts (and produce nearly identical SEDs on the Rayleigh-Jeans portion of the spectrum), they make substantially different assumptions about the dust properties: $T_{\rm dust}$ and β are 68 K and 1.8 for the Wiklind (2003) model SED and 40 K and 1.6 for the Laurent et al. (2005) model SED. This points to the degeneracy of the dust temperature and the grain emissivity index. While the shapes of the submillimeter SEDs are reasonably modeled by either dust model and thus predict photometric redshifts with some accuracy, essentially no information about the dust temperatures can be inferred. In fact, representing the dust SED with two (or more) components produces similar χ^2 values (and thus similar redshifts), with both temperatures *lower* than that of the single dust temperature model (Wiklind, 2003).

The photometric redshifts determined by fitting the *Spitzer* infrared observations yield redshifts that are equivalent to both the Laurent et al. (2005) and Wiklind (2003) model SEDs. This confirms the conclusions of Egami et al. (2004), in which starburst-dominated galaxies (”cold”) show remarkably similar SEDs in the infrared. The resulting photometric redshifts are highly sensitive to the 1.6 μm continuum hump (and PAH features), with a sharp minimum in χ^2. (The ARP 220 fits may be biased towards particularly good fits as 4 of the 5 galaxies with spectroscopic redshifts lie between $2 \lesssim z \lesssim 3$, which is optimal for the 8 μm PAH feature to be shifted into the observed 20 μm IRAC waveband.) AGN-dominated (”warm”) galaxies also show very similar SEDs, but lacking a strong continuum feature in the infrared, are subject to larger redshift fitting uncertainties; a brighter, higher redshift galaxy is characterized by a similar shape in the infrared portion of the SED as a cooler, low-redshift galaxy, with the Wien side of the spectrum well-modeled with a power-law (Blain et al., 1999).

11.4 Bolocam Source 17: Spectroscopic Misidentification?

We bring special attention to photometric redshift analysis of Bolocam source 17 (corresponding to SCUBA source 8), as the Laurent et al. (2005), Wiklind (2003), and *Spitzer* IR models are consistent in overpredicting the redshift of this galaxy ($z_{\rm spec}$ = 0.689) by $\geq 4\sigma$ ($z_{\rm phot} = 3.3^{0.4}_{0.5}$, $3.4^{0.6}_{0.6}$, and $3.4^{0.3}_{0.3}$, respectively). We point out that the large offset between the spectroscopic and photometric redshifts is possibly the result of source confusion, as two radio sources (both with *Spitzer* and optical counterparts) fall near the center of the Bolocam, SCUBA, MAMBO, and SHARC II error circles, within $4''$ of each other. (Egami et al. 2004 refer to the northwest and southeast radio sources as LE850.8a and LE850.8b, respectively.) The northwest radio source is believed by Lehmann et al. (2001) to be the counterpart to the ROSAT X-ray emission, who find a redshift of 0.974 using optical Keck spectroscopy. Using XMM-Newton observations, however, Ivison et al. (2002) conclude that the X-ray source corresponds to the southeast radio source. Indeed, the linear fit of a combination of ARP 220 and MRK 231

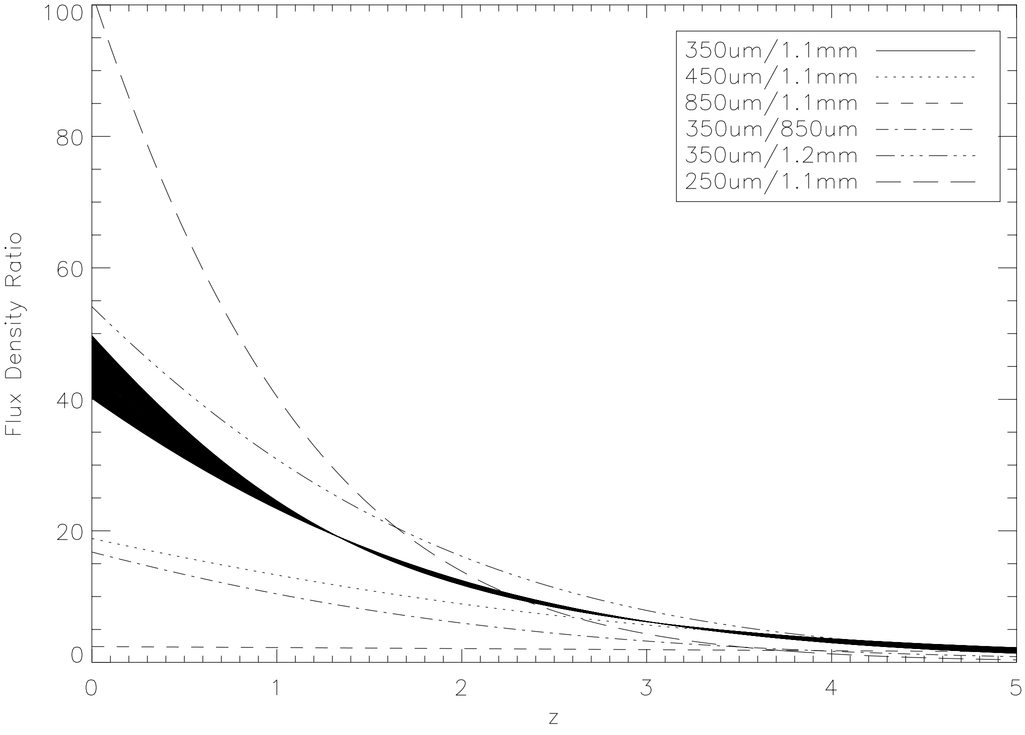

Figure 11.5 Flux density ratio between various wavebands assuming the submillimeter galaxy model SED of Laurent et al. (2005). The model is based on the composite SED of nearby dusty IRAS galaxies, high-redshift submillimeter galaxies, gravitationally lensed high-redshift galaxies, and high-redshift AGNs (Blain et al., 2002, and references therein). The Laurent et al. (2005) model assumes dust parameters of $T = 40$ K, $\nu_0 = 3700$ GHz, $\beta = 1.6$, and a power law of $f_\nu \propto \nu^{-1.7}$ to model the hotter dust components on the Wien side of the spectrum. The shaded line represents the ratio of the SHARC 350 μm and Bolocam 1.1 mm wavebands, with the thickness corresponding to the difference between the Laurent et al. (2005) and Wiklind (2003) model SEDs.

ULIRG models to the *Spitzer* points coincident with the southeast radio source yields a 100% warm (AGN dominated) component. It is near this radio position that Chapman et al. (2005) find a spectroscopic redshift of 0.689. In fact, the X-ray emission observed with both instruments appears to fall between these two radio sources. Optical R-band images from both Yun et al. (2005), and Ivison et al. (2005) show multiple optical counterparts at the southeast radio source position. Furthermore, the spectroscopic position quoted by Chapman et al. (2005) appears to coincide with an optical source $\sim 2''$ to the south of the southeast radio source, a source detected with four-color SDSS photometry (in addition to Yun et al. 2005 and Ivison et al. 2005 R-band photometry) and cataloged as a low-redshift galaxy. We conclude that it is possible that the submillimeter detections may either be suffering from source confusion from two or more galaxies, or that the Chapman et al. (2005) redshift corresponds to a source other than that of the southeast radio detection. If the latter is true, then the consistent redshifts predicted by the Laurent et al./Wiklind (2005, 2003) and *Spitzer* IR models may further point to the accuracy of these photometric redshift techniques.

Chapter 12

Discussion

12.1 IR Spectrum

SEDs over the entire IR-radio spectral range of the five Bolocam galaxies with spectroscopic redshifts are shown in Figure 12.1. These spectra have the same redshift, cosmological dimming, and normalization corrections as in Figure 10.4. While four of the five galaxies have closely correlated spectra in the submillimeter region of the spectrum, the infrared spectra (*Spitzer* 3.6, 4.5, 5.8, and 8.0 μm IRAC and 24 μm MIPS observations) exhibit a large degree of dispersion. This dispersion may be the result of several things: 1) Because the spectra have been normalized to a $T = 40$ K ($\beta = 1.6$) spectrum at their 1.1 mm Bolocam flux densities to account for intrinsic brightness variation between the galaxies, the normalization will result in an artificial reduction in the submillimeter flux density dispersions. This effect is not likely to dominate, as the flux density normalization has a $\sim 10\%$ effect on the flux densities of the galaxies. 2) The *Spitzer* detection associated with Bolocam source 14 lies systematically low compared to the other three galaxies well-modeled by a T=40 K dust spectrum. While these *Spitzer* observations (Egami et al., 2004) are from a different data set than the remaining *Spitzer* observations (this work), it is unlikely that their flux densities are systematically uncertain by nearly an order of magnitude. 3) The 40 K dust temperature model of the submillimeter portion of the spectrum for Bolocam sources 5, 8, 14, and 16 assume a single dust temperature for each of the four sources. The temperature fit parameter is somewhat degenerate with other fit parameters, including the critical frequency, ν_0, where the optical depth of the dust is unity. Thus, if Bolocam source 14 has a lower characteristic dust temperature, then the infrared portion of the 40 K model will significantly overestimate the infrared flux density. Chapman et al. (2005) estimates the temperature of Bolocam source 14 to be 33 K from two photometric points (850 μm SCUBA and 1.4 GHz VLA radio observations) and the dust SED templates of Dale & Helou (2002). This temperature uncertainty likely dominates our uncertainty in matching the infrared flux densities. 4) In addition to heating by the ultraviolet and optical flux density from young stars associated with ongoing star formation, the thermal dust emission responsible for the bright submillimeter flux densities may be contributed to by an energetic AGN. While not dominating the total bolometric output from the galaxy, they may have a non-negligible (20%) contribution (Alexander et al., 2004). If this is the case, then the shape of the infrared continuum may be vary according to the relative contribution of star formation rates for these galaxies. 5) Another possible explanation for the larger dispersion in *Spitzer* infrared flux density as compared to our single dust temperature model may be from the fact that the infrared flux densities trace separate epochs of star formation within the galaxy. It is plausible that the dust heated by the ultraviolet and optical flux density from from current star formation is not well correlated to the current infrared flux density of older stars (from previous star formation). Furthermore, models of UV to millimeter emission of star clusters embedded in optically thick giant molecular clouds (GMCs) suggest that the near-infrared to far-infrared portion of starburst galaxy SEDs vary considerably with age of the starburst (Efstathiou, Rowan-Robinson, & Siebenmorgen, 2000).

12.2 Radio Spectrum / FIR-Radio Correlation

The composite SED (including the radio points) of the 5 Bolocam sources with spectroscopic redshifts is shown in Figure 12.1. Two interesting observations can be

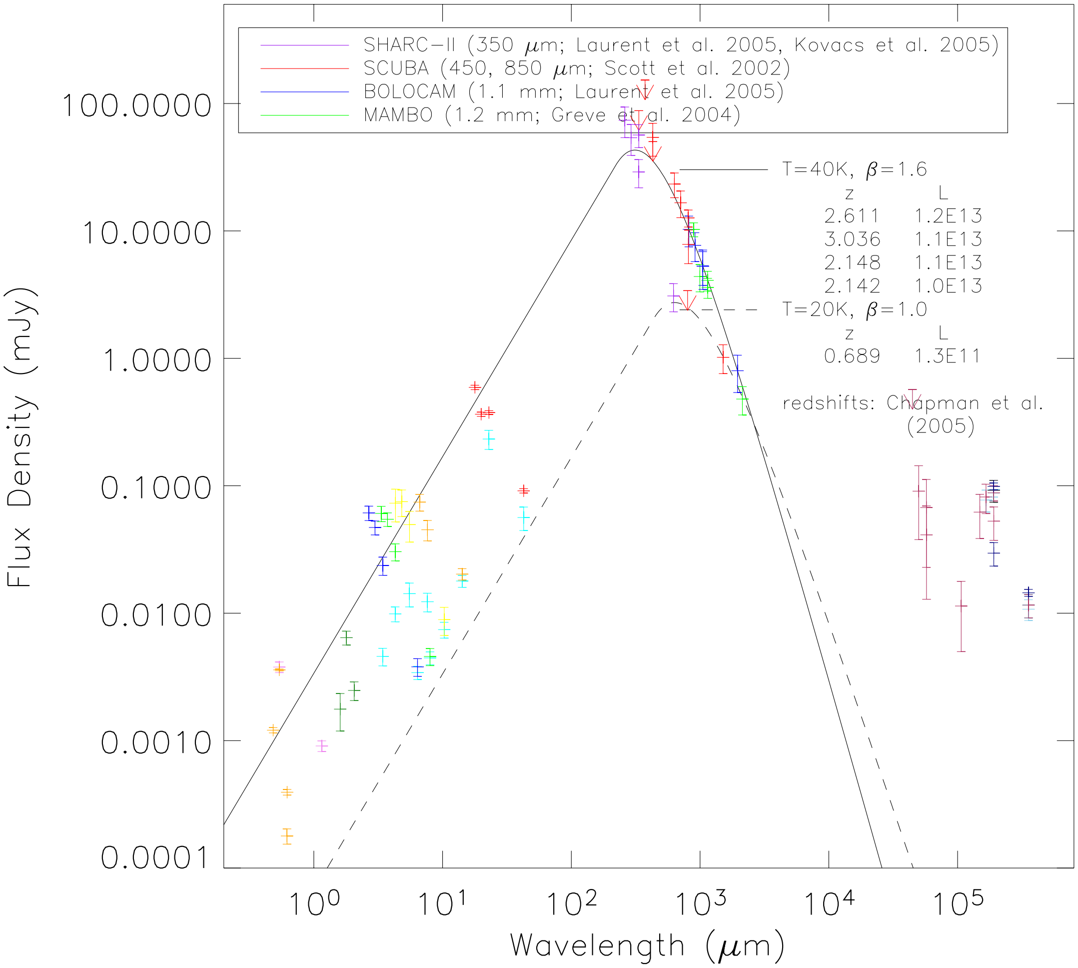

Figure 12.1 Composite SED for the five Bolocam galaxies with spectroscopic redshifts (Bolocam 5, 8, 14, 16, and 17). The observed SEDs have all been redshifted to $z = 2.0$ using the spectroscopic redshifts, corrected for cosmological dimming, and their Bolocam 1.1 mm fluxes normalized to the modified blackbody model of § 12.3. The solid line represents the modified blackbody model (T = 40 K, $\beta = 1.6$) of § 12.3, based on the composite SED of Blain et al. (2002, and references therein). The dashed line represents the same model, with T = 20 K and $\beta = 1.0$.

made about the radio continuum emission associated with these galaxies: (1) the radio continuum is lower (or the submillimeter continuum is higher) on average than the well established radio-FIR correlation for the local universe by Yun, Reddy, & Condon (2001, cf. § 11.3); and (2) like the infrared flux densities, the 6 and 20 cm VLA radio flux densities for the four galaxies with closely correlated spectra in the submillimeter region of the spectrum show a large degree of dispersion (factor of 5 in 20 cm flux density). This scatter is much larger than the quoted uncertainties of the VLA radio observations (which constrain the 20 cm radio flux density of each galaxy to better than 20%) This degree of dispersion is also larger than the factor of 3 scatter in the radio-FIR correlation seen among the FIR selected galaxies in the local universe. In fact, while the spectroscopic redshifts are similar for the four galaxies ($2.1 < z < 3.0$), varying the 20 cm flux density over the observed range causes the best fit photometric redshifts of Yun & Carilli (2002) to vary from $z = 2.7$ to 4.8. This dispersion undoubtably contributes to the large errors of the photometric redshifts discussed in § 11.

Deep radio continuum imaging using the VLA is a technically challenging task, and the disparate 20 cm flux densities by $\sim 50\%$ reported for Bolocam sources 2 and 6 (cf. § 10.3.2) exemplifies the difficulty of the photometry at radio wavelengths. Most systematic noises in interferometry tend to suppress the brightness of astronomical sources, and part of the lower radio continuum flux density might be related to the imaging and photometry problems.

It is important to note that due to the low S/N ratios at which the sources have been detected in the submillimeter wavebands ($\leq 4\sigma$ for the vast majority of SHARC, SCUBA, Bolocam, and MAMBO detections), flux bias (cf. § 5.4) plays a major role in overestimating the flux densities at these wavelengths. While this factor indeed results in a systematic shift of the entire submillimeter portion of the spectrum to higher flux densities, it is unlikely that the magnitude of this effect ($\sim 20\%$ for the Bolocam flux densities) could fully account for the lower than expected (from the FIR-radio correlation) radio continuum flux densities. Calibration errors may also contribute to a systematic overestimate of the submillimeter flux densities. Finally, as two or more independent radio sources are found within the Bolocam error circle in 8 out of 17 cases in Figure 2, source confusion or source blending may also contribute to the apparently lower radio continuum flux if only one radio source is identified as the counterpart.

The lower radio continuum flux density and the larger scatter may also reflect an actual breakdown in the radio-FIR correlation. Inverse-Compton losses for the high energy cosmic rays responsible for the synchrotron radiation is thought to be significant at $z > 2$, and a possible breakdown in the radio-FIR correlation has been considered previously (see Condon 1992, Carilli & Yun 2000). This effect is demonstrated in Figure 11.3, in which models of local ULIRGs Arp 220 and Mrk 231 systematically overestimate the radio flux densities of these submillimeter galaxies. Higher quality data on a larger sample of high redshift systems are needed to examine the importance of inverse-Compton loss and the possible breakdown in the radio-FIR correlation.

X-ray heating of the circum-nuclear gas and dust is an important source of luminosity in the far-IR if a luminous AGN is present (Maloney, Hollenbach, & Tielens 1996). Radio-quiet AGN FIR emission could reduce the 1.4 GHz flux density with respect to the FIR heating. Alexander et al. (2004, and references therein) make the case using X-ray detections and spectral indices that many, perhaps most, submillimeter galaxies have AGN but that they are not bolometrically important. However, the statistics of X-ray detected submillimeter galaxies for which hard/soft ratios can be measured is not large and it cannot be ruled out that many submillimeter galaxies are Compton thick ($\mathrm{N_H} > 1.5 \times 10^{24}\ \mathrm{cm}^{-2}$). We conclude that the generally low radio flux densities in our sample could be due to small number statistics, source confusion, or generally depressed radio emission, perhaps due to quenching of high energy cosmic rays, although radio-quiet, Compton-thick AGN contributions to the dust heating cannot be ruled out. There are new AGN versus star formation spectral diagnostics emerging (Ivison et al., Egami et al.), and it is possible that to definitively settle the issue may ultimately require ALMA, Constellation-X, and interferometric FIR spectral line diagnostic capability.

12.3 Implied Luminosities and Star Formation Rates

The flux density of a galaxy at an observed frequency, ν, is related to its intrinsic luminosity, L, by (Blain et al., 2002)

$$S_\nu = \frac{1+z}{4\pi D_L^2} L \frac{f_{\nu(1+z)}}{\int f_{\nu'}\, d\nu'}, \tag{12.1}$$

where D_L is the luminosity distance to redshift z, $f_{\nu(1+z)}$ is the redshifted SED of the galaxy, and $\int f_{\nu'}\, d\nu'$ is the integrated rest SED. For a flat ($\Omega_k = 0$) cosmology, it can be shown (e.g., Peebles, 1993) that the luminosity distance is given by

$$D_L = \frac{c\,(1+z)}{H_0} \int_0^z \frac{1}{\Omega_M (1+z')^3 + \Omega_\Lambda}\, dz'.$$

To estimate the bolometric luminosities of the submillimeter galaxies detected by Bolocam, a template SED was constructed that assumes a blackbody emission spectrum modified by a dust emissivity term:

$$f_\nu \propto \epsilon_\nu B_\nu(T) \propto [1 - \exp(-\tau_\nu)] B_\nu(T), \tag{12.2}$$

where $B_\nu(T)$ is the Planck function evaluated at dust temperature, T, and frequency, ν, and τ_ν is the optical depth of the dust:

$$\tau_\nu = \left(\frac{\nu}{\nu_0}\right)^\beta .$$

The dust emissivity index, β, is believed to lie between 1 and 2 (Dunne et al., 2000). The form of equation (12.2) is commonly assumed in the literature for dusty nearby galaxies and high-redshift AGNs, including Benford et al. (1999), Omont et al. (2001), Priddey & McMahon (2001), and Isaac et al. (2002). This equation reduces to a simple optically thin emission spectrum, $\epsilon_\nu B_\nu(T) \sim \nu^{2+\beta}$, in the Rayleigh-Jeans limit and $\nu \ll \nu_0$, and it asymptotes to $B_\nu(T)$ at high frequencies (because an emissivity of > 1

is unphysical). Observations of luminous low-redshift galaxies (Arp 220 and Mrk 231) and high-redshift galaxies detected by deep submillimeter surveys furthermore suggest that a power law, $f_\nu \propto \nu^\alpha$, is appropriate to model the hotter components of dust on the Wien side of the spectrum (Blain et al., 1999). We implement such a power law at high frequencies, matched to equation (12.2) at $1.2\nu_0$. Creating a composite SED of nearby dusty *IRAS* galaxies, high-redshift submillimeter galaxies, gravitationally lensed high-redshift galaxies, and high-redshift AGNs (Blain et al., 2002, and references therein), we find that parameters of T = 40 K, ν_0 = 3700 GHz, β = 1.6, and α = -1.7 provide a reasonable fit.

To obtain the intrinsic bolometric luminosities of the five Bolocam galaxies with spectroscopic redshifts, the spectra of § 10.3.4 (based on the above modified blackbody model) were integrated for each galaxy in their respective rest frames. The resulting bolometric luminosities are listed in Figure 10.4. The four galaxies well-modeled by a 40 K dust spectrum have extreme bolometric luminosities ranging from $L = (1.0 - 1.2) \times 10^{13}$ $\mathrm{L}_\odot$. The lower redshift galaxy (Bolocam source 17) has an inferred luminosity two orders of magnitude lower ($L = 1.3 \times 10^{11}$ $\mathrm{L}_\odot$). If the spectroscopic redshift of 0.689 does not apply to this galaxy and it instead lies at z = 3.4 (the photometric redshift predicted by the Laurent et al. 2005 / Wiklind 2003 and *Spitzer* IR models), then its luminosity of $L = 8.2 \times 10^{12}$ $\mathrm{L}_\odot$ agrees well with the others. Note that if these galaxies are lensed, their intrinsic luminosities will be lower.

Observations of nearby star-forming galaxies suggest the following relation between the SFR present in a galaxy and its far-infrared luminosity:

$$\mathrm{SFR} = \epsilon \times 10^{-10} \frac{L_{60\mu\mathrm{m}}}{\mathrm{L}_\odot} \mathrm{M}_\odot \mathrm{yr}^{-1},$$

where $L_{60\mu\mathrm{m}}$ is the 60 μm luminosity. The value of ϵ varies in the literature from 2.1 to 6.5 (Scoville & Young, 1983; Thronson & Telesco, 1986; Rowan-Robinson et al., 1997) because of different assumptions about the duration of the starburst, different initial mass functions (IMFs), and lower mass limits. In this paper we adopt a value of $\epsilon = 2.1$ from a "cirrus" model that combines very small grains and polycyclic aromatic hydrocarbons (PAHs) with a Salpeter IMF in a starburst of OBA stars over 2×10^6 yr (Thronson & Telesco, 1986). Obtaining $L_{60\mu\mathrm{m}}$ from our model SED yields large SFRs of $480 - 810$ $\mathrm{M}_\odot \mathrm{yr}^{-1}$. While these calculated luminosities and SFRs are sensitive to the SED model parameters, particularly T and β, most recent models of local star-forming galaxies nevertheless result in dust temperatures and emissivities that imply extreme luminosities and SFRs. It is possible, however, that these extremely luminous galaxies derive some of their power from AGNs (e.g., Alexander et al., 2003), in which case the SFRs have been overestimated. Observations of ultraluminous infrared galaxies (ULIRGs) in the local universe ($z \lesssim 0.1$) with luminosities $> 10^{13}$ $\mathrm{L}_\odot$ show that nearly all of these galaxies possess luminous AGNs and that the dominant power source in the majority of nearby ULIRGs may be AGNs rather than star formation (Sanders 1999). Recent X-ray observations and optical spectroscopic data of $z > 1$ ultraluminous galaxies, however, indicate that in almost all cases the AGNs account for $< 20\%$ of the total bolometric output of higher-redshift galaxies (Alexander et al., 2004). *Spitzer* observations will prove useful in investigating the incidence of AGNs versus star formation in submillimeter galaxies from the shape of the mid-infrared continuum emission; initial results confirm the high-redshift X-ray results and show a mixture of infrared-warm AGNs and cooler starburst-dominated sources (Egami et al., 2004; Frayer et al., 2004), with a smaller fraction (~25%) of energetically important AGNs (Ivison et al., 2004).

12.4 Stellar and Dust Masses Implied from the Integrated Submillimeter Luminosities

Three hundred and fifty micron observations combined with far-infrared and millimeter-wavelength photometry enables accurate measurements of luminosity for galaxies near $z = 2$ because no interpolation across the peak of the SED is required.

Characteristically, integration of the SEDs of the galaxies in our sample from far-infrared to millimeter-wavelengths yields luminosities of $\sim 1 \times 10^{13}$ $L_{\odot}$. Assuming: 1) that the luminosity derives from star formation (young stars, which may overestimate stellar masses due to contribution from intermediate mass giants), 2) a characteristic (Salpeter) form of the initial mass function (IMF) from Chabrier (2003), and 3) all of the optical and ultraviolet radiation is reprocessed to long wavelengths by dust, enables the stellar mass content of the galaxies to be approximately estimated. We adopt the $M^{3.5}$ luminosity function of Demircan & Kahraman (1991). Because the luminosity function is so steep, the derived mass depends strongly on the assumed upper mass limit of integration. The lower limit of integration is not well constrained by the data, although masses less than 0.3 $M_{\odot}$ are not likely to dominate the mass because the IMF flattens considerably at low mass. Lower mass limits of 0.7 and 1.0 $M_{\odot}$ could be relevant because: 1) Dwek et al. (1998) argued that a Salpeter IMF for $z > 1$ galaxies cannot extend much lower than this without producing too many low mass stars that would be present today and 2) Chabrier (2003) suggests (with caution) that the high-z IMF could cut off > 1 $M_{\odot}$ based on multiple circumstantial lines of evidence. Varying m_l from 0.3 to 1.0 $M_{\odot}$ and limiting m_u to ≤ 50 $M_{\odot}$ yields a mininum stellar mass of 10^{10} $M_{\odot}$ and a maximum of a few $\times$ 10^{11} $M_{\odot}$, consistent with the stellar mass content of large elliptical galaxies, as previously pointed out by many authors (e.g., Smail et al., 2002; Lilly et al., 1999). This range must be considered an upper limit because AGN could be responsible for some of the dust heating.

For all of the galaxies with secure 350 μm detections, especially those with Chapman et al. (2005) spectroscopic redshifts, it is clear that the Bolocam 1.1 mm observations lie on the optically thin Rayleigh-Jeans side of the SED, and therefore enable dust mass estimates. The flux density, S_{ν}, of a galaxy at an observed frequency, ν, is related to the dust mass, M, by

$$S_\nu = B_{\nu'}(T)\frac{\kappa_\nu M(1+z)}{D_L^2},$$

where D_L is the luminosity distance to redshift z, $B_{\nu'}(T)$ is the Plank function evaluated at the emitted frequency, ν', and κ_ν is the dust opacity. Using the range of observed Bolocam flux densities (4.0 - 6.8 mJy), assuming a redshift of 2.1, and applying the dust cross section of $\kappa_\nu = 12.4$ cm^2/g (Ossenkopf & Henning, 1994) most relevant for high mass star formation (high gas density and thin ice mantle model), leads to dust masses of 3 - 5 $\times$ 10^8 M$_\odot$ (2 - 3 $\times$ 10^8 M$_\odot$) for a dust temperature of 40 K (50 K). Blindly applying a dust-to-gas mass ratio of 1/100 implies gas masses of 3 - 5 $\times$ 10^{10} M$_\odot$. These gas masses are comparable to those from a recent sample of 8 submillimeter galaxies of Genzel et al. (2004) and Neri et al. (2003) which yield median molecular gas masses (from CO emission) of 2.2 $\times$ 10^{10} M$_\odot$ and 2.8 $\times$ 10^{10} M$_\odot$, with median dynamical masses of 1.1 $\times$ 10^{11} M$_\odot$ and 6.2 $\times$ 10^{10} M$_\odot$ (assuming the most probable inclination angle of sin $i = 2/\pi$), respectively. These gas mass estimates are uncertain to at least a factor of a few due to 1) the Bolocam flux density bias, which causes the measured flux densities to be overestimated by 10 - 30%, 2) our assumed values of κ and T, which may vary by a factor of a few and ± 20 K, respectively, and 3) increasing our assumed redshift of 2.1 (the mean of the 5 Chapman spectroscopic redshifts of the Bolocam galaxies) to $z = 2.4$ *increases* our calculated gas mass by 30%. Nevertheless, taking these factor into account still imply that a considerable fraction of the mass could already by in stars and substantial gas remains for star formation. This major epoch of galaxy formation at approximately $z = 2$ is consistent with the conclusions of Fontana et al. (2004) from spectral fitting of a sample of 500 elliptical galaxies at $0.2 \leq z \leq 2.5$ that approximately 35% of elliptical galaxy stellar mass was assembled by $z = 2$ and approximately 80% by $z = 1$.

Chapter 13

Future Work

We have shown that observations at shorter submillimeter wavelengths are vital to both confirm the Bolocam galaxy candidate detections and make photometric redshift and temperature estimates. Follow-up 350 μm photometry of the Bolocam-detected submillimeter galaxies with SHARC II has helped fill in the SEDs of these galaxies and has provided more precise astrometry (due to the $10''$ beam size of SHARC II) of the submillimeter sources. Similarly, *Spitzer* far-infrared observations combined with the Bolocam 1.1 mm galaxy survey will provide a flux density ratio that is strongly dependent on redshift for a given temperature. This is because the rest wavelengths corresponding to the observed *Spitzer* MIPS wavelengths of 70 and 160 μm are on the rapidly falling Wien side of the greybody spectrum (for a $z \sim 2$ galaxy at 40 K), and Bolocam's 1.1 mm observations are on the steep $\nu^{2+\beta}$ ($\beta \approx$1.5) modified Rayleigh-Jeans side of the SED. The ratio of $S_{1.1\mathrm{mm}}/S_{70\mu\mathrm{m}}$ is thus highly dependent on redshift, growing by a factor of 250 from $z = 1$ to 5 (cf. Figure 11.5). Combined with the existing near- and mid-IR *Spitzer* IRAC observations, the 70 μm MIPS photometry will strengthen the photometric redshift determinations discussed in § 11.

As discussed in § 9.1, this survey does not constrain the number counts at flux densities above 7 mJy, at approximately the break point where the number counts are expected to drop sharply (based on the 850 μm observations in Fig. 9.1). This can be addressed with a survey covering a larger area to shallower depth. Such a survey has recently been completed in February 2004 and February - April 2005 with Bolocam in the COSMOS field,[1] which uniformly covers ~ 1000 arcmin^2 down to an RMS of 1.9 mJy beam^{-1} after optimal (Wiener) filtering for point sources (Aguirre et al., 2006). The COSMOS field (2 square degrees in total) was picked by a large collaboration in order to obtain deep, multi-wavelength coverage to study the evolution of large scale structure out to $z \sim 3$. The field will be covered by HST I-band, Subaru deep imaging, VLA 20 cm, VLT-VIMOS spectroscopy, Spitzer IRAC and MIPS, and submillimeter surveys by Bolocam, MAMBO (0.25 square degrees to 0.9 mJy beam^{-1} RMS at 1.2 mm) and AzTEC (1.1 mm). The MAMBO coverage is roughly half-completed, surveying approximately 0.13 square degrees to between 0.9 and 2.0 mJy beam^{-1}. Using a more finely sampled, highly cross-linked scan strategy than that used for the Lockman Hole field, the Bolocam observations covered the central 1000 arcmin^2 of the COSMOS field to a very uniform depth, with rms coverage variations of only 1.6%. This uniform coverage aids in rejecting atmospheric $1/f$ noise, better constrains the bright end of the submillimeter galaxy distribution, and provides an even more uniformly sampled map for $P(D)$ analysis.

Preliminary analysis that mirrors the extensive jackknife simulations of the Lockman Hole analysis in estimating the false detection rate, flux bias, and completeness reveals 9 detections at $\geq 3.8\sigma$ (the detection threshold where only one false detection is expected). The mean flux density of these sources, corrected for flux bias, is 6.1 mJy, with the brightest having a flux density of 8.1 mJy. An initial comparison with the MAMBO survey yields only one Bolocam 3.8σ detection within the MAMBO uniform coverage region, with MAMBO positively detecting the source. A preliminary $P(D)$ analysis on the COSMOS field finds general agreement with the Lockman Hole data, with tentative evidence for the slightly higher values of n_0 and δ as reported by the MAMBO Lockman Hole survey Greve et al. (2004). When complete, this survey will

---

[1] See http://www.astro.caltech.edu/cosmos.

allow either the determination or a strong upper limit on the 1.1 mm number counts well beyond 7 mJy, as well as uncover extremely bright, interesting sources, perhaps with strong AGN components that should be easy to follow up at other wavelengths.

Comparison of the COSMOS sources with VLA 1.4 GHz data to find radio counterparts is currently underway. With these sources, we will identify counterparts in optical surveys with HST, Spitzer and Subaru. SHARC II follow-up time has been awarded for Spring 2006 to help constrain the SEDs near the submillimeter dust peak. Future work also includes pointed 6 cm VLA continuum observations, and proposed submillimeter spectroscopic redshifts with Z-Spec and the GBT. With these data we can put further constraints on the shape of the dust peak in submillimeter galaxies and test photometric redshift techniques for galaxies with well-sampled SEDs. This will help place submillimeter galaxies into the framework of galaxy evolution and determine their connection to large scale structure formation.

Several instruments will soon come online that address several of the limitations of Bolocam and other current submillimeter surveys and will contribute substantially to the field of submillimeter astronomy over the next decade. The large beam sizes of current submillimeter instruments limit the astrometry of submillimeter galaxies as well as contribute to source confusion. The multi-dish submillimeter interferometers of the SMA (Sub-Millimeter Array, Ho, 2000) and ALMA (Atacama Large Millimeter Array, Wootten, 2001) promise sub-arcsecond resolution and have the bandwidth to make rapid searches for CO lime emission of known submillimeter continuum sources. High altitude balloon-based observations with BLAST (Devlin et al., 2001), along with the SPIRE receiver on the *Herschel* satellite (Griffin, Swinyard & Vigroux, 2001), will be largely immune to the sky emission that dominates source signal by three or more orders of magnitude, allowing for surveys of tens of square degrees, with projected detection rates of thousands of submillimeter galaxies. Combined with 1.1 mm Bolocam observations, the BLAST and *Herschel* space telescope 250 μm bands are also extremely strong functions of redshift, which will allow for more precise photometric redshift determinations. Finally, definitive spectroscopic redshifts of these galaxies will be obtained directly from the submillimeter waveband with Z-Spec (Naylor et al., 2002), a broadband millimeter-wave grating spectrometer. Submillimeter spectroscopy eliminates the necessity of radio and / or optical counterparts for redshifts, which bias spectroscopic samples against both cooler galaxies (especially at high redshift) as well as sources in the "spectroscopic desert" ($1 < z < 2$, in which no strong ultraviolet lines are redshifted into the optical portion of the spectrum). These advancements in submillimeter technology will bring us substantially closer to the goals of this research, namely the determination of galaxy redshifts and clustering, constraints on the luminosity and mass functions of submillimeter galaxies, and the resolution of structure formation models.

Chapter 14

Conclusions

Bolocam is a new bolometer camera with a large field of view and a rapid mapping speed optimized for surveys, including surveys for rare, bright submillimeter galaxies. We have used Bolocam on the Caltech Submillimeter Observatory at a wavelength of 1.1 mm to conduct a survey of 324 arcmin^2 toward the Lockman Hole for submillimeter galaxies. Unlike previous submillimeter surveys, the observations were made without chopping, at a fast scan rate of $60''$ s^{-1}. The Bolocam survey encompasses the entire 850 μm 8 mJy JCMT SCUBA and 1.2 mm IRAM MAMBO surveys to a comparable depth under the assumption of a model SED for a galaxy at $z = 2.4$, with relative rms of $1 : 0.9 : 0.6{-}1.4$, respectively. We have reduced the resulting data set using a custom IDL-based software pipeline, in which correlated atmospheric and instrument noise is rigorously removed via a PCA sky subtraction technique. We detect 17 galaxies at a significance of $\geq 3\ \sigma$, where the map rms is $\sim$1.4 mJy.

A series of simulations have allowed us to verify the robustness of the galaxy candidates. Extensive jackknife and pointing jitter tests reveal that the sources detected in this survey have a small characteristic length scale (point sources) and are contributed to by the ensemble of observations, strongly indicating that the galaxy candidates are real. Simulations of the observations using both synthetic maps and observational data indicate that six false detections should be expected.

Comparing our detections to those of other surveys (including SCUBA 850 μm, MAMBO 1.2 mm, and VLA radio observations) indicates that the majority of Bolocam sources have coincident detections in at least two other wavebands; we conclude that a majority of the Bolocam detections are real. Six of the detections are galaxies previously detected by the SCUBA 8 mJy survey. Of the remaining 11 Bolocam detections, 9 of them lie outside the SCUBA survey region, and we cannot search for counterparts for them. Seven of the 17 Bolocam detections have been detected by the MAMBO 1.2 mm survey, with 6 of the remaining 10 sources lying outside the MAMBO good coverage region. While both the SCUBA and MAMBO surveys detect most of the Bolocam sources in the overlap region, neither Bolocam nor SCUBA/MAMBO detect the majority of the remaining SCUBA and MAMBO sources. A total of 88% of the 17 Bolocam source candidates have at least one radio coincidence, although the accidental radio detection rate is high ($\geq 20\%$) owing to the size ($31''$ FWHM) of the Bolocam beam. Furthermore, we statistically detect the aggregate average of the SCUBA and MAMBO sources below our 3 σ detection threshold at significances of 3.3 and 4.0 σ, respectively.

Further simulations enabled us to estimate the completeness and bias of this survey, which were subsequently used with the false detection rate to fit a simple power-law model of the underlying parent distribution to match the observed number count distribution. This model constrains the submillimeter counts over the flux density range $S_{1.1\mathrm{mm}} = 1{-}7$ mJy. While the validity of this model is significantly limited by both the effects of confusion noise and the flux density cutoffs assumed for the underlying number count distribution, we find this modeled number count distribution to be consistent with previously published submillimeter galaxy number counts. Integrating the maximum likelihood differential number counts distribution between 1 and 6.8 mJy (the maximum observed flux density) yields 276 mJy in the map, or $\sim$13% of the FIRAS integrated far-infrared background light (with the majority of the FIRAS background likely lying below the minimum fluxes derived from our number counts models).

We have also obtained 350 μm SHARC II observations toward galaxy candidates from the Bolocam Lockman Hole survey. The Lockman Hole has rich, deep, multiwavelength observations enabling detailed studies of galaxies. The 350 μm photometry is near the peaks of the SEDs of galaxies with characteristic temperatures of $\sim$ 50 K and redshifts of $z \sim 2$ to 3. They therefore enable measurements of luminosities and estimates of temperatures and photometric redshifts without interpolating over the peak of the FIR thermal SEDs. Seven galaxies detected at 1.1 mm with Bolocam were detected at 350 μm, two of which have two 350 μm counterparts; these were combined with two 350 μm detections from the survey of Kovács et al. (2005), bringing the total number of Bolocam galaxies detected with SHARC II to nine. Two additional galaxies not associated with the Bolocam sources were also detected. The SHARC II detections range in significance from 3.0 σ to 6.8 σ, with flux densities ranging from 14 mJy to 64 mJy.

We combined our observations with 850 μm and 1.2 mm photometry from the literature to fit the submillimeter/millimeter-wave spectra to thermal dust models. We found that two models with significantly different dust temperatures (40 K and 68 K) and spectral indices β (1.6 and 1.8, respectively) yielded similar quality fits owing to the degeneracy in T and β, rendering them indistinguishable without better SED sampling. However, there is little consequence of the degeneracy to the derived luminosities, photometric redshifts, and dust masses within the statistical uncertainties. Five of the galaxies have spectroscopic redshifts in the literature, with four ranging from $z = 2.1$ to 3.0 and one at $z = 0.689$. The four high-z galaxies have luminosities of (1.0 - 1.2) $\times$ 10^{13} $L_\odot$, while the $z = 0.689$ galaxy is best fit by a 20 K, $\beta = 1.0$, spectrum with a much lower luminosity: 1.3 $\times$ 10^{11} $L_\odot$. (Given the source confusion in the optical and radio, along with consistent photometric redshifts, we suggest that the $z = 0.689$ spectroscopic redshift of Bolocam source 17 may be a misidentification.) Assuming that they are powered by star formation, large SFRs of $480 - 810$ $M_\odot yr^{-1}$ are implied. The characteristic dust masses for the four high-z spectroscopic galaxies are 4 $\times$ 10^8 $M_\odot$, implying gas masses of 4 × 10^{10} $M_\odot$. The dominant uncertainties in this estimation are the dust opacity and the gas-to-dust conversion factor, which make the estimation uncertain to a factor of a few. Assuming a Salpeter IMF and that the submillimeter emission derives completely from star formation yields stellar masses of 10^{10} to a few times 10^{11} $M_\odot$, broadly consistent with the stellar content of modern-day elliptical galaxies.

The photometric redshifts of the full sample of seven galaxies span the range of $z = 2.0$ to $z = 4.3$, with statistical uncertainties of $\Delta z = 0.3$ to 0.6 (1 σ). Photometric redshifts utilizing composite radio/FIR spectra representative of local star-forming ULIRGs yields systematically higher redshifts, on the order of $\Delta z = 1$. For the four galaxies with optical spectroscopic redshifts the anomalously high redshifts arise from systematically low 1.4 GHz observed flux densities. The discrepancy could arise from small number statistics, inverse-Compton losses of high energy cosmic rays off the CMB, heating by radio-quiet AGN, or suppressed synchrotron emission from supernova remnants in the unusually luminous galaxies. For comparison, photometric redshifts derived using only Spitzer MIPS and IRAC data points yielded slightly more precise and accurate redshifts than the submillimeter/millimeter-wave data alone, with discriminatory power between heating by AGN and star formation (albeit with limited bolometric luminosity constraints).

This thesis utilized the Bolocam instrument at 1.1 mm to better characterize the origin and nature of submillimeter galaxies. The Bolocam instrument and atmospheric noise subtraction techniques offer the mapping of large fields to a uniform depth for the detection of the brightest submillimeter galaxies. Through the detection of these galaxies at 1.1 mm, determination of their number count distribution, and follow-up observations at 350 μm, we support the proposition that these dusty galaxies lie at high redshift, are likely powered primarily through star formation, and form a group of galaxies that are characteristically distinct (in number counts and / or luminosities) from sources selected at other wavelengths and epochs of formation, namely LBGs, EROs, and ULIRGs. When combined with future surveys with Bolocam and other instruments, this research will help better understand the role of submillimeter galaxies in galaxy formation and evolution, and the growth of large scale structure.

Bibliography

Aguirre, J., et al. 2006, ApJ, in prep.

Alexander, D. M., Bauer, F. E., Brandt, W. N., Hornschemeier, A. E., Vignali, C., Garmire, G. P., Schneider, D. P., Chartas, G., & Gallagher, S. C. 2003, AJ, 125, 383

Alexander, D. M., Bauer, F. E., Chapman, S. C., Smail, I., Blain, A. W., Brandt, W. N., & Ivison, R. J. 2004, preprint (astro-ph/0401129)

Almaini, O., Scott, S. E., Dunlop, J. S., Manners, J. C., Willott, C. J., Lawrence, A., Ivison, R. J., Johnson, O., Blain, A. W., Peacock, J. A., Oliver, S. J., Fox, M. J., Mann, R. G., Perez-Fournon, I., Gonzalez-Solares, E., Rowan-Robinson, M., Serjeant, S., Cabrera-Guerra, F., & Hughes, D. H. 2003, MNRAS, 338, 303

Aretxaga, I., Hughes, D. H., Chapin, E. L., Gaztanaga, E., Dunlop, J. S., & Ivison, R. J. 2003, MNRAS, 342, 759

Barger, A. J., Cowie, L. L., & Sanders, D. B. 1999, ApJ, 518, L5

Barmby, P., Huang, J.-S., Fazio, G. G., Surace, J. A., Arendt, R. G., Hora, J. L., Pahre, M. A., Adelberger, K. L., Eisenhardt, P., Erb, D. K., Pettini, M., Reach, W. T., Reddy, N. A., Shapley, A. E., Steidel, C. C., Stern, D., Wang, Z., & Willner, S. P. 2004, ApJS, 154, 97

Benford, D. J., Cox, P., Omont, A., Phillips, T. G., & McMahon, R. G. 1999, ApJ, 518, L65

Bertoldi, F., Carilli, C. L., Menten, K. M., Owen, F., Dey, A., Gueth, F., Graham, J. R., Kreysa, E., Ledlow, M., Liu M. C., Motte, F., Reichertz, L., Schilke, P., & Zylka, R. 2000, A&A, 360, 92

Biggs, A. D., Ivison, R. J. 2006, in prep

Blain, A. W., Chapman, S. C., Smail, I., & Ivison, R. 2004, ApJ, 611, 725

Blain, A. W., Kneib, J.-P., Ivison, R. J., & Smail, I. 1999, ApJ, 512, L87

Blain, A., Smail, I., Ivison, R. J., Kneib, J.-P., & Frayer, D. T. 2002, Phys. Rept.369, 111

Bond, J. R., Contaldi, C. R., Pen, U.-L., Pogosyan, D., Prunet, S., Ruetalo, M. I., Wadsley, J. W., Zhang, P., Mason, B. S., Myers, S. T., Pearson, T. J., Readhead, A. C. S., Sievers, J. L., & Udomprasert, P.S. 2005, ApJ, 626, 12

Borys, C., Chapman, S., Halpern, M., & Scott, D. 2003, MNRAS, 344, 385

Brinchmann, J., & Ellis, R. S. 2000, ApJ, 536, L77

Carilli, C. L., & Yun, M. S. 1999, ApJ, 513, L13

Chabrier, G. 2003, PASP, 115, 763

Chapman, S. C., Blain, A., Ivison, R., & Smail, I. 2003a, in ASP Conf. Ser. 297, Star Formation through Time, ed. E. Perez, R. M. Gonzales Delgado, & G. Tenorio-Tagle (San Francisco: ASP), 289

Chapman, S. C., Blain, A. W., Ivison, R. J., & Smail, I. R. 2003b, Nature, 422, 695

Chapman, S. C., Windhorst, R., Odewahn, S., Yan, H., & Conselice, C. 2003c, 599, 92

Chapman, S. C., Blain, A. W., Smail, I., & Ivison, R. J. 2005, ApJ, 622, 772

Chapman, S. C., Scott, D., Borys, C., & Fahlman, G. G. 2002, MNRAS, 330, 92

Ciliegi, P., Zamorani, G., Hasinger, G., Lehmann, I., Szokoly, G., & Wilson, G. 2003, A&A, 398, 901

Condon, J. J. 1974, ApJ, 188, 729

Cowie, L. L., Barger, A. J., & Kneib, J.-P. 2002, AJ, 123, 2197

Crawford, D. F., Jauncey, D. L., & Murdoch, H. S. 1970, ApJ, 162, 405

Daddi, E., Cimatti, A., Pozzetti, L., Hoekstra, H., Rottgering, H. J. A., Renzini, A., Zamorani, G., & Mannucci, F. 2000 A&A, 361, 535

Dale, D., & Helou, G. 2002, ApJ, 576, 159

Devlin, M., et al. 2001, in Lowenthal, J., Hughes, D. H., eds, Deep Millimetre Surveys: Implications for Galaxy Formation and Evolution. World Scientific, p. 59

Demircan, O., & Kahraman, G. 1991, Ap&SS, 181, 313

Dunne, L., Eales, S., Edmunds, M., Ivison, R, Alexander, P., & Clements, D. L. 2000, MNRAS, 315, 115

Dwek, E., Arendt, R. G., Hauser, M. G., Fixen, D., Kelsall, T., Leisawitz, D., Pei, Y. C., Wright, E. L., Mather, J. C., Moseley, S. H., Odegard, N., Shafer, R., Silverberg, R. F., Weiland, J. L. 1998, ApJ, 508, 106

Eales, S., Bertoldi, F., Ivison, R., Carilli, C., Dunne, L., & Owen, F. 2003, MNRAS, 344, 169

Eddington, A. S. 1913, MNRAS, 73, 359

Eddington, A. S. 1940, MNRAS, 100, 354

Efstathiou, A., Rowan-Robinson, M., & Siebenmorgen, R. 2000, MNRAS, 313, 734

Egami, E., Dole, H., Huang, J.-S., Perez-Gonzalez, P., Floc'h, E. Le, Papovich, C., Barmby, P., Ivison, R. J., Serjeant, S., Mortier, A., Frayer, D. T., Rigopoulou, D., Lagache, G., Rieke, G. H., Willner, S. P., Alonso-Herrero, A., Bai L., Engelbracht, C. W., Fazio, G. G., Gordon, K. D., Hines, D. C., Misselt, K. A., Miyazaki, S., Morrison, J. E., Rieke, M. J., Rigby, J. R., & Wilson, G. 2004, ApJ, 154, 130

Feldman, G. J., & Cousins, R. D. 1998, Phys. Rev. D, 57, 3873

Fixsen, D. J., Dwek, E., Mather, J. C., Bennett, C. L., & Shafer, R. A. 1998, ApJ, 508, 123

Fontana, A., Pozzetti, L., Donnarumma, I., Renzini, A., Cimatti, A., Zamorani, G., Menci, N., Daddi, E., Giallongo, E., Mignoli, M., Perna, C., Salimbeni, S., Saracco, P., Broadhurst, T., Cristiani, S., D'Odorico, S., & Gilmozzi, R. 2004, A&A, 424, 23

Fox, M. J., Efstathiou, A., Rowan-Robinson, M., Dunlop, J. S., Scott, S., Serjeant, S., Mann, R. G., Oliver, S., Ivison, R. J., Blain, A., Almaini, O., Hughes, D., Wilcott, C. J., Longair, M., Lawrence, A., & Peacock, J. A. 2002, MNRAS, 331, 839

Frayer, D. T., Chapman, S. C., Yan, L., Armus, L., Helou, G., Fadda, D., Morganti, R., Garrett, M. A., Appleton, P., Choi, P., Fang, F., Heinrichsen, I., Im, M., Lacy, M., Marleau, F., Amsci, F. J., Shupe, D. L., Soifer, B. T., Squires, G. K., Storrie-Lombardi, L. J., Surace, J. A., Teplitz, H. I., & Wilson, G. 2004, ApJS, 154, 137

Frayer, D. T., Ivison, R. J., Scoville, N. Z., Evans, A. S., Yun, M. S., Smail, I., Barger, A. J., Blain, A. W., & Kneib, J.-P. 1999, ApJ, 514, L13

Frayer, D. T., Ivison, R. J., Scoville, N. Z., Yun, M., Evans, A. S., Smail, I., Blain, A. W., & Kneib, J.-P. 1998, ApJ, 506, L7

Genzel, R., Baker, A. J., Ivison, R. J., Bertoldi, F., Blain, A. W., Chapman, S. C., Cox, P., Davies, R. I., Eisenhauer, F., Frayer, D. T., Greve, T., Lehnert, M. D., Lutz, D., Nesvadba, N., Neri, R., Omont, A., Seitz, S., Smail, I., Tacconi, L. J., Tecza, M., Thatte, N. A., & Bender, R. 2004, preprint (astro-ph/0403183)

Genzel, R., Lutz, D., Moorwood, A. F. M., Rigopoulou, D., Spoon, H. W. W., Sternberg, A., Sturm, E., & Tran, D. 2000, LNP, 548, 199

Glenn, J., Ade, P. A. R., Amarie, M., Bock, J. J., Edgington, S. F., Goldin, A., Golwala, S., Haig, D., Lange, A. E., Laurent, G., Mauskopf, P. D., Yun, M., & Nguyen, H. 2003, in *Proc. of the SPIE*, Millimeter and Submillimeter Detectors for Astronomy, eds. T.G. Phillips & J. Zmuidzinas, 4855, 30

Glenn, J., Bock, J. J., Chattopadhyay, G., Edgington, S. F., Lange, A. E., Zmuidzinas, J., Mauskopf, P. D., Rownd, B., Yuen, L., & Ade, P. A. R. 1998, in *Proc. of the SPIE*, Advanced Technology MMW, Radio, and Terahertz Telescopes, ed. T.G. Phillips, 3357, 326

Glenn, J., Chattopadhyay, G., Edgington, S. F., Lange, A. E., Bock, J. J., Mauskopf, P. D., & Lee, A. T. 2002, *Appl. Opt.*, 41, 136

Greve, T. R., Bertoldi, F., Smail, I., Neri, R., Chapman, S. C., Blain, A. W., Ivison, R. J., Genzel, R., Omont, A., Cox, P., Tacconi, L., & Kneib, J.-P. 2005, MNRAS, 359, 1165

Greve, T. R., Ivison, R. J., Bertoldi, F., Stevens, J. A., Dunlop, J. S., Lutz, D., & Carilli, C. L. 2004, MNRAS, 354, 779

Griffin, M. J., Swinyard, B. M., & Vigroux, L. 2001, phso conf, 37

Haig, D. J., Ade, P. A. R., Aguirre, J. E., Bock, J. J., Enoch, M. L., Glenn, J., Goldin, A., Golwala, S., Laurent, G. T., Maloney, P. R., Mauskopf, P. D., Rossinot, P., Sayers, J., & Stover, P. 2004, Proc. SPIE, 5498, 78

Hasinger, G., Altieri, B., Arnaud, M., Barcons, X., Bergeron, J., Brunner, H., Dadina, M., Dennerl, K., Ferrando, P., Finoguenov, A., Griffiths, R. E., Hashimoto, Y., Jansen, F. A., Lumb, D. H., Mason, F. O., Mateos, S., McMahon, R. G., Miyaji, T., Paerels, F., Page, M. J., Ptak, A. F., Sasseen, T. P., Schartel, N., Szokoly, G. P., Trumper, J., Turner, M., Warwick, R. S., & Watson, M. G. 2001, A&A, 365, L45

Hauser, M. G., Arendt, R. G., Kelsall, T., Dwek, E., Odegard, N., Weiland, J. L., Freudenreich, H. T., Reach, W. T., Silverberg, R. F., Moseley, S. H., Pei, Y. C., Lubin, P., Mather, J. C., Shafer, R. A., Smoot, G. F., Weiss, R., Wilkinson, D. T., & Wright, E. L. 1998, ApJ, 508, 25

Ho, P. T. P. 2000, in *ASP Conf. Series*, Imaging at Radio through Submillimeter Wavelengths, ed. J. Mangum, 217, 25

Holland, W. S., Robson, E. I., Gear, W. K., Cunningham, C. R., Lightfoot, J. F., Jenness, T., Ivison, R. J., Stevens, J. A., Ade, P. A. R., Griffin, M. J., Duncan, W. D., Murphy, J. A., & Naylor, D. A. 1999, MNRAS, 303, 659

Isaak, K. G., Priddey, R. S., McMahon, R. G., Omont, A., Peroux, C., Sharp, R. G., & Withington, S. 2002, MNRAS, 329, 149

Ivison, R. J., Greve, T. R., Serjeant, S., Bertoldi, F., Egami, E., Mortier, A. M. J., Alonzo-Herrero, A., Barmby, P., Bei, L., Dole, H., Engelbracht, C. W., Fazio, G. G., Frayer, D. T., Gordon, K. D., Hines, D. C., Huang, J.-S., Le Floc'h, E., Misselt, K. A., Miyazaki, S., Morrison, J. E., Papovich, C., Perez-Gonzalez, P. G., Rieke, M. R., Rieke, G. H., Rigby, J., Rigopoulou D., Smail, I., Wilson, G., & Willner, S. P. 2004, ApJS, 154, 124

Ivison, R. J., Greve, T. R., Smail, I., Dunlop, J. S., Roche, N. D., Scott, S. E., Page, M. J., Stevens, J. A., Almaini, O., Blain, A. W., Wilcott, C. J., Fox, M. J., Gilbank, D. G., Serjeant, S., & Hughes, D. H. 2002, MNRAS, 337, 1

Ivison, R. J., et al., 2005, private communication

Jahoda, K., Lockman, F. J., & McCammon, D. 1990, ApJ, 354, 184

Jenness, T., Stevens, J. A., Archibald, E. N., Economou, F., Jessop, N. E. & Robson, E. I. 2002, MNRAS, 336, 14

Khan, S. A., Shafer, R. A., Benford, D. J., Staguhn, J. G., Chanial, P., Le Floc'h, E., Babbedge, T. S. R., Farrah, D., Moseley, S. H., Dwek, E., Clements, D. L., Sumner, T. J., Ashby, M. L. N., Brand, K., Brodwin, M., Eisenhardt, P. R., Elston, R., Gonzalez, A. H., Mckenzie, E., & Murray, S. S., 2004, preprint (astro-ph/0508405)

Klaas, U., Haas, M, Muller, S. A. H., Chini, R., Schulz, B., Coulson, I., Hippelein, H., Wilke, K., Albrecht, M., & Lemke, D. 2001, A&A, 379, 823

Kovács, A., et al., 2005, ApJ, in prep.

Laurent, G. T., Aguirre, J. E., Glenn, J., Ade, P. A. R., Bock, J. J., Edgington, S. F., Goldin, A., Golwala, S. R., Haig, D., Lange, A. E., Maloney, P. R., Mauskopf, P. D., Nguyen, H., Rossinot, P., Sayers, J., & Stover, P. 2005, ApJ, 623, 742

Lehmann, I., Hasinger, G., Schmidt, M., Giacconi, R., Trumper, J., Zamorani, G., Gunn, J. E., Pozzetti, L., Schneider, D. P., Stanke, T., Szokoly, G., Thompson, D., & Wilson, G. 2001, A&A, 371, 833

Lilly, S. J., Eales, S. A., Gear, W. K. P., Hammer, F., Le Fevre, O., Crampton, D., Bond, J. R., & Loretta, D. 1999, ApJ, 518, 641

Lutz, D., Dunlop, J. S., Almaini, O., Andreani, P., Blain, A., Efstathiou, A., Fox, M., Genzel, R., Hasinger, G., Hughes, D., Ivison, R. J., Lawrence, A., Mann, R. G., Oliver, S., Peacock, J. A., Rigopoulou, D., Rowan-Robinson, M., Scott, S., Sergeant, S., & Tacconi, L. 2001, A&A, 378, 70

Mainieri, V., Bergeron, J., Hasinger, G., Lehmann, I., Rosati, P., Schmidt, M., Szokoly, G., & Della Ceca, R. 2002, A&A, 393, 425

Maloney, P. R., Glenn, J., Aguirre, J. E., Golwala, S. R., Laurent, G. L., Ade, P. A. R., Bock, J. J., Edgington, S. F., Goldin, A., Haig, D., Lange, A. E., Mauskopf, P. D., Nguyen, H, Rossinot, P., Sayers, J., & Stover, P. 2005, preprint (astro-ph/0508563)

Marshall, H. L. 1985, ApJ, 289, 457

Masi, S., Ade, P. A. R., Bock, J. J., Boscaleri, A., Crill, B. P., de Bernardis, P., Giacometti, M., Hivon, E., Hristov, V. V., Lange, A. E., Mauskopf, P. D., Montroy, T., Netterfield, C. B., Pascale, E., Piacentini, F., Prunet, S., & Ruhl, J. 2001, ApJ, 553, L93

Murdoch, H. S., Crawford, D. F., & Jauncey, D. L. 1973, ApJ, 183, 1

Murtagh, F. & Heck, A. 1987 *Multivariate Data Analysis*, Kluwer Academic Publishers, Boston

Naylor, B. J. et al. in *Proc. of the SPIE*, Z-Spec: A Broadband, Direct-Detection Millimeter-Wave Spectrometer, 4855, 239

Neri, R., Genzel, R., Ivison, R. J., Bertoldi, F., Blain, A. W., Chapman, S. C., Cox, P., Greve, T. R., Omont, A., & Frayer, D. T. 2003, ApJ, 597, L113

Omont, A., Cox, P., Bertoldi, F., McMahon, R. G., Carilli, C., & Isaak, K. G. 2001, A&A, 374, 371

Ossenkopf, V., & Henning, T. 1994, A&A, 291, 943

Oyabu, S., Yun, M. S., Murayama, T., Sanders, D. B., Kawara, K., Taniguchi, Y., Veilleux, S., Okuda, H., Matsuhara, H., Cowie, L. L., Sato, Y., Wakamatsu, K., & Sofue, Y. 2005, preprint (astro-ph/0507240)

Peebles, P.J.E., 1993 *Principles of Physical Cosmology*, Princeton University Press, New Jersey

Priddey, R. S., & McMahon, R. G. 2001, MNRAS, 324, L17

Puget, J.-L., Abergel, A., Bernard, J.-P., Boulanger, F., Burton, W. B., Desert, F.-X., & Hartmann, D. 1996, A&A, 308, L5

Rodighiero, G., & Franceschini, A. 2004, A&A, 419, L55

Rowan-Robinson, M. 2000, MNRAS, 316, 885

Rowan-Robinson, M., Mann, R. G., Oliver, S. J., Efstathiou, A., Eaton, N., Goldschmidt, P., Mobasher, B., Serjeant, S. B. G., Sumner, T. J., Danese, L., Elbaz, D., Franceschini, A., Egami, E., Knotizas, M., Lawrence, A., McMahon, R., Norgaard-Nielsen, H. U., Perez-Fournon, I., & Gonzalez-Serrano, J. I. 1997, MNRAS, 289, 490

Sandell, G. 1994, MNRAS, 271, 75

Sanders, D. B. 1999, Ap&SS, 266, 331

Sanders, D. B., & Mirabel, I. F. 1996, ARA&A, 34, 749

Sawicki, M. 2002, AJ, 124, 3050

Scheuer, P. A. G. 1957, Proc. Cambridge Philos. Soc., 53, 764

Scheuer, P. A. G. 1974, MNRAS, 166, 329

Scott, S. E., Fox, M. J., Dunlop, J. S., Serjeant, S., Peacock, J. A., Ivison, R. J., Oliver, S., Mann, R. G., Lawrence, A., Efstathiou, A., Rowan-Robinson, M., Hughes, D. H., Archibald, E. N., Blain, A., & Longair, M. 2002, MNRAS, 331, 817

Scoville, N. Z., & Young, J. S. 1983, ApJ, 265, 148

Sheth, K., Blain, A. W., Kneib, J., Frayer, D. T., van der Werf, P. P., & Knudsen, K. K. 2004, ApJ, 614, L5

Silva, L., Granato, G. L., Bressan, A., & Danese, L. 1998, ApJ, 509, 103

Smail, I., Ivison, R. J., Blain, A. W., & Kneib, J.-P. 2002, MNRAS, 331, 495

Steidel, C. C., Hamilton, D. 1993, AJ, 105, 2017

Stompor, R., Abroe, M., Ade, P., Balbi, A., Barbosa, D., Brock, J., Borrill, J., Boscaleri, A., de Bernardis, P., Ferreira, P. G., Hanany, S., Hristov, V., Jaffe, A. H., Lee, A. T., Pascale, E., Rabii, B., Richards, P. L., Smoot, G. F., Winant, C. D., & Wu, J. H. P. 2001, ApJ, 561, L7

Swinbank, A. M., Smail, I., Chapman, S. C., Blain, A. W., Ivison, R.J., & Keel, W. C. 2004, ApJ, 617, 64

Thompson, D., Beckwith, S. V.W., Fockenbrock, R., Fried, J., Hippelein, H., Huang, J.-S., von Kuhlmann, B., Leinert, Ch., Meisenheimer, K., Phelps, S., Roser, H.-J., Thommes, E., & Wolf, C. 1999, ApJ, 523, 100

Thronson, H., & Telesco, C. 1986, ApJ, 311, 98

Ulich, B. L., Haas, R. W. 1976, ApJS, 30, 247

Weatherley, S. J., & Warren, S. J. 2003, MNRAS, 345, L29

Webb, T. M. A., Lilly, S. J., Clements, D. L., Eales, S., Yun, M., Brodwin, M., Dunne, L., & Gear, W. K. 2003, ApJ, 597, 680

Wiklind, T. 2003, ApJ, 588, 736

Wilson, G., Huang, J.-S., Perez-Gonzalez, P. G., Egami, E., Ivison, R. J., Rigby, J. R., Alonzo-Herrero, A., Barmby, P., Dole, H., Fazio, G. G., Le Floc'h, E., Papovich, C., Rigopoulou, D., Bai, L., Engelbracht, C. W., Frayer, D., Gordon, K. D., Hines, D. C., Misselt, K. A., Miyazaki, S., Morrison, J. E., Rieke, G. H., Rieke, M. J., & Surace, J. 2004, ApJS, 154, 107

Wootten, A. 2001, in *ASP Conf. Series*, Science with the Atacama Large Millimeter Array, 235

Yan, L., McCarthy, P. J., Weymann, R. J., Malkan, M. A., Teplitz, H. I., Storrie-Lombardi, L. J., Smith, M., & Dressler, A. 2000, AJ, 120, 575

Yun, M. S., & Carilli, C. L. 2002, ApJ, 568, 88

Yun, M. S., Reddy, N. A., & Condon, J. J. 2001, ApJ, 554, 803

Yun, M. S., et al., 2005, in prep

Zhang, P., Pen, U.-L., & Wang, B. 2002, ApJ, 577, 555

Appendix A

Cleaning Formalism

A.1 Correlated Noise Removal

A.1.1 Introduction

Bolocam is designed to map the sky in several observation modes: Raster scanning, in which the telescope is driven across the sky at a fixed scan rate; Drift scanning, in which the telescope remains fixed and the relative rotation of the sky provides spatial coverage; Chopping, in which the oscillation of the secondary mirror provides on-beam and off-beam signals. To deal with the effects of atmospheric emission and low-frequency instrument drift, which contribute to varying degrees depending on the observation mode, a variety of data cleaning techniques have been implemented. Because sky noise dominates the signal from all but the brightest extra-galactic sources by three or more orders of magnitude, a careful treatment of the noise is required. This appendix focuses on the removal of channel-correlated sky and instrument noise directly from the time stream.

A.1.2 Correlated Noise

Bolocam's 144 element bolometer array is advantageous not only in its increased mapping speeds and large field-of-view, but also in the treatment of correlated noise. The term correlated in this document refers to a time-dependent signal whose signature is seen in more than one bolometer channel. Minor temperature variations of the focal plane and microphonics from telescope motion introduce voltage drifts that are correlated across all of the bolometer channels. Furthermore, the bolometer beams have a 90% overlap in the lower atmosphere, with each bolometer a witness the the same variability of the sky emission. (To facilitate removal of fluctuating atmospheric water vapor emission [sky noise] from the bolometer signals, Bolocam was designed such that the feed horn beams overlap maximally on the primary mirror of the telescope and therefore sample very similar columns of atmosphere.) Thus, the sky noise, which dominates the fundamental instrument noise by a factor of ~ 100, is a nearly common-mode signal.

A proper correlation analysis of the good bolometer signals thus enables us to construct and subtract a correlated noise template from the data streams. Such correlation is extremely beneficial for the software removal of $1/f$ noise contributions because, as will be described below, it allows the approximation of these contributions by simply taking averages over many bolometer channels. However, note that correlation alone does not ensure that the removal of a correlated signal will be straightforward. Here we are aided greatly by the fact that the $1/f$ noise components are correlated in **time**, whereas the astrophysical signal being measured is correlated in **space**. Put differently, the time-functionality of the astronomical signal produced by our scan strategy is, on average, completely **uncorrelated** to the time-functionality of the sky noise, which is seen nearly identically in each bolometer channel. It is this fact that is actually being exploited by the noise removal portion of the cleaning software, which will now be discussed in detail.

A.1.3 Average Subtraction

For bright and extended sources, a principal component analysis often removes a significant amount of source flux (see § A.1.4). It is in these cases in which a simple average sky subtraction is appropriate. Furthermore, much of the source signal that is removed via an average subtraction may be regained with an iterative cleaning technique.

A sky template for each subscan is obtained by simply taking an average of all of the working bolometers for each time element,

$$S_i = \frac{\sum_{j=1}^{n_i} B_{\mathrm{raw},j,i}}{n_i},$$

where S_i is the sky template (estimate of the correlated sky and instrument noise) for time element i, $B_{\mathrm{raw},j,i}$ is the signal for bolometer j at time i, and n_i are the number of good bolometers for time element i. Note that n_i may vary for each time element, as flagged bolometers due to cosmic rays, known sources, etc... are not included in the determination of the sky template.

The sky template is then mean subtracted to prevent the mean from skewing the correlation of the template to the individual bolometer time streams,

$$S'_i = S_i - \frac{\sum_{i=1}^{m} S_i}{m},$$

where m is the number of time elements in the subscan. This mean-subtracted sky template is then correlated to each of the individual bolometer time streams to obtain the coefficient of correlated noise (C_j), which is the sky template corrected for the responsivity of each bolometer,

$$C_j = \frac{\sum_{i=1}^{m} S'_i B_{\mathrm{raw},j,i}}{\sum_{i=1}^{m} S'_i}. \tag{A.1}$$

The cleaned bolometer time stream is then calculated by subtracting out the sky template, scaled by C_j,

$$B_{\mathrm{clean},j,i} = B_{\mathrm{raw},j,i} - C_j S'_i.$$

Finally, the mean of each time trace is subtracted to remove any remaining DC level,

$$B'_{\mathrm{clean},j,i} = B_{\mathrm{clean},j,i} - \frac{\sum_{i=0}^{m} B_{\mathrm{clean},j,i}}{m}. \tag{A.2}$$

Note that for very bright sources (i.e. flux calibrators and pointing sources), multiple subscans for each bolometer are concatenated to ensure that the source contributes negligibly to the fit to the sky template (Equation A.1) as well as preventing a negative trough around the source when performing the final mean subtraction (Equation A.2). This concatenated version of the average subtraction was used for cleaning the calibrators and pointing sources of the January and May 2003 observing runs.

A.1.4 Principal Component Analysis

For observations where the sky and instrument noise dominate sources signal by many orders of magnitude, a principal component analysis (PCA) has been developed to rigorously remove correlated $1/f$ noise. This technique is applicable for dim sources because the source signal will contribute negligibly to any sky template that we develop. The PCA decomposition may be applied to both raster scan and chopped data, after chop demodulation in the latter case.

The formalism of the PCA analysis is standard (see, e.g., Murtagh & Heck, 1987). Here the covariance matrix is built from the n bolometers by m time elements matrix for each subscan. Eigenfunctions of the orthogonal decomposition that have “large” eigenvalues, corresponding to large contributions to the correlated noise, are nulled and the resulting functions are transformed back into individual bolometer time streams. This technique is applicable for dim ($\lesssim$10 mJy) point sources and other blank-field surveys (i.e., submillimeter galaxies) because the source signal contributes negligibly to the sky templates and is largely uncorrelated from bolometer to bolometer. The PCA technique is not appropriate for extended sources, however, in which case the bolometers see correlated astrophysical signals, which are then attenuated (although iterative mapping techniques may mitigate this limitation).

To ensure that the DC level of each of the bolometer time traces is zero (as it approximately should be from the high-pass filter in the lock-in amplifier), we first subtract the mean of the time streams:

$$B'_{raw,j,i} = B_{raw,j,i} - \frac{\sum_{i=0}^{m} B_{raw,j,i}}{m}.$$

We next calculate the correlation matrix, C, of the raw data:

$$\mathbf{C} = \mathbf{B}\,\mathbf{B}^T,$$

where $\mathbf{B}$ is the n bolometers by m time elements matrix of the mean-subtracted raw data, and $\mathbf{B}^T$ is its transpose. $C_{j,j}$ represents the variance of the time stream of bolometer j, and $C_{j,k}$ $(j \neq k)$ gives correlation of the time stream of bolometer j with the time stream of bolometer k ($\mathbf{C}$ is an n by n real and symmetric array.). For clarity, matrices in this section will be designated in boldface. Note that our PCA analysis does implement the flagging of bad data points due to cosmic rays, known sources, etc... (just as in the average sky subtraction technique). This is to ensure that the use of flags does not skew the correlation matrix. The flagged data are not included in constructing the eigenfunctions.

In order to decompose the bolometer signals into n orthogonal eigenvectors of length n, and n corresponding eigenvalues, we wish to solve the following linear equation:

$$\mathbf{C}\mathbf{R}_j = \lambda_j \mathbf{R}_j,$$

where λ is the jth eigenvalue and $\mathbf{R}_j$ is the n element corresponding eigenvector of length unity. Since each of the n good bolometer time streams are independent, we expect n unique eigenvalues and therefore n unique sets of eigenvectors. The set of eigenvectors is the rotation matrix needed to transform the n by m bolometer time streams into an orthogonal n by m set of eigenfunctions, $\mathbf{F}$, each of which contributes to raw bolometer signals:

$$\mathbf{F} = \mathbf{R}^T\mathbf{B}. \tag{A.3}$$

The eigenvalues and eigenvectors of our linear system of bolometer time traces are defined by the condition:

$$\mathbf{R}^T \mathbf{C}\,\mathbf{R} = \lambda,$$

where λ is diagonal:

$$\sum_k^l R_{i,k} C_{l,k} R_{j,l} = \lambda_i \delta_{i,j}.$$

It can also be shown that $\mathbf{F}\,\mathbf{F}^T$ is also diagonal:

$$\begin{aligned} \lambda = \text{diagonal} &= \mathbf{R}^T\,\mathbf{C}\,\mathbf{R} \\ &= \mathbf{R}^T\,\mathbf{B}\,\mathbf{B}^T\,\mathbf{R} \\ &= \mathbf{R}^T\,\mathbf{B}\,\left(\mathbf{R}^T\,\mathbf{B}\right)^T \\ &= \mathbf{F}\,\mathbf{F}^T. \end{aligned}$$

The eigensystem decomposition was performed using the EigenQL IDL routine, which computes the eigenvalues and eigenvectors using Householder reductions (to reduce the real, symmetric **C** array to tridiagonal form) and the QL method with implicit shifts (Section 11.3 Numerical Recipes in C: The Art of Scientific Computing, 2nd edition).

To recompose the bolometer time streams from the eigensystem decomposition, one simply inverts Equation A.3, yielding

$$\begin{aligned} \mathbf{B} &= \mathbf{R}\,\left(\mathbf{R}^T\,\mathbf{B}\right) \\ &= \mathbf{R}\,\mathbf{F}. \end{aligned} \tag{A.4}$$

Unaltered, Equation A.4 would regenerate the mean-subtracted raw bolometer time streams. In order to remove the correlated instrument and sky noise from the data, we must first perform a cut on the largest eigenvalues, null their corresponding eigenfunctions, and rotate back using the modified eigenfunction matrix,

$$\mathbf{B} = \mathbf{R}\,\mathbf{F}',$$

where $F'_{j,i} = 0$ for all i at large values of λ_j. The distribution of eigenvalues for a typical Lockman Hole blank field observation during the January 2003 observing run can be seen in Figure A.1.

The precise level of the cut on the large eigenvalues is somewhat arbitrary, with large eigenvalues corresponding to eigenfunctions that are dominated by correlated sky and instrument noise. The greater the number of eigenfunctions that are nulled, the lower the resulting noise in the cleaned time stream, but the correspondingly greater source flux removed (see § 5.2). Empirically (from January 2003 Lockman Hole raster scan observations), an iterative cut with the nulling of eigenfunctions with eigenvalues $> 3\,\sigma$ from the mean of the eigenvalue distribution produces a balance between sky emission removal and source flux density reduction in simulated observations by maximizing the S/N. Because the distribution of eigenvalues for each observation is characterized by a few outliers (typically $4 - 7$) at large σ-values, the overall variance of the time stream is largely dominated by these eigenvalues, resulting in a S/N that is insensitive to the cut threshold for $2 - 5\ \sigma$. (Furthermore, the distribution of source candidates in the combined Lockman Hole map was invariant under variations in the cut threshold in this range.)

Because the distribution of eigenvalues is approximately exponential, the logarithm of the distribution is approximately Gaussian. It is on this distribution that the iterative cut is performed. The dashed line in Figure A.1 shows the result of this cut on the eigenvalue distribution.

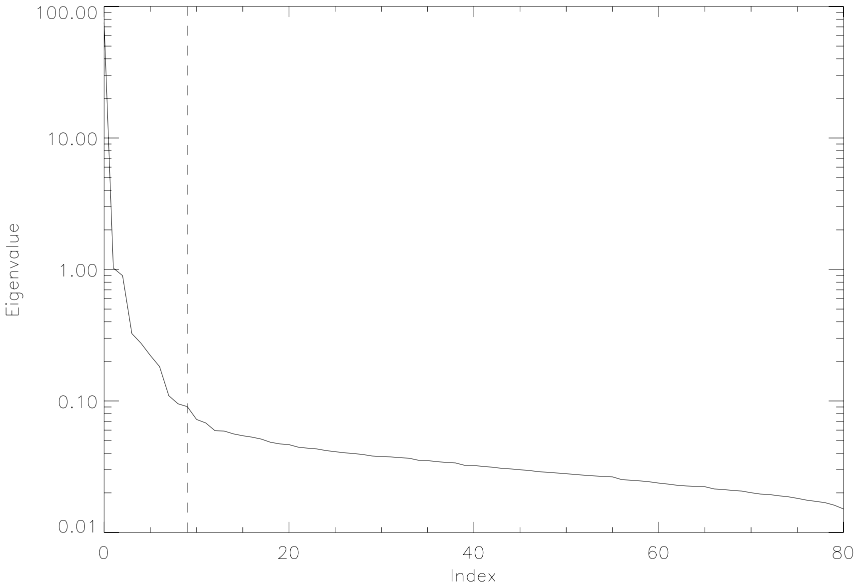

Figure A.1 Plot of eigenvalues for a typical observation of the Lockman Hole taken during the January 2003 observing run. Dashed vertical line represents the results of an iterative 3σ cut on large eigenvalues, whose corresponding eigenfunctions are subsequently removed from the raw bolometer time streams.

Appendix B

Calibration Formalism

B.1 Introduction

Because the Bolocam instrument measures the voltage response of a current-biased bolometer as it moves over a source, it is necessary to compare this response to a calibration source of known flux in order to obtain the true fluxes of blank field source candidates. Because our flux calibrators are hundreds or thousands of times brighter than the dim submillimeter point sources that we are searching for, the non-linearity and finite beam size must be accounted for. Furthermore, the flux calibration is a function of both the atmospheric attenuation and bolometer loading. This appendix details how the flux calibration was obtained for the January 2003 observing run.

B.2 Observations

Since the Bolocam calibration sources are a subset of the sources used for pointing, the observation and reduction of the raw files is similar. A 149-element subset of the 307 raster-scanned pointing observations were used for flux calibration. Only planets and sources from the Sandell (1994) and Jenness et al. (2002) catalogs, whose 1.1 mm fluxes are accurately known, were used. The calibration sources were selected by their bright submillimeter fluxes and proximity to the science fields, including planets (Mars, Jupiter, and Saturn), ultracompact H_{II} regions (W3(OH), G45.1)), low luminosity protostellar sources (IRAS 16293-2422, L1551-IRS5 and NGC 2071IR), and AGB, planetary, and protoplanetary stars (OH231.8+4.2 and IRC+10216). Quasars/blazars (3C273, 3C279, 3C345, 0923+0392/4C+39.25) and molecular clouds (NGC1333-IRAS 4A), while suitable for pointing, were not used for flux calibration because of uncertainty in their 1.1 mm fluxes (due to variability and/or lack of published fluxes). Observations of the calibration sources were taken at the same scanning speeds as the science observations ($60''$ s^{-1} for scanned observations, $5''$ s^{-1} for chopped observations). Chopped observations of the pointing and science fields were taken at chopping frequencies of both 1 and 2 Hz. The size of the pointing fields were generally small ($\sim 4'$ x $4'$), although several larger maps ($10' \times 10'$) were made of Mars in order for the source pass over the entire array. Gross pointing corrections during the observing run were accomplished by adjusting the quadratic telescope pointing terms (T-terms) as a function of zenith angle and the global pointing model described in § 5.3.

B.3 Reductions

Observations of flux calibrators were reduced with the Bolocam software pipeline in the same manner as the sources used for pointing calibration. The raw pointing files were cleaned via a average sky subtraction technique, with a point source filter applied to the timestream. Individual bolometer maps (alt/az) were created at sub beam-sized pixelization ($10''$ pixel^{-1}). The point sources in each of the individual bolometer maps were then centroided by fitting a 7-parameter, two dimensional Gaussian to the maps. A detailed account of the preliminary data reduction on the flux and pointing calibrators can be found in § 5.3.

The flux (in volts) of the the calibration source was obtained from the mean of the individual bolometer peak values from the Gaussian fits. (Note that an iterative 3 σ cut on peak value, σ_x, and σ_y) was performed to eliminate bolometers that did not pass through the source. Source fluxes (in Jy) were obtained from Sandell (1994) and

Jenness et al. (2002), and from the JCMT planetary flux calibration website.[1]

B.4 Spectral Response

The fluxes of the primary calibrators as listed on the JCMT website assume the SCUBA "1.1 mm" bandpass, which has a band center of 264.0 GHz. This is considerably different from the Bolocam band center of 273 GHz as well as the UKT14 band center (271.6 GHz) from Sandell (1994). Thus the in-band fluxes listed on the JCMT website and Sandell (1994) must be corrected for the specific spectral response of Bolocam.

In order to obtain a more accurate estimate of the true Bolocam fluxes of the primary calibrators, Fourier Transform Spectroscopy (FTS) was implemented to provide spectral responses for each of the bolometers (including the 1.1 mm filter stack). Brightness temperatures as a function of frequency from the JCMT website were used to calculate bolometric flux densities at each wavelength. (These flux densities are consistent with what is on the JCMT website.) Figure B.1 shows the spectral response of a typical bolometer.

For each bolometer, a total flux was calculated by integrating the source response function (F_ν) over our transmission spectrum (T_ν):

$$F_{\text{total}} = \frac{\int_{200\text{GHz}}^{500\text{GHz}} F_\nu T_\nu d\nu}{\int_{200\text{GHz}}^{500\text{GHz}} T_\nu d\nu}.$$

The integration limits of 200 GHz and 500 GHz were chosen to ignore leaks in the FTS transmission spectrum data that are blocked by the Bolocam window.

Fluxes of the primary (planetary) calibrators in the Bolocam bandpass are 5% larger than those quoted by the JCMT for SCUBA. The bolometer-to-bolometer response variation is small, with an rms of 1%. This correction was performed for the Sandell (1994) calibrators as well, but because the UKT14 band center and bandwidth (74 GHz) are similar to our own, the effect is small.

---

[1] http://www.jach.hawaii.edu/jac-bin/planetflux.pl.

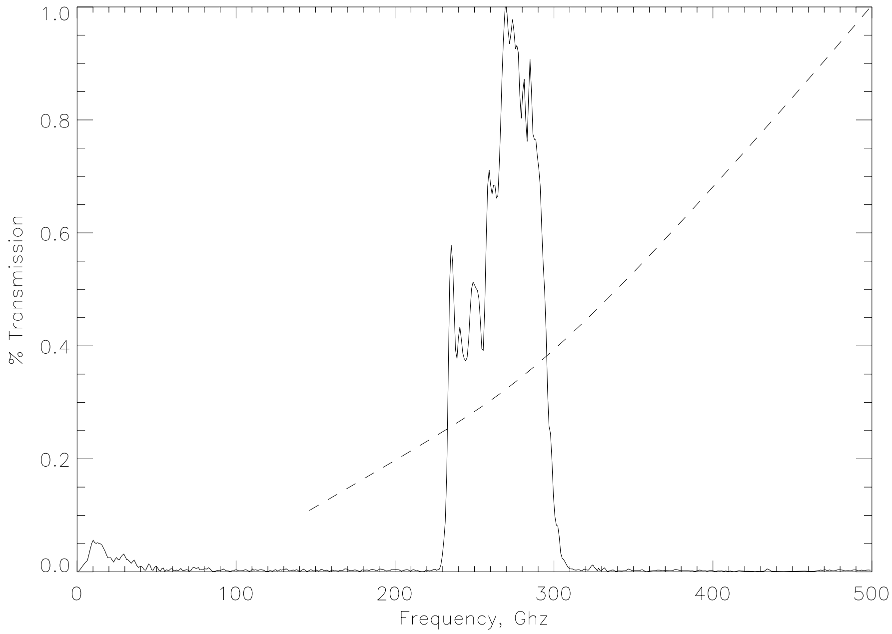

Figure B.1 Solid: Fourier Transform Spectroscopy (FTS) response of a typical Bolocam bolometer with the 1.1 mm filter stack. Dashed: Normalized flux of Saturn (Jan. 26th, 2003) obtained from brightness temperatures from JCMT planetary flux calibration website.

B.5 Beam Coupling Efficiency

Because the finite angular size of the primary calibrators (During the January 2003 observing run, Saturn and Jupiter had a semi-diameters of $10''$ and $22''$, respectively) is a substantial fraction of the Bolocam 1.1 mm beam ($31''$), we must take into account the beam coupling efficiency. (Since the response of the Bolocam beam is, to first order, Gaussian, the response to an extended source is not constant as a function of radius.)

From Ulich & Haas (1976), the forward beam coupling efficiency for an extended source, which is the ratio of source and beam solid angles, is defined as

$$\begin{aligned}\eta_f &\equiv \frac{\int\int_{source} P_n(\Psi - \Omega) B_n(\Psi) d\Psi}{\int\int_{sky} P_n(\Omega) d\Omega} \\ &\equiv \frac{\Omega_{\text{source}}}{\Omega_{\text{beam}}}, \qquad \text{(B.1)}\end{aligned}$$

where η_f is the forward beam coupling efficiency (dimensionless), B_n is the normalized beam profile, P_n is the normalized source profile, Ψ is the solid angle of the beam on the sky, and Ω is the solid angle of the source.

For a uniformly bright disk with sharp edges,

$$\begin{aligned}B_n &= 1 \quad \text{for} \quad \left[(x - x_o)^2 + (y - y_o)^2\right]^{1/2} \leq R \\ B_n &= 0 \quad \text{for} \quad \left[(x - x_o)^2 + (y - y_o)^2\right]^{1/2} > R,\end{aligned}$$

where R is the radius of the disk. We approximate our beam profile as a Gaussian with amplitude, A:

$$\begin{aligned}P_n &= A \exp\left[-\frac{(x - x_o)^2 + (y - y_o)^2}{2\sigma^2}\right] \\ &= A \exp\left[-4 \ln 2 \frac{(x - x_o)^2 + (y - y_o)^2}{\text{FWHM}^2}\right].\end{aligned}$$

Substituting into Equation B.1, assuming a circular disk, and simplifying, we find

$$\begin{aligned}
\eta_f &= \frac{\int\int_0^R A\exp\left(-4\ln 2\frac{x^2+y^2}{\mathrm{FWHM}^2}\right)d\Psi}{\int\int_{sky} A\exp\left(-4\ln 2\frac{x^2+y^2}{\mathrm{FWHM}^2}\right)d\Omega} \\
&= \frac{\int_0^{2\pi}\int_0^R \exp\left(-4\ln 2\frac{r^2}{\mathrm{FWHM}^2}\right)r\,dr\,d\theta}{\int_0^{2\pi}\int_0^\infty \exp\left(-4\ln 2\frac{r^2}{\mathrm{FWHM}^2}\right)r\,dr\,d\theta} \\
&= \frac{\int_0^R \exp\left(-4\ln 2\frac{r^2}{\mathrm{FWHM}^2}\right)r\,dr}{\int_0^\infty \exp\left(-4\ln 2\frac{r^2}{\mathrm{FWHM}^2}\right)r\,dr} \\
&= \frac{\int_0^{-4\ln 2\frac{R^2}{\mathrm{FWHM}^2}} e^\alpha d\alpha}{\int_0^\infty e^\alpha d\alpha} \\
&= \frac{\exp\left(-4\ln 2\frac{R^2}{\mathrm{FWHM}^2}\right)-1}{0-1} \\
&= 1-\exp\left(-4\ln 2\frac{R^2}{\mathrm{FWHM}^2}\right).
\end{aligned}$$

In terms of the beam coupling efficiency, η_n, the total flux coming into the beam is

$$F_{\mathrm{beam}} = \eta_f \int\int P_n(\Omega)d\Omega.$$

In order to correct our calibration for the finite size of the source, we must obtain the ratio of the actual flux in our beam, F_{beam}, to that of the flux (F_o) obtained assuming the source to be much smaller than our beam (i.e., point-like):

$$\begin{aligned}
\frac{F_{\mathrm{beam}}}{F_o} &= \frac{\eta_f\int\int P_n(\Omega)d\Omega}{\eta_{fo}\int\int P_n(\Omega)d\Omega} \\
&= \frac{\eta_f}{\eta_{fo}} \\
&= \frac{1-\exp\left(-4\ln 2\frac{R^2}{\mathrm{FWHM}^2}\right)}{\Omega_{\mathrm{source}}/\Omega_{\mathrm{beam}}}. \qquad \text{(B.2)}
\end{aligned}$$

The source solid angle, Ω_{source}, is simply the area of the disk:

$$\Omega_{\mathrm{source}} = \pi R^2.$$

The beam solid angle is the integrated area of the assumed Gaussian:

$$\begin{aligned}
\Omega_{\mathrm{beam}} &= 2\pi\sigma^2 \\
&= \frac{\pi\,\mathrm{FWHM}^2}{4\ln 2},
\end{aligned}$$

giving a ratio of solid angles:

$$\frac{\Omega_{\text{source}}}{\Omega_{\text{beam}}} = 4\ln 2\left(\frac{R^2}{\text{FWHM}^2}\right).$$

Substituting into Equation B.2 produces

$$\frac{F_{\text{beam}}}{F_o} = \frac{1-\exp\left(-4\ln 2\frac{R^2}{\text{FWHM}^2}\right)}{4\ln 2(R^2/\text{FWHM}^2)}. \tag{B.3}$$

This ratio of the flux in our beam to that of the flux assuming a point-like source represents a correction factor that was applied to the true fluxes of the flux calibrators. For sources small compared to the 31″ Bolocam beam (Mars, 3″), this is a small correction (0.99). For larger sources (Saturn, 10″; Jupiter, 22″), this is a substantial correction (0.86 and 0.52 respectively). As a check of our above analysis, Equation B.3 produces results which are consistent with the ”flux in beam” results for the SCUBA detector array on the JCMT flux calibration website.

Figure 5.3 shows our calibration in nV Jy^{-1} for calibration sources taken during the January 2003 observing run as a function of the average DC loading on the bolometers (converted to bolometer voltage at the bias frequency). Because thermal expansion of the telescope structure affects our focus and subsequently the flux entering the beam, only observations taken after 30 minutes post-sunset and before 30 minutes pre-sunrise were used in the fit (this is appropriate, as no daytime Lockman science observations were taken). Calibrator fluxes have been corrected for beam coupling efficiency as well as the Bolocam spectral response. Note that bright sources such as Jupiter cannot be corrected for bolometer non-linearity and are therefore not included, as it is meaningless to assign a single DC level to an observation of a bright source. The quadratic fit to the data was fit to minimize errors between observed and true fluxes.

Appendix C

Mapping Formalism

C.1 Relative Uncertainty

C.1.1 Introduction

When creating a map, many data frames from numerous bolometers go into each pixel. These data frames may derive from different subscans or from entirely different observations taken during different atmospheric conditions. Thus, it is necessary to obtain an estimate of the uncertainty of each frame in the timestream. While flagging pixels that have abnormal characteristics such as cosmic rays, voltage spikes, and bad scans with particularly errant RMS values will prevent these data from contributing to the final map, the remaining "good" data will have varying levels of low frequency noise. Therefore a noise estimate is useful as a way to compare all bolometers and subscans in the data stream to one another in terms of how well the cleaning modules were able to remove correlated $1/f$ noise from them.

C.1.2 Formalism

In this section, I will provide an overview of the formalism used to estimate the relative uncertainty in our measurements and use this information to create a weighted map and determine uncertainties in individual pixel values.

C.1.3 Relative Uncertainties

The relative noise of a bolometer and subscan is characterized in terms of its power spectral density (PSD). The individual PSD of a given subscan and bolometer of a real, time-sequenced function $V(t)$ is the primary diagnostic tool used to determine the amount of $1/f$ noise present in the data and is defined for each bolometer and subscan as

$$PSD(f) = \left[\frac{|V(f)|^2}{\Delta f}\right]^{1/2}, \tag{C.1}$$

where $V(f)$ is the Fast Fourier Transform (FFT) of the signal $V(t)$, and Δf is the lowest frequency (bin width) of the subscan (simply $1/(\Delta t\ M_{samples})$, or the inverse of the total sampling time in the subscan).

The PSD used in Equation C.1 is averaged over all (N) subscans (in quadrature) in a given observation in order to smooth over random noise in individual PSDs (the sky noise is assumed to be roughly constant over an observation), thus providing us with a general measurement of the uncertainty of an individual bolometer over the entire spectral range:

$$\overline{PSD}(f) = \left[\frac{\sum_i^N PSD_i^2(f)}{N}\right]^{1/2}. \tag{C.2}$$

Note that the lowest frequency of each PSD of a given subscan will be determined by the the total number of frames in the subscan. Thus if subscans vary in length, the average in Equation C.2 must be done by binning or interpolating frequencies of component subscans. By this definition, the PSD has units of V $\text{Hz}^{-1/2}$, which is the value appropriate for the assessment of noise (PSD^2 in units of V^2 Hz^{-1} is also commonly used but represents of the power rather than the noise in the signal as a function of frequency).

The relative uncertainty of a bolometer and subscan when detecting a point source is related to its PSD by

$$\sigma^2_{\mathrm{subscan}} = \frac{\int |g'(f)|^2 \, \overline{PSD}(f)^2 \, df}{\left[\int g'(f) \; s(f) \; df\right]^2}, \tag{C.3}$$

where $\overline{PSD}(f)$ is the power spectral density of a given bolometer averaged over all subscans in an observation and the optimal filter $g'(f)$ is the conjugate of a high-pass-filtered Gaussian (digital analogy to the Bolocam lock-in amplifier). The denominator represents a normalization factor with $s(f)$ representing the source in frequency space that we are trying to detect (a point source in most cases). While it remains constant for every subscan and we are only interested in the relative uncertainties between bolometers and subscans, the normalization in Equation C.3 is nevertheless incorporated in the mapping routine for completeness.

Because our signal of interest does not fall throughout the entire frequency range of the PSD, we filter it in Equation C.3 with a optimal filter ($g'(f)$) in order to obtain the uncertainty in the frequency range of interest. $s(t)$ is the expected profile of a point source in our data stream. In frequency space, it is thus a high-pass filtered Gaussian. Assuming white noise, the optimal filter for a source, in frequency space, is the conjugate of this source profile:

$$g'(f) \;=\; s^*(f) \tag{C.4}$$

$$\;=\; [F(f) \; g(f)]^*, \tag{C.5}$$

where F(f) is a digital high-pass filter analogous to the analog filter found in the Bolocam lock-in amplifier, and $g(f)$ is the FFT of a Gaussian normalized to an amplitude of unity and a width equal to (in time space):

$$F(f) = \frac{2\pi i f \tau_1}{1 + 2\pi i f \tau_1} - \frac{2\pi i f \tau_2}{1 + 2\pi i f \tau_2}$$

$$\sigma_{\mathrm{Gaussian}} = \frac{\sigma_{\mathrm{beam}}}{\text{scan speed in ''/s}}$$

where $\tau_1 = 10$ sec and $\tau_2 = 0.82$ msec are the time constants of the Bolocam lock-in high-pass filter. σ_{beam} is equal to $58.5''$ when operating at a wavelength of 2.1 mm and $35''$ at 1.1 mm.

Given the definitions of the optimal filter and source profile in Equations C.4-C.5, the definition of the relative uncertainty of a bolometer in Equation C.3 simplifies to

$$\begin{aligned}
\sigma^2_{\text{subscan}} &= \frac{\int |g'(f)|^2 \, \overline{PSD}(f)^2 \, df}{\left[\int [F(f) \; g(f)]^* \; s(f) \; df\right]^2} \\
&= \frac{\int |g'(f)|^2 \, \overline{PSD}(f)^2 \, df}{\left[\int s^*(f) \; s(f) \; df\right]^2} \\
&= \frac{\int |g'(f)|^2 \, \overline{PSD}(f)^2 \, df}{\left[\int |s(f)|^2 \; df\right]^2} \\
&= \frac{\int |g'(f)|^2 \, \overline{PSD}(f)^2 \, df}{\left[\int |g'(f)|^2 \; df\right]^2}. \qquad \text{(C.6)}
\end{aligned}$$

The lower limit of the integral in Equation C.6 corresponds to the lowest frequency of the shortest subscan, which is simply the inverse of the total time of the subscan $1/(\Delta t \; M_{samples})$. As previously mentioned, when comparing the relative uncertainties of subscans of varying length, a common lower frequency limit must be used in order for the relative uncertainties to have any meaning. The upper limit of the integral is simply the Nyquist frequency, or half the sampling frequency of data acquisition. Thus the upper limit is 25 Hz with our sampling rate of 50 Hz.

Note that the Gaussian filter applied to the PSD as described is valid only when detecting a point source (i.e., the width of the Gaussian is determined by the amount of time for a point source to pass through a beam).

C.1.4 Co-adding Multiple Observations

When using subscans from numerous observations to produce a final co-added map, it is necessary to accurately weight each signal with its corresponding uncertainty to minimize both the final uncertainty in each pixel as well as the pixel-to-pixel dispersion. To do this we use a simple weighted average (expectation value) over N hits in order to calculate each pixel value:

$$< V >= V_{\text{coadd}} = \frac{\sum_i^N \left(V_i/\sigma_i^2\right)}{\sum_i^N \left(1/\sigma_i^2\right)}. \tag{C.7}$$

The final uncertainty in each pixel value is defined as a weighted standard deviation:

$$< \sigma^2 >= \sigma^2_{\text{pix,coadd}} = \frac{\sum_i^N \frac{(V_i - <V>)^2}{\sigma_i^2 (N-1)}}{\sum_i^N \left(1/\sigma_i^2\right)}. \tag{C.8}$$

Because the data are read in and mapped incrementally (one subscan at a time), $< V >$ is not yet known for a given pixel. Thus Equation C.8 must be rearranged to allow specific quantities to be carried through the mapping code:

$$\begin{aligned} < \sigma^2 > &= \frac{\sum_i^N \frac{(V_i - <V>)^2}{\sigma_i^2}}{(N-1)\sum_i^N \left(1/\sigma_i^2\right)} \\ &= \frac{\sum_i^N \left(\frac{V_i^2}{\sigma_i^2} - \frac{2V_i <V>}{\sigma_i^2} + \frac{<V>^2}{\sigma_i^2}\right)}{(N-1)\sum_i^N \left(1/\sigma_i^2\right)} \\ &= \frac{\sum_i^N \left(V_i^2/\sigma_i^2\right) - 2 < V > \sum_i^N \left(V_i/\sigma_i^2\right) + < V >^2 \sum_i^N \left(1/\sigma_i^2\right)}{(N-1)\sum_i^N \left(1/\sigma_i^2\right)}. \end{aligned}$$

Substituting Equation C.7 in for $\sum_i^N (V_i/\sigma_i^2)$:

$$\begin{aligned} < \sigma^2 > &= \frac{\sum_i^N \left(V_i^2/\sigma_i^2\right) - 2 < V >< V > \sum_i^N \left(1/\sigma_i^2\right) + < V >^2 \sum_i^N \left(1/\sigma_i^2\right)}{(N-1)\sum_i^N \left(1/\sigma_i^2\right)} \\ &= \frac{\sum_i^N \left(V_i^2/\sigma_i^2\right) - < V >^2 \sum_i^N \left(1/\sigma_i^2\right)}{(N-1)\sum_i^N \left(1/\sigma_i^2\right)}. \end{aligned} \tag{C.9}$$

Thus the quantities $1/\sigma_i^2$, V_i/σ_i^2, and V_i^2/σ_i^2 are carried through and summed as each subscan is incrementally read in and mapped.

C.2 Error Analysis

In order to verify that we are cleaning and co-adding the data correctly, it is necessary to examine both the mean within-pixel uncertainties as well as the pixel-to-pixel dispersions for multiple observations. This section attempts to describe what we expect the uncertainties to look like as we co-add multiple observations to form a single map.

C.2.1 Pixel-to-Pixel Dispersion

While our multiple observation maps are co-added by weighting each subscan by its corresponding integrated PSD uncertainty, suppose that we have n individual maps, m$_i$, each with an average integration time per pixel T$_i$ and pixel-to-pixel variance of σ_i^2. The optimal combination of the maps is then a simple weighted average:

$$m_{\rm coadd} = \frac{\sum_i^n \left(m_i/\sigma_i^2\right)}{\sum_i^n \left(1/\sigma_i^2\right)}. \tag{C.10}$$

Assuming that there is no signal in the maps (i.e., $< m_i >= 0$ for each individual map), the resulting pixel-to-pixel variance in the co-added map is

$$\sigma^2_{\rm coadd} =< m^2_{\rm coadd} > =< \left[\frac{\sum_i^n \left(m_i/\sigma_i^2\right)}{\sum_i^n \left(1/\sigma_i^2\right)}\right]^2 > . \tag{C.11}$$

Because the denominator contains only map variances rather than the map itself, we can pull it out of the mean:

$$\begin{aligned} \sigma^2_{\rm coadd} &= \frac{< \left[\sum_i^n (m_i/\sigma_i^2)\right]^2 >}{\left[\sum_i^n (1/\sigma_i^2)\right]^2} \\ &= \frac{< \sum_i^n (m_i/\sigma_i^2)^2 > + < \sum_{i\neq j}^n \left(\frac{m_i m_j}{\sigma_i^2 \sigma_j^2}\right) >}{\left[\sum_i^n (1/\sigma_i^2)\right]^2}, \end{aligned}$$

where the sum in the numerator has been split into its respective diagonal and cross terms. The cross terms vanish under the assumption that the maps are uncorrelated with each other (i.e., $< m_i m_j >= 0$ for $i \neq j$):

$$\begin{aligned} \sigma^2_{\rm coadd} &= \frac{\sum_i^n \left(< m_i^2 > /\sigma_i^4\right)}{\left[\sum_i^n (1/\sigma_i^2)\right]^2} \\ &= \frac{\sum_i^n \left(\sigma_i^2/\sigma_i^4\right)}{\left[\sum_i^n (1/\sigma_i^2)\right]^2} \qquad \text{(C.12)} \\ &= \frac{\sum_i^n \left(1/\sigma_i^2\right)}{\left[\sum_i^n (1/\sigma_i^2)\right]^2} \\ &= \frac{1}{\sum_i^n (1/\sigma_i^2)}. \qquad \text{(C.13)} \end{aligned}$$

In other words, the expected co-added map pixel-to-pixel variance is given by reciprocally summing the individual map pixel-to-pixel variances. If all the individual pixel-to-pixel variances are the same ($\sigma_i^2 = \sigma^2$), then the pixel-to-pixel variance of the co-added map goes down as 1/n as expected ($\sigma^2_{\rm coadd} = \sigma^2/n$).

If the noise is independent of time, meaning that the noise is the same in observations with equal integration times, then we define a time-independent instantaneous sensitivity in units of V $\rm s^{1/2}$ which corresponds to the noise in one second of integration time per pixel:

$$\sigma^* = \sigma_i T_i^{1/2}.$$

Given this simple case of time-independent noise, the pixel-to-pixel variance of Equation C.13 becomes

$$\sigma^2_{\rm coadd} = \frac{1}{\sum_i^n (T_i/\sigma^{*^2})} = \sigma^{*^2}/T_{tot}, \tag{C.14}$$

where $T_{tot} = \sum_i^n T_i$. Thus as we would expect, the pixel-to-pixel noise ($\sigma_{\rm coadd}$) for a time-independent instantaneous sensitivity integrates down as $T_{tot}^{-1/2}$.

It is necessary to consider the case of time dependent noise, as we might expect for co-added maps that are comprised of individual observations taken under varying sky conditions. We cannot factor out σ^* out of Equation C.14 and therefore the expected behavior of $\sigma_{\rm coadd}$ with T_{tot} is not obvious. We therefore define a time dependent pixel-to-pixel instantaneous sensitivity for an individual map:

$$\sigma_i^* = \sigma_i T_i^{1/2}. \tag{C.15}$$

We also define an effective time, $T_{\rm eff}$, that corrects the integration times of the maps to account for variations in pixel-to-pixel instantaneous sensitivity between the maps:

$$T_{{\rm eff},i} = T_i \frac{< \sigma_i^{*^2} >}{\sigma_i^{*^2}}, \tag{C.16}$$

where the mean pixel-to-pixel instantaneous sensitivity, $< \sigma_i^{*^2} >$, is calculated as a variance-weighted expectation value:

$$< \sigma_i^{*^2} > = \frac{\sum_i^n (\sigma_i^{*^2}/\sigma^2_{\sigma_i^{*^2}})}{\sum_i^n (1/\sigma^2_{\sigma_i^{*^2}})}. \tag{C.17}$$

The variance of the pixel-to-pixel instantaneous sensitivity ($\sigma^2_{\sigma_i^{*2}}$) is

$$\begin{aligned}
\sigma^2_{\sigma_i^{*2}} &= \sigma^2_{\sigma_i^2 T_i} \\
&= T_i^2 \sigma^2_{\sigma_i^2} \qquad \text{(C.18)} \\
&= T_i^2 \frac{2\sigma_i^4}{N_{\text{pix},i}} \\
&= \frac{2\sigma_i^{*4}}{N_{\text{pix},i}}, \qquad \text{(C.19)}
\end{aligned}$$

where $N_{\text{pix},i}$ is the number of pixels in map i. In Equation C.18, pulling T_i out from the variance yields T_i^2 because the variance of a quantity has units of the square of the quantity's units. Substituting Equation C.19 into Equation C.17 yields

$$\begin{aligned}
< \sigma_i^{*2} > &= \frac{\sum_i^n (\sigma_i^{*2}/(2\sigma_i^{*4}/N_{\text{pix},i}))}{\sum_i^n (1/(2\sigma_i^{*4}/N_{\text{pix},i}))} \\
&= \frac{\sum_i^n (N_{\text{pix},i}/\sigma_i^{*2})}{\sum_i^n (N_{\text{pix},i}/\sigma_i^{*4})}. \qquad \text{(C.20)}
\end{aligned}$$

This quantity is calculated to produce the mean pixel-to-pixel instantaneous sensitivity used in Equation C.16. Note that if all n maps have an equal number of pixels, which is reasonable given multiple identical observations, then Equation C.20 simplifies to

$$< \sigma_i^{*2} > = \frac{\sum_i^n (1/\sigma_i^{*2})}{\sum_i^n (1/\sigma_i^{*4})}. \qquad \text{(C.21)}$$

Thus from Equation C.16, if for an individual map, the pixel-to-pixel instantaneous sensitivity is worse than the average, the effective time will be less than the actual time ($T_{\text{eff}} < T_i$). Equations C.15 and C.16 can be combined to give an expression for the pixel-to-pixel instantaneous map variance in terms of the effective time:

$$\begin{aligned}
\sigma_i^2 &= \frac{\sigma_i^{*2}}{T_i} \\
&= \frac{\sigma_i^{*2}}{T_{\text{eff},i}\sigma_i^{*2} / < \sigma_i^{*2} >} \\
&= \frac{< \sigma_i^{*2} >}{T_{\text{eff},i}}.
\end{aligned}$$

The effective time for maps comprised of several observations is simply

$$T_{\text{eff,coadd}} = \sum_i^n T_{\text{eff},i}. \qquad \text{(C.22)}$$

We now can calculate an expected effective pixel-to-pixel instantaneous sensitivity for a co-added map:

$$\begin{aligned}\sigma^{*^2}_{\rm coadd} &= \sigma^2_{\rm coadd} T_{\rm eff,coadd} \\ &= \frac{1}{\sum_i^n (1/\sigma_i^2)} \sum_i^n T_{{\rm eff},i} \\ &= \frac{1}{\sum_i^n (T_{{\rm eff},i}) / < \sigma_i^{*^2} >} \sum_i^n T_{{\rm eff},i} \\ &= < \sigma_i^{*^2} > .\end{aligned}$$

Rearranging,

$$\sigma^2_{\rm coadd} = \frac{< \sigma_i^{*^2} >}{T_{\rm eff,coadd}}. \tag{C.23}$$

Thus the pixel-to-pixel noise in a map ($\sigma_{\rm coadd}$) should integrate down as $T_{\rm eff,coadd}^{-1/2}$. Inspection of Figure C.1 supports this claim. Note that departure from this relation would indicate that our original assumption of no fixed pattern noise ($< m_i m_j >= 0$) would be invalid and suggest the existence of such map-correlated, non-random, coherent $1/f$ noise. Also note that when co-adding only a subset of the total n observations in Figure C.1, the mean pixel-to-pixel instantaneous sensitivity ($< \sigma_i^{*^2} >$) as calculated by Equation C.20 incorporated all n observations for the determination of the effective times ($T_{{\rm eff},i}$ and $T_{\rm eff,coadd}$). This was done for both simplicity and (more importantly) to prevent observations from being treated differently depending on which other observations it was co-added with.

It is important to point out that the proper pixel-to-pixel dispersion should be calculated as a weighted rms:

$$\sigma^2_{\rm map} = \frac{\sum_i^N (V_i^2/\sigma_i^2)}{\sum_i^N (1/\sigma_i^2)}, \tag{C.24}$$

where V_i is the mean signal value of pixel i (which is assumed to be noise), and σ_i^2 is the within-pixel variance of pixel i (see next section). This expression can be understood by extending the previous analogy of map co-adding to individual pixel values. The

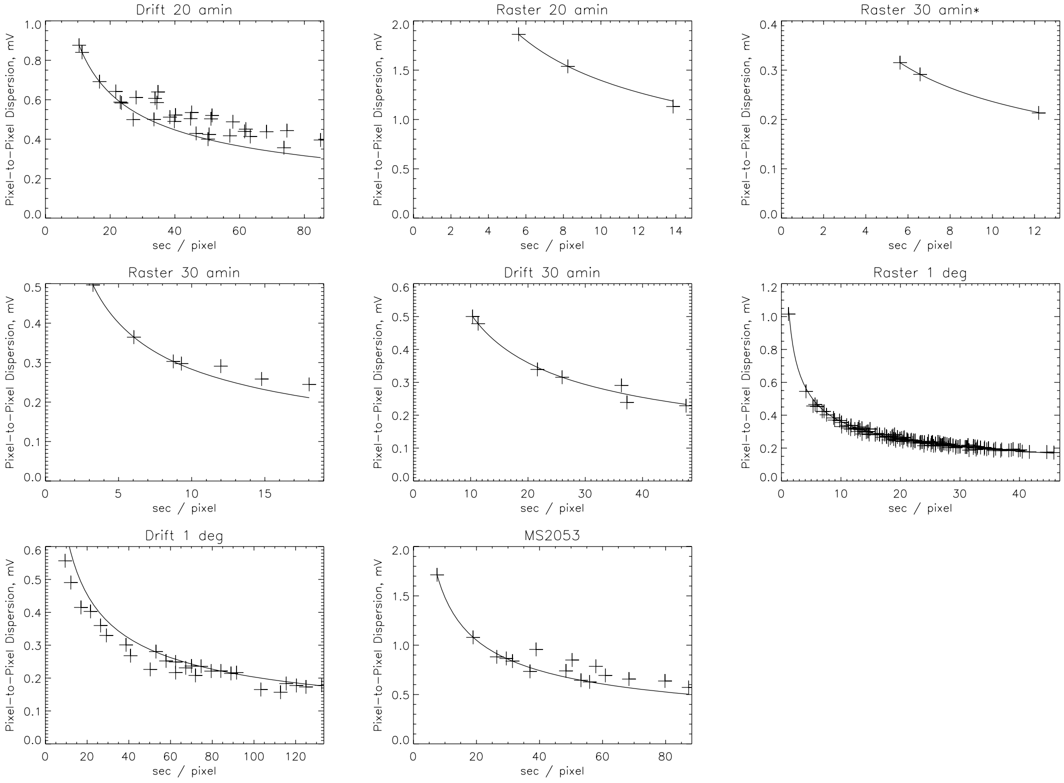

Figure C.1 Plot of pixel-to-pixel dispersion vs. effective time per pixel for blank and galaxy cluster (MS2053) fields of various sizes. Each plotted point represents either an individual or co-added observation. The solid line represents a $T_{\mathrm{eff,coadd}}^{-1/2}$ fit, normalized to the observation with the least integration time.

variance of each pixel, σ_i^2 is related to the within-pixel instantaneous sensitivity by the now familiar expression:

$$\sigma_i^* = \sigma_i T_i^{1/2}. \tag{C.25}$$

One can similarly calculate an effective time:

$$T_{\mathrm{eff},i} = T_i \frac{<\sigma_i^{*^2}>}{\sigma_i^{*^2}} = \frac{<\sigma_i^{*^2}>}{\sigma_i^2}. \tag{C.26}$$

Equations C.25 and C.26 lead to equivalent expressions for the pixel-to-pixel variance of a co-added map:

$$\begin{aligned} \sigma^2_{\mathrm{map}} = \frac{\sum_i^N (V_i^2 T_i/\sigma_i^{*^2})}{\sum_i^N (T_i/\sigma_i^{*^2})} &= \frac{\sum_i^N (V_i^2 T_{\mathrm{eff},i}/<\sigma_i^{*^2}>)}{\sum_i^N (T_{\mathrm{eff},i}/<\sigma_i^{*^2}>)} \\ &= \frac{\sum_i^N (V_i^2 T_{\mathrm{eff},i})}{\sum_i^N T_{\mathrm{eff},i}}. \end{aligned}$$

In the limit that instantaneous sensitivity is uniform throughout the map ($\sigma_i^{*^2} =< \sigma_i^{*^2} >$) and the map coverage is uniform ($T_i =< T_i >$), or equivalently if the effective time is uniform throughout the map ($T_{\mathrm{eff},i} =< T_{\mathrm{eff},i} >$), then

$$\sigma^2_{\mathrm{map}} = \frac{\sum_i^N V_i^2}{N},$$

which is the general standard deviation expression. Thus, because of possible variations of within-pixel instantaneous sensitivity and coverage over the map, it is important to use within-pixel variances as weights (Equation C.24) when calculating the pixel-to-pixel standard deviation of a map.

Given that the effective time for a co-added observation ($T_{\mathrm{eff,coadd}}$) as defined by Equation C.22 is simply the sum of the effective times of individual observations, one may naively expect the following:

$$T_{\mathrm{eff,coadd}} = \sum_i^n T_{\mathrm{eff},i} \overset{?}{=} \sum_i^n T_i. \tag{C.27}$$

This claim initially seems reasonably because the effective times for individual maps should be symmetrically distributed around the actual times such that $< T_{\mathrm{eff},i} - T_i >= 0$

(i.e., Gaussian distributed). However, Equation C.27 is valid only in the simple case of a constant pixel-to-pixel instantaneous sensitivity ($\sigma_i^{*^2} =< \sigma_i^{*^2} >$):

$$\begin{aligned} T_{\mathrm{eff,coadd}} &= \sum_i^n T_{\mathrm{eff},i} \\ &= \sum_i^n T_i \frac{< \sigma_i^{*^2} >}{\sigma_i^{*^2}} \\ &= \sum_i^n T_i. \end{aligned} \tag{C.28}$$

For variations in pixel-to-pixel instantaneous sensitivity, we substitute the definition of $< \sigma_i^{*^2} >$ from Equation C.21 (assuming all maps have an equal number of pixels) into Equation C.28, which yields

$$\begin{aligned} T_{\mathrm{eff,coadd}} &= < \sigma_i^{*^2} > \sum_i^n \frac{T_i}{\sigma_i^{*^2}} \\ &= \frac{\sum_i^n (1/\sigma_i^{*^2})}{\sum_i^n (1/\sigma_i^{*^4})} \sum_i^n \frac{T_i}{\sigma_i^{*^2}}. \end{aligned}$$

Only in the limit of $\sigma_i^{*^2}$ being the same for all i (constant pixel-to-pixel instantaneous sensitivity) does this expression reduce to $\sum_i^n T_i$. In the general case, however, $T_{\mathrm{eff,coadd}} \leq \sum_i^n T_i$. This is a surprizing result in that one expects the $T_{\mathrm{eff},i} - T_i$ differences to be distributed in some simple way (i.e., Gaussian distributed) around zero, causing $\sum_i^n (T_{\mathrm{eff},i} - T_i)$ to vanish (thus having $T_{\mathrm{eff,coadd}} = \sum_i^n T_i$). But the $T_{\mathrm{eff},i} - T_i$ differences are distributed in a more complicated way as we will now qualitatively show.

First, the $\sigma_i^{*^2}$ values used to define $T_{\mathrm{eff},i}$ in Equation C.16 are not distributed in a simple Gaussian fashion around $< \sigma_i^{*^2} >$ because $< \sigma_i^{*^2} >$ is not defined as a simple mean of $\sigma_i^{*^2}$. Rather we define the expectation value of the pixel-to-pixel instantaneous sensitivity as in Equation C.21:

$$< \sigma_i^{*^2} >= \frac{\sum_i^n (1/\sigma_i^{*^2})}{\sum_i^n (1/\sigma_i^{*^4})}. \tag{C.29}$$

This proper definition of the weighted mean tends to causes $< \sigma_i^{*^2} >$ to be lower than the simple mean would be. This can be understood as follows. In the simple mean

$$< \sigma_i^{*^2} >= \frac{\sum_i^n \sigma_i^{*^2}}{n},$$

all the pixel-to-pixel instantaneous sensitivities ($\sigma_i^{*^2}$) contribute with equal weight and the resulting mean is at about the median of the $\sigma_i^{*^2}$ distribution. If instead, one used a reciprocal mean, weighting each observation in the mean by the inverse of the pixel-pixel instantaneous sensitivity:

$$\begin{aligned} < \sigma_i^{*^2} > &= \frac{\sum_i^n (\sigma_i^{*^2}/\sigma_i^{*^2})}{\sum_i^n (1/\sigma_i^{*^2})} \\ &= \frac{n}{\sum_i^n (1/\sigma_i^{*^2})}, \end{aligned} \tag{C.30}$$

the lower $\sigma_i^{*^2}$ values are more heavily weighted, pulling down $< \sigma_i^{*^2} >$ with respect to the simple mean. Essentially, this version corresponds to a weighted mean with a weighting factor of the i'th observation equal to $w_i = 1/\sigma_i^{*^2}$, so observations with low $\sigma_i^{*^2}$ points contribute more to the final value of $< \sigma_i^{*^2} >$. The correct version of the weighted mean which we use, Equation C.29, attributes even more importance to the low $\sigma_i^{*^2}$ points, since the weighting factor of the i'th observation is $w_i = 1/\sigma_i^{*^4}$. So, the $\sigma_i^{*^2}$ are distributed asymmetrically around $< \sigma_i^{*^2} >$, with fewer points below the mean than above. Given this asymmetric distribution we would expect the effective times of many observations (each of which are directly proportional to the weighted mean pixel-to-pixel instantaneous sensitivity as seen from Equation C.16) to be similarly asymmetrically distributed, with most values of $T_{\text{eff},i}$ falling below the simple mean $((\sum_i^n T_i)/n)$. This will therefore cause the effective time of a co-added observation to be less than the sum of the individual actual times ($T_{\text{eff,coadd}} \leq \sum_i^n T_i$).

Another reason why the $T_{\text{eff},i} - T_i$ differences are asymmetrically distributed around zero is because the effective time ($T_{\text{eff},i}$) itself depends on $1/\sigma_i^{*^2}$ as shown by Equation C.16. Thus even a symmetric distribution of $\sigma_i^{*^2}$ around $< \sigma_i^{*^2} >$ would result in an asymmetric $T_{\text{eff},i} - T_i$ distribution. This effect, in fact, tends to give $T_{\text{eff},i} > T_i$, giving $T_{\mathrm{eff,coadd}} > \sum_i^n T_i$. If one uses a simple reciprocal mean to calculate the mean pixel-to-pixel instantaneous sensitivity ($< \sigma_i^{*^2} >$) as in Equation C.30, one gets the aforementioned asymmetric distribution of $\sigma_i^{*^2}$ around the mean, but these two reciprocations cancel, yielding an approximately symmetric distribution of $T_{\mathrm{eff},i}/T_i$. However, Because we calculate $< \sigma_i^{*^2} >$ from Equation C.29, the greater asymmetry of $\sigma_i^{*^2}$ around the mean produces a final $T_{\mathrm{eff},i}/T_i$ distribution that is less than unity. This is why $T_{\mathrm{eff,coadd}} \leq \sum_i^n T_i$.

Finally, it is important to note that one gets $T_{\mathrm{eff,coadd}} = \sum_i^n T_i$ with a constant pixel-to-pixel instantaneous sensitivity ($\sigma_i^{*^2} =< \sigma_i^{*^2} >$ for all i). This is because the $\sigma_i^{*^2}$ distribution is collapsed down to a delta function and there is no longer an asymmetry issue.

C.2.2 Within-Pixel Uncertainty

Similar to that of Equation C.15, a within-pixel instantaneous sensitivity can be defined to determine how the mean within-pixel uncertainty integrates down with time. Let $\sigma^2_{\mathrm{pix},i}$ be the within-pixel variance of the i'th pixel in a given map (as defined by Equation C.9). The (weighted) mean value of this within-pixel variance over the entire map of N pixels is

$$< \sigma^2_{\mathrm{pix},i} >= \frac{\sum_i^N \left(\sigma^2_{\mathrm{pix},i} / \sigma^2_{\sigma^2_{\mathrm{pix},i}} \right)}{\sum_i^N \left(1/\sigma^2_{\sigma^2_{\mathrm{pix},i}} \right)}. \tag{C.31}$$

The variance of the within-pixel variance of pixel i ($\sigma^2_{\sigma^2_{\mathrm{pix},i}}$) is simply $\sigma^2_{\mathrm{pix},i}/(2N_i)$ where N_i is the number of hits in pixel i. This reduces Equation C.31 to

$$\begin{aligned} < \sigma^2_{\mathrm{pix},i} > &= \frac{\sum_i^N \left[\sigma^2_{\mathrm{pix},i} / (\sigma^2_{\mathrm{pix},i}/(2N_i)) \right]}{\sum_i^N \left[1/(\sigma^2_{\mathrm{pix},i}/(2N_i)) \right]} \\ &= \frac{\sum_i^N (2N_i)}{\sum_i^N (2N_i/\sigma^2_{\mathrm{pix},i})} \\ &= \frac{\sum_i^N T_{\mathrm{pix},i}}{\sum_i^N (T_{\mathrm{pix},i}/\sigma^2_{\mathrm{pix},i})}, \end{aligned} \tag{C.32}$$

where $T_{\rm pix,\it i} = N_i \Delta t$ is the total integration time in pixel i. The within-pixel instantaneous sensitivity of pixel i is analogous to the pixel-pixel instantaneous sensitivity of Equation C.15:

$$\sigma^*_{\rm pix,\it i} = \sigma_{\rm pix,\it i} T^{1/2}_{\rm pix,\it i}.$$

The variance of the within-pixel instantaneous sensitivity is as follows:

$$\sigma^2_{\sigma^{*2}_{\rm pix,\it i}} = \sigma^2_{\sigma^2_{\rm pix,\it i}} T_{\rm pix,\it i} = \frac{\sigma^2_{\rm pix,\it i}}{2N_i} T_{\rm pix,\it i} = \frac{\sigma^{*2}_{\rm pix,\it i}}{2N_i} = \sigma^{*2}_{\rm pix,\it i} \frac{\Delta t}{2T_{\rm pix,\it i}}.$$

Thus as one might expect, the uncertainty of the within-pixel instantaneous sensitivity ($\sigma_{\sigma^{*2}_{\rm pix,\it i}}$) goes down as $T^{-1/2}_{\rm pix,\it i}$.

We can now derive a proper expression for the mean value of within-pixel instantaneous sensitivity across the entire map:

$$\begin{aligned} < \sigma^{*2}_{\rm pix,\it i} > &= \frac{\sum_i^N \left(\sigma^{*2}_{\rm pix,\it i} / \sigma^2_{\sigma^{*2}_{\rm pix,\it i}} \right)}{\sum_i^N \left(1/\sigma^2_{\sigma^{*2}_{\rm pix,\it i}} \right)} \\ &= \frac{\sum_i^N [\sigma^{*2}_{\rm pix,\it i} / (\sigma^{*2}_{\rm pix,\it i} \Delta t / (2T_{\rm pix,\it i}))]}{\sum_i^N [1/(\sigma^{*2}_{\rm pix,\it i} \Delta t/(2T_{\rm pix,\it i}))]} \\ &= \frac{\sum_i^N T_{\rm pix,\it i}}{\sum_i^N (T_{\rm pix,\it i}/\sigma^{*2}_{\rm pix,\it i})}. \end{aligned} \tag{C.33}$$

We now define the total map integration time as $T_{\rm map} = \sum_i^N T_{\rm pix,\it i}$ which gives

$$\frac{T_{\rm map}}{< \sigma^{*2}_{\rm pix,\it i} >} = \sum_i^N \left(\frac{T_{\rm pix,\it i}}{\sigma^{*2}_{\rm pix,\it i}} \right).$$

It is important to note that this result is not necessary what we would expect. We might naively expect the relation for the mean instantaneous sensitivity:

$$\begin{aligned} < \sigma^{*2}_{\rm pix,\it i} > &\overset{?}{=} < \sigma^2_{\rm pix,\it i} > T_{\rm map} \\ &\overset{?}{=} \frac{\sum_i^N T_{\rm pix,\it i}}{\sum_i^N (T_{\rm pix,\it i}/\sigma^2_{\rm pix,\it i})} T_{\rm map} \\ &\overset{?}{=} \frac{T^2_{\rm map}}{\sum_i^N (T^2_{\rm pix,\it i}/\sigma^{*2}_{\rm pix,\it i})}. \end{aligned}$$

Rearranging,

$$\frac{T_{\mathrm{map}}^2}{<\sigma^{*^2}_{\mathrm{pix},i}>} \overset{?}{=} \sum_i^N \left(\frac{T^2_{\mathrm{pix},i}}{\sigma^{*^2}_{\mathrm{pix},i}} \right)$$

This guess is incorrect because it overweights those pixels with greater integration time.

In the simple case of pixel-independent instantaneous sensitivities ($\sigma^{*^2}_{\mathrm{pix},i} = \sigma^{*^2}_{\mathrm{pix}}$), the mean within-pixel instantaneous sensitivity (Equation C.33) simplifies greatly:

$$<\sigma^{*^2}_{\mathrm{pix},i}>= \sigma^{*^2}_{\mathrm{pix},i} = \sigma^{*^2}_{\mathrm{pix}}. \tag{C.34}$$

However, the mean within-pixel variance (Equation C.32) does not simplify:

$$\begin{aligned} <\sigma^2_{\mathrm{pix},i}> &= \frac{\sum_i^N T_{\mathrm{pix},i}}{\sum_i^N (T_{\mathrm{pix},i}/\sigma^2_{\mathrm{pix},i})} \\ &= \frac{\sum_i^N T_{\mathrm{pix},i}}{\sum_i^N [T_{\mathrm{pix},i}/(\sigma^{*^2}_{\mathrm{pix},i}/T_{\mathrm{pix},i})]} \\ &= \frac{\sum_i^N T_{\mathrm{pix},i}}{\sum_i^N (T^2_{\mathrm{pix},i}/\sigma^{*^2}_{\mathrm{pix},i})} \\ &= \sigma^{*^2}_{\mathrm{pix}} \frac{\sum_i^N T_{\mathrm{pix},i}}{\sum_i^N T^2_{\mathrm{pix},i}}. \end{aligned} \tag{C.35}$$

This is because while the within-pixel instantaneous sensitivities ($\sigma^{*^2}_{\mathrm{pix},i}$) may be uniform across the entire map, there may be variations in the within-pixel uncertainties ($\sigma^2_{\mathrm{pix},i}$) due to variations in the individual pixel times ($T_{\mathrm{pix},i}$). Thus the mean within-pixel uncertainty ($<\sigma^2_{\mathrm{pix},i}>$) is not a particularly good statistic to rely for error analysis on except in the uniform coverage case, where $T_{\mathrm{pix},i}$ is constant over the entire map. The mean within-pixel instantaneous sensitivity ($<\sigma^{*^2}_{\mathrm{pix},i}>$) makes the milder assumption of uniform sensitivity.

Examination of the mean within-pixel uncertainty and the mean within-pixel instantaneous sensitivity for 2.1 mm Lynx blank-field data and 1.1 mm MS2053 cluster data shows a constant mean within-pixel instantaneous sensitivity, implying a pixel independent instantaneous sensitivity as presented in Equation C.34.

What if the assumption of pixel-independent within-pixel instantaneous sensitivity is not valid? Deviations from a constant mean within-pixel instantaneous sensitivity with integration time as implied by Equation C.34 would imply such a scenario. The expected behavior of within-pixel instantaneous sensitivity with integration in time is not trivial in this case because when we co-add, we weight the maps by the pixel-to-pixel variances, not by the true integration time or the within-pixel variances. That is for each pixel (recall from Equation C.10):

$$m_{\text{coadd}} = \frac{\sum_i^n \left(m_i/\sigma_i^2\right)}{\sum_i^n \left(1/\sigma_i^2\right)},$$

where σ_i^2 is the pixel-to-pixel variance of the i'th map. The within-pixel variance of each pixel is then (following the argument of Equations C.11-C.12)

$$\begin{aligned} \sigma^2_{\text{pix,coadd}} &= \frac{\sum_i^n (< m_i^2 > /\sigma_i^4)}{\left[\sum_i^n (1/\sigma_i^2)\right]^2} \\ &= \frac{\sum_i^n (\sigma^2_{\text{pix},i}/\sigma_i^4)}{\left[\sum_i^n (1/\sigma_i^2)\right]^2}, \end{aligned} \tag{C.36}$$

where we have again assumed that different maps are uncorrelated with each other (i.e., $< m_i m_j >= 0$ for $i \neq j$.)

One immediately can identify the problem. This expression can not be further reduced because, in general, there is no simple relation between $\sigma^2_{\text{pix},i}$ and σ_i^2. They are given by the high- and low-frequency components of the PSD, which in general are unrelated unless all the sky noise has been removed. In trying to calculate the average instantaneous sensitivity of the co-added map, $\sigma^{*2}_{\text{pix,coadd}}$, one runs into similar difficulties.

Consider the case where the within-pixel instantaneous sensitivity ($\sigma^{*2}_{\text{pix},i}$) were uniform across each individual map (a reasonable assumption) and the same for all maps (a less reasonable assumption, but good to the extent that we are dominated by photon noise from the time-independent dewar and telescope loading). In this case, if we use the effective time instead of the true time, we will integrate down as $T_{\text{eff}}^{-1/2}$.

We define an effective instantaneous sensitivity by replacing T by T_{eff} (as defined by Equation C.22) everywhere in the definitions of $\sigma^2_{\text{pix},i}$ and $\sigma^{*2}_{\text{pix},i}$. Since T_{eff} is a map based quantity rather than a pixel based quantity, it holds that the scaling between $\sigma^2_{\rm pix,\it i}$ and $\sigma^2_{\rm pix,eff,\it i}$, and $\sigma^{*^2}_{\rm pix,\it i}$ and $\sigma^{*^2}_{\rm pix,eff,\it i}$ is the same for all pixels in a map. This scaling is simply

$$\sigma^2_{\rm pix,eff,\it i} = \sigma^2_{\rm pix,\it i}\frac{\sigma^{*^2}_i}{<\sigma^{*^2}_i>} = \sigma^2_{\rm pix,\it i}\frac{T_i}{T_{{\rm eff},i}}$$

$$\sigma^{*^2}_{\rm pix,eff,\it i} = \sigma^{*^2}_{\rm pix,\it i}\frac{\sigma^{*^2}_i}{<\sigma^{*^2}_i>} = \sigma^{*^2}_{\rm pix,\it i}\frac{T_i}{T_{{\rm eff},i}}.$$

That is, if a given map's pixel-to-pixel instantaneous sensitivity is worse than the average (and the effective time is lower than the average), the map's effective within-pixel variance and effective within-pixel instantaneous sensitivity are correspondingly artificially worsened.

Now we calculate the value of the effective co-added within-pixel instantaneous sensitivity of each pixel of the co-added map ($\sigma^{*^2}_{\rm pix,eff,coadd}$). First we must calculate the effective co-added within-pixel variance ($\sigma^2_{\rm pix,eff,coadd}$) for each pixel. From Equation C.36:

$$\begin{aligned}
\sigma^2_{\rm pix,eff,coadd} &= \frac{\sum_i^n(\sigma^2_{\rm pix,eff,\it i}/\sigma^4_i)}{\left[\sum_i^n(1/\sigma^2_i)\right]^2} \\
&= \frac{\sum_i^n(\sigma^2_{\rm pix,\it i}\sigma^{*^2}_i/(<\sigma^{*^2}_i>\sigma^4_i))}{\left[\sum_i^n(1/\sigma^2_i)\right]^2} \\
&= \frac{\sum_i^n(\sigma^2_{\rm pix,\it i}T_i\sigma^2_i/\sigma^4_i)}{<\sigma^{*^2}_i>\left[\sum_i^n(1/\sigma^2_i)\right]^2} \\
&= \frac{\sum_i^n(\sigma^2_{\rm pix,\it i}T_{\rm pix,\it i}/(a_i\sigma^2_i))}{<\sigma^{*^2}_i>\left[\sum_i^n(1/\sigma^2_i)\right]^2} \\
&= \frac{\sum_i^n(\sigma^{*^2}_{\rm pix,\it i}/(a_i\sigma^2_i))}{<\sigma^{*^2}_i>\left[\sum_i^n(1/\sigma^2_i)\right]^2},
\end{aligned}$$

where $a_i = T_{\rm pix,\it i}/T_i < 1$ is the fraction of the integration time of the i'th map that is spent in the pixel. We have also defined the within-pixel instantaneous sensitivity for the map to be $\sigma^*_{\rm pix,\it i} = \sigma_{\rm pix,\it i}T_i^{1/2}$.

As previously discussed, we now assume the within-pixel instantaneous sensitivity is uniform over each individual map and over time ($\sigma^{*^2}_{\rm pix,\it i} = \sigma^{*^2}_{\rm pix}$), and that the map coverage pattern is the same (though not necessarily uniform) for all maps ($a_i = a$):

$$\begin{aligned}\sigma^2_{\mathrm{pix,eff,coadd}} &= \frac{\sigma^{*^2}_{\mathrm{pix}}/a}{<\sigma^{*^2}_i> \sum_i^n (1/\sigma_i^2)} \\ &= \frac{\sigma^{*^2}_{\mathrm{pix}}\sigma_{\mathrm{coadd}}}{a<\sigma^{*^2}_i>},\end{aligned}$$

where $\sigma^2_{\mathrm{coadd}}$ is the pixel-to-pixel variance of the co-added map as defined by Equation C.13. Equation C.23 showed the pixel-to-pixel variance to be $\sigma^2_{\mathrm{coadd}} =< \sigma^{*^2}_i > /T_{\mathrm{eff,coadd}}$, which yields

$$\begin{aligned}\sigma^2_{\mathrm{pix,eff,coadd}} &= \frac{\sigma^{*^2}_{\mathrm{pix}}}{aT_{\mathrm{eff,coadd}}} \\ &= \frac{\sigma^{*^2}_{\mathrm{pix}}}{T_{\mathrm{pix,eff,coadd}}},\end{aligned}$$

where we have taken the co-added within-pixel effective time to be $T_{\mathrm{pix,eff,coadd}} = aT_{\mathrm{eff,coadd}}$, which is valid under the aforementioned assumption that the map coverage pattern is the same for all maps $(a_i = a)$. Therefore under the assumptions of uniform within-pixel instantaneous sensitivity $\sigma^{*^2}_{\mathrm{pix}}$, and a coverage pattern a_i that is the same for each map, we find that the within-pixel effective dispersion for each pixel of a co-added map ($\sigma_{\mathrm{pix,eff,coadd}}$) integrates down as $T^{-1/2}_{\mathrm{pix,eff,coadd}}$ as we would expect. Note that when the assumption of $\sigma^{*^2}_{\mathrm{pix},i} = \sigma^{*^2}_{\mathrm{pix}}$ was made, we made the more strict assumption that the within-pixel instantaneous sensitivity is uniform over both each individual map and over time. The same result would be obtained in the unlikely event that the within-pixel instantaneous sensitivity was constant only over time, with non-uniform sensitivities over each map (i.e., it is unlikely that the within-pixel instantaneous sensitivity could vary with map position but not between maps).

We are now ready to calculate the effective co-added within-pixel instantaneous sensitivity of each pixel of the co-added map ($\sigma^{*^2}_{\mathrm{pix,eff,coadd}}$):

$$\begin{aligned}\sigma^{*^2}_{\mathrm{pix,eff,coadd}} &= \sigma^2_{\mathrm{pix,eff,coadd}} T_{\mathrm{pix,eff,coadd}} \\ &= \sigma^{*^2}_{\mathrm{pix}}.\end{aligned}$$

This is, of course, exactly what we hoped for given our assumption of uniform within-pixel instantaneous sensitivity. That is, the effective within-pixel instantaneous sensitivity from a co-added map is simply equal to the true within-pixel instantaneous sensitivity.

Now we are able to average over all N pixels and calculate the mean effective within-pixel dispersion ($<\sigma_{\rm pix,eff,coadd}>$) and the mean effective within-pixel instantaneous sensitivity for a co-added map ($<\sigma^*_{\rm pix,eff,coadd}>$). From Equations C.32 and C.33:

$$\begin{aligned}
<\sigma^{*2}_{\rm pix,eff,coadd}> &= \frac{\sum_j^N T_{\rm pix,eff,coadd,\it j}}{\sum_j^N (T_{\rm pix,eff,coadd,\it j}/\sigma^{*2}_{\rm pix,eff,coadd,\it j})} \\
&= \frac{\sum_j^N T_{\rm pix,eff,coadd,\it j}}{\sum_j^N (T_{\rm pix,eff,coadd,\it j}/\sigma^{*2}_{\rm pix})} \\
&= \sigma^{*2}_{\rm pix}
\end{aligned}$$

$$\begin{aligned}
<\sigma^{2}_{\rm pix,eff,coadd}> &= \frac{\sum_j^N T_{\rm pix,eff,coadd,\it j}}{\sum_j^N (T_{\rm pix,eff,coadd,\it j}/\sigma^{2}_{\rm pix,eff,coadd,\it j})} \\
&= \frac{\sum_j^N T_{\rm pix,eff,coadd,\it j}}{\sum_j^N (T^2_{\rm pix,eff,coadd,\it j}/\sigma^{*2}_{\rm pix})} \\
&= \sigma^{*2}_{\rm pix}\frac{\sum_j^N T_{\rm pix,eff,coadd,\it j}}{\sum_j^N T^2_{\rm pix,eff,coadd,\it j}}.
\end{aligned}$$

These expressions are of the same form as Equations C.34 and C.35 for the mean within-pixel variance ($<\sigma^2_{{\rm pix},i}>$) and mean within-pixel instantaneous sensitivity ($\sigma^{*2}_{{\rm pix},i}>$) averaged over a single map, except now the time of interest is the effective co-added pixel integration time rather than the true integration time. Note that if the pixels have the same integration time ($T_{\rm pix,eff,coadd,\it j} = T_{\rm pix,eff,coadd}$) then

$$<\sigma^2_{\rm pix,eff,coadd}>= \frac{\sigma^{*2}_{\rm pix}}{T_{\rm pix,eff,coadd}},$$

which is as one would expect. (Note that we have used $T_{\rm pix,eff,coadd} = \sum_j^N T_{\rm pix,eff,coadd,\it j}$ as the total integration time of the co-added map.)

Thus for a co-added map, one can define a quantity $\sigma^{*^2}_{\text{pix,eff,coadd}}$ that should be totally independent of the integration time under the assumptions of a uniform within-pixel sensitivity over time and the save coverage pattern for all map being co-added. Deviation of the quantity from a line of zero slope indicate fixed-pattern noise that is not integrating down.

C.3 Mapping Speed

The mapping speed of a given map, i, is defined as the amount of sky coverage mapped down to a certain noise level in a certain amount of time. We wish to determine the mapping speed for a co-added map for several observations. In terms of sensitivity, the mapping speed (MS_i) for a single observation, i, is

$$MS_i = \frac{N_{\text{bolo}}\Omega_{\text{beam}}}{\sigma^{*^2}_i}, \tag{C.37}$$

where N_{bolo} is the number of working bolometers used to make the map, Ω_{beam} is the solid angle of the beam, and σ^*_i is the pixel-to-pixel instantaneous sensitivity of map i:

$$\sigma^*_i = \sigma_i T^{1/2}_{\text{pix},i},$$

where σ_i is the weighted pixel-to-pixel dispersion as defined by Equation C.24 and $T_{\text{pix},i}$ is the average per-pixel dwell time in map i. Assuming uniform coverage, it holds that

$$T_{\text{pix},i} = T_{\text{map},i}\frac{N_{\text{bolo}}}{N_{\text{pix},i}}, \tag{C.38}$$

where $N_{\text{pix},i}$ is the number of pixels in map i, and $T_{\text{map},i}$ is the total integration time in the map:

$$T_{\text{map},i} = \frac{N_{\text{hits},i}}{N_{\text{bolo}}\text{SamplingRate}},$$

where $N_{\text{hits},i}$ is the total number of frames used to make the map. Equation C.38 is more intuitive when rewritten as

$$T_{\text{pix},i}N_{\text{pix},i} = T_{\text{map},i}N_{\text{bolo}}.$$

We can now transform the mapping speed equation (C.37) into an equivalent expression that is more intuitive:

$$\begin{aligned} MS_i &= \frac{N_{\text{bolo}}\Omega_{\text{beam}}}{\sigma_i^{*^2}} \\ &= \frac{N_{\text{bolo}}\Omega_{\text{beam}}}{\sigma_i^2 T_{\text{pix},i}} \\ &= \frac{N_{\text{bolo}}\Omega_{\text{beam}}}{\sigma_i^2 (T_{\text{map},i} N_{\text{bolo}}/N_{\text{pix},i})} \\ &= \frac{N_{\text{pix},i}\Omega_{\text{beam}}}{\sigma_i^2 T_{\text{map},i}} \\ &= \frac{A_{\text{map},i}}{\sigma_i^2 T_{\text{map},i}}. \end{aligned}$$

where $A_{\text{map}} = N_{\text{pix},i}\Omega_{\text{beam}}$ is the sky coverage obtained, and σ_i is usually converted to units of mJy^2 by means of a calibrator.

As the pixel size is increased, the corresponding pixel-to-pixel variance of the map will decrease due to the greater number of hits in each pixel. In order to obtain the mapping speed per beam, the map (with pixel areas less than a beam) is convolved with the shape of the beam on the sky (roughly a Gaussian with FWHM of $35''$ at 1.1 mm and $58.5''$ at 2.1 mm), causing the pixel-to-pixel variance of the smoothed map, and thus the mapping speed, to be independent of the pixel size used to make the map.

For a co-added map, an effective time ($T_{\text{eff},\text{map},i}$) must be used (rather than an actual time) as we will now show. In the case of a co-added map, we have from Equation C.23:

$$\sigma_{\text{coadd}}^{*^2} = \sigma_{\text{coadd}}^2 T_{\text{eff},\text{coadd}}.$$

Recall that $T_{\text{eff},\text{coadd}}$ is per-pixel effective dwell time for the co-added map. One can write an expression analogous to that of Equation C.38 for a co-added map:

$$T_{\text{eff},\text{coadd}} = T_{\text{eff},\text{coadd},\text{map}} \frac{N_{\text{bolo}}}{N_{\text{pix},\text{coadd}}}.$$

This expression defines $T_{\text{eff},\text{coadd},\text{map}}$ in a reasonable way. With this definition, we repeat the analysis of Equations C.39-C.39, yielding:

$$MS_{\text{coadd}} = \frac{N_{\text{bolo}}\Omega_{\text{beam}}}{\sigma^{*2}_{\text{coadd}}} = \frac{A_{\text{map,coadd}}}{\sigma^2_{\text{coadd}} T_{\text{eff,coadd,map}}}.$$

Thus the effective co-added time ($T_{\text{eff,coadd,map}}$) should be used in calculating the mapping speed. It is reasonable to expect this because we have previously shown that the raw sum of the per-pixel dwell time ($T_{\text{coadd,map}} = \sum_i^n T_i$) is not a very useful quantity (see § C.2.1). This is due to variations in instantaneous sensitivity with time (i.e., $\sigma^{*2}_i \neq < \sigma^{*2}_i >$ in general). Essentially, all ticks of the clock are not created equal because of variations in σ^{*2}_i. Therefore it is not proper to use $T_{\text{coadd,map}}$ in the denominator of the mapping speed expression and instead $T_{\text{eff,coadd,map}}$ should be used. This will both stabilize the mapping speeds as well as yield a mapping speed that is consistent with $< \sigma^{*2}_i >$.

Appendix D

Multiwavelength Coverage

D.1 Multiwavelength Coverage

Observations at both longer and shorter wavelengths are necessary to characterize high redshift submillimeter galaxies. Radio identifications provide precise astrometry which allow optical and infrared counterparts to be identified. The radio observations detect the synchrotron emission (presumably from high energy cosmic rays associated with supernova explosions, see review by Condon 1992), which is known to be correlated to the far-infrared luminosity (and is thus correlated to the Bolocam flux density, which traces the dust emission that is responsible for the infrared luminosity). The Bolocam and radio points may then be used to obtain temperature and redshift estimates. Multiple submillimeter wavelengths are essential in confirming the Bolocam sources and allow for a photometric redshift measurement that is independent of the radio-to-far-IR correlation (i.e., using only the submillimeter portion of the spectrum for an assumed temperature). Furthermore, a third photometric redshift estimate using the 1.6 μm bump in the stellar emission spectrum is possible using the near- and mid-infrared portion of the spectrum. In this appendix we briefly discuss the multiwavelength coverage (submillimeter, radio, infrared, optical, and X-ray) of the Lockman Hole and the coincident detections of each survey. Figure 10.2 presents an overview of the Bolocam detections, including all of the submillimeter, radio, and infrared counterparts.

D.1.1 Submillimeter Surveys

Four submillimeter / millimeter surveys of the Lockman Hole region are considered. Three of the surveys (Bolocam, SCUBA, MAMBO) represent blank-field surveys, while the SHARC II survey covers only the 17 Bolocam sources. The surveys include:

1) Entire Bolocam Lockman Hole survey at 1.1 mm (this work). The survey covers 324 arcmin^2 down to an RMS of 1.4 mJy/beam and includes 17 source candidates ($\geq 3\ \sigma$) ranging in flux densities from 4.0 to 6.8 mJy. Extensive simulations and jackknife tests yielded 6 expected false detections. The Bolocam beam size is $31''$ and observations were taken without chopping while scanning at $60''\ \text{s}^{-1}$. The Bolocam survey includes the entire regions surveyed by the published 8 mJy 850 μm JCMT SCUBA (Scott et al., 2002) and 1.2 mm IRAM MAMBO (Greve et al., 2004) surveys. Using a model SED based on nearby, dusty, star-forming galaxies (see § 11) gives relative flux densities of $1:2.0:0.8$ and relative RMSs of $1:0.9:0.6-1.4$ for the Bolocam, SCUBA, and MAMBO surveys, respectively, for a galaxy redshift of $z = 2.4$ (with the range given for MAMBO due to nonuniform noise).

2) JCMT SCUBA 8 mJy survey (Scott et al., 2002). The survey covers 122 arcmin^2 (in the Lockman Hole) to an RMS of 2.5 mJy/beam with a $14''$ beam, and includes 36 source candidates ($\geq 3\ \sigma$). Five sources of the Scott et al. (2002) catalog (LE850.9, 10, 11, 15, 20) were retracted by Ivison et al. (2002) on the basis of large $\sigma_{850\mu m}$ values (and lack of radio identifications). The SCUBA survey detects 6 of the 8 Bolocam detections in the overlap region between the surveys (Bolocam 5, 8, 13, 14, 16, and 17).

3) 1.2 mm IRAM MAMBO survey (Greve et al., 2004). The survey covers 197 arcmin^2 (in the Lockman Hole) to an RMS of 0.6-1.5 mJy/beam, with a $10.7''$ beam. The survey includes 23 sources ($\geq 3\ \sigma$). The MAMBO survey detects 7 of the 11 Bolocam detections in the overlap region between the surveys (Bolocam 1, 4, 5, 8, 14,

16, and 17).

4) 350 μm SHARC II observations of the Lockman Hole (this work – see § 10.1). The instrument beam is $9''$ and the observations were taken with a Lissajous scan pattern with uniform coverage regions of $95'' \times 18''$ to an RMS of 6-18 mJy/beam (with deeper integrations taken for fainter sources). A total of 14 sources were detected (3 by Kovács et al., 2005), 11 of which coincide with 9 Bolocam sources. (An additional 3 SHARC II sources were detected outside of the Bolocam positional error circles.)

To summarize, the majority of the Bolocam sources within the regions covered by other submillimeter surveys were detected (SCUBA detects 6 of 8 Bolocam detections, MAMBO detects 7 of 11, and SHARC II detects 9 of 17). Seven of the Bolocam source candidates were not detected by any other submillimeter survey (Bolocam 7, 9, 10, 11, 12, 13, and 15, each of which was detected at $< 3.5\ \sigma$), which is consistent with the 6 false detections (Poisson distributed) expected from simulations. These results point to the robustness of the remaining Bolocam galaxy candidates.

D.1.2 Radio Detections

Three independent VLA radio surveys were used to identify counterparts to the Bolocam sources. In addition, this work re-analyzes the Ivison et al. (2002) data set to obtain a complete source catalog over the entire Bolocam source catalog. The radio surveys include:

Published Surveys:

1) VLA radio source list at 1.4 GHz of the SCUBA 8 mJy survey sources (Ivison et al., 2002). The Lockman East radio survey reached an average noise level of 4.8 μJy beam^{-1} with a $1.3''$ FWHM circular beam. Coincident sources (and 5σ upper limits) are given for each of the 21 brighter ($> 3\sigma$) SCUBA sources, with 20 positive detections over 14 of the sources. Five of the 21 SCUBA sources (LE850.9, 10, 11, 15, 20) are ignored on the basis of large $\sigma_{850\mu m}$ values (and lack of radio identifications). Of the 8

Bolocam detections covered by this VLA survey, 5 (Bolocam 5, 8, 14, 16, 17) coincide with 7 Ivison et al. (2002) sources. Ivison et al. (2002) also report continuum data at 4.9 GHz (using the VLA in the C configuration), with a resulting noise level of ~ 11 μJy beam^{-1}. Positive detections exist for 8 of the SCUBA galaxies, 4 of which are coincident with Bolocam sources (Bolocam 5, 14, 16, 17).

2) A source list from the 6 cm VLA survey of the Lockman Hole (Ciliegi et al., 2003). The survey has a noise level of $\sim 11\mu$Jy and covers the northeast quadrant of the Bolocam survey, including 7 of the Bolocam sources. A total of 63 sources were detected at $> 4.5\ \sigma$, with a radio counterpart for only one of the Bolocam sources (Bolocam 8).

Unpublished Surveys:

3) A source list of 20 cm VLA observations was obtained from Yun et al. (2005). The observations were broken into four fields, with the northeastern section being deeper (10 μJy/beam RMS) than the other three fields (15 μJy/beam). The observations cover the entire Bolocam field, with a total of 640 sources $> 3.5\sigma$. The source list contains counterparts for 10 of the Bolocam sources (Bolocam 1, 2, 3, 5, 6, 8, 9, 13, 14, 17).

4) Re-analysis of the VLA map from Ivison et al. (2002) by Biggs & Ivison (2006). The survey reached a median noise level in the locality of the 17 Bolocam sources of 4.4 μJy beam^{-1}. Radio sources were extracted from the VLA map within $30''$ from the Bolocam source positions. Counterparts for 15 of the 17 Bolocam sources were detected (all except Bolocam sources 10 and 12). Seven of the detections are coincident with the Ivison et al. (2002) analysis (Bolocam 5, 8, 14, 16, and 17), with flux densities in good agreement (within the stated uncertainties).

In total, 15 of the 17 Bolocam galaxy candidates are found to have at least one radio counterpart (all except Bolocam 10 and 12). As only the VLA observations from Yun et al. (2005) and Ciliegi et al. (2003) include an entire source catalog, we are limited to estimating accidental detection rates for these two surveys. The accidental detection rate is defined as the Poisson likelihood that one or more of these known radio sources, randomly distributed, fall within the 2 σ positional confidence region of the Bolocam beam (see § 10.2). The rates for the Yun et al. (2005) and Ciliegi et al. (2003) surveys are 17-24% and 8-11%, respectively. (The accidental radio detection rate is dominated by the Yun et al. 2005 survey due to its greater relative depth.)

D.1.3 Infrared Detections

Both published and unpublished *Spitzer* observations were used to obtain infrared counterparts to the Bolocam / radio sources. They include:

1) *Spitzer* postage stamps and an extracted source list (this work) with the IRAC (3.6, 4.5, 5.8, and 8.0 μm) and MIPS (24 μm) instruments were obtained for 14 of the 17 Bolocam source candidates for areas within a $16''$ radius of the Bolocam beam centers. (Note that this radius is smaller than the 2 σ positional errors of Bolocam.) Bolocam.LE.1100.2, 6, and 12 fall outside of the region observed with *Spitzer*. Multiple *Spitzer* sources were detected within each of the 14 Bolocam positional error circles.

2) *Spitzer* observations of SCUBA/VLA selected sources (Egami et al., 2004) with IRAC (3.6, 4.5, 5.8, 8.0 μm) and MIPS (24 μm) in a $5' \times 5'$ area of the Lockman Hole region. The MIPS 24 μm field of view is $5.4' \times 5.4'$. The total integration time was 300 seconds per pixel, with a 3 σ detection limit of 120 μJy. The observed region contains the following *Spitzer*, VLA radio, SCUBA, and Bolocam correlations:

- The field imaged by IRAC and MIPS contains 10 SCUBA sources of the Scott et al. (2002) catalog (LE850.1, 4, 7, 8, 10, 14, 18, 23, 24, 35).

- Ivison et al. (2002) detected radio counterparts for 5 (LE850.1, 7, 8, 14, 18) of the 7 secure ($\geq$ 3.5 σ) SCUBA sources at high significance and a radio counterpart for LE850.4 with lower significance.

- Egami et al. (2004) finds an additional radio counterpart to LE850.4 upon re-examination of the VLA map.

- Of these 7 SCUBA sources with a total of 9 radio components (LE850.1, 4, 7, 8a, 8b, 14a, 14b, 18, 35), all are found to have *Spitzer* counterparts.
- *Spitzer* counterparts are found only for the sources with radio detections.
- Four of the 9 *Spitzer* detections (LE850.1, 8a, 8b, 8c) fall within 2 of the Bolocam positional error circles (Bolocam.LE.1100.14 and 17).

D.1.4 Optical Detections

Optical counterparts to the Bolocam / radio sources were obtained from three deep surveys, including:

1) SDSS u, g, r, i, z photometry was obtained from the public SDSS data release 3 (DR3) website[1] , including 7,148 objects in the Lockman Hole region. The 61 objects falling within the Bolocam positional error circles include 43 galaxies (extended) and 18 stars (point-like).

2) A list of objects with Johnson R-band (Subaru) photometry was obtained from Yun et al. (2005) for each of the Yun et al. (2005) VLA 20 cm radio sources. The optical catalog consists of 1,031 objects down to a limiting magnitude of R = 24.5. 29 sources were found within the positional error circles of the 10 Bolocam sources covered by the catalog. As no radio sources were detected by Yun et al. (2005) for Bolocam sources 4, 7, 10, 11, 12, 15, and 16, no optical coverage was available for these sources.

3) Optical Johnson R-band (Subaru) photometry was also obtained from Ivison et al. (2005) for most of the Lockman Hole region (with no coverage for Bolocam sources 6, 9, and 11). 50,297 sources were detected down to a limiting magnitude of R = 27. 950 sources lie within the positional error circles of the 14 Bolocam sources covered by the survey.

---

[1] http://cas.sdss.org/dr3/en/tools/search/rect.asp

D.1.5 X-ray Detections

Finally, two X-ray surveys were used to identify Bolocam sources with a possible AGN contribution. The X-ray surveys include:

1) The ROSAT Ultra Deep Survey (Lehmann et al., 2001) source list of the Lockman Hole was cross referenced with the positions of the 17 Bolocam galaxy candidates. The survey reached a flux density level of 1.2×10^{-15} erg cm^{-2} s^{-1} in the 0.5-2.0 keV energy band, detecting 94 X-ray sources. Two of the sources coincide with the Bolocam positions, coincident with the eastern radio source of Bolocam 8 and in-between the two radio sources associated with Bolocam 17. Despite the positional offset, Lehmann et al. (2001) associate the X-ray emission coincident with Bolocam source 17 with the northwestern radio (and optical) source. An additional X-ray detection exists of SHARC II source 3 (in the field of Bolocam source 9), although the SHARC II and X-ray positions lie well outside the positional error circle of the Bolocam source.

2) XMM-Newton observations of the Lockman Hole ($\simeq$ 100 ksec) were taken during the Performance Verification phase of the instrument (Mainieri et al., 2002), yielding 98 sources with more than 70 net counts (flux density limit of 1.6×10^{-15} erg cm^{-2} s^{-1} in the 0.5-7 keV band). Cross referencing the source list with the 17 Bolocam sources yields a coincidence list identical to that of the ROSAT survey.

3) A deep, (1 Msec) unpublished (Ivison et al., 2005) XMM-Newton survey of the majority of the Bolocam good coverage region (Bolocam 2, 6, 11, and 12 are not covered) confirms the above results with only one identification, coincident with Bolocam source 17.

D.2 Previous Redshift Estimates of Bolocam Galaxies

Several of the Bolocam galaxies with radio counterparts have had their redshifts determined with either photometric or spectroscopic techniques. We briefly discuss the

Table D.1. Summary of Multiwavelength Detections of Bolocam Galaxy Candidates

Bolocam Number	Bolocam 1.1 mm mJy	SHARC II 350 μm mJy	SCUBA 850 μm mJy	MAMBO 1.2 mm mJy	Yun 20 cm μJy	Yun (deep) 20 cm μJy	Biggs 20 cm μJy	Ivison 20 cm μJy	Ivison 6 cm μJy	Ciliegi 6 cm μJy	*Spitzer* 3.6 μm mJy	*Spitzer* 4.5 μm mJy	*Spitzer* 5.8 μm mJy	*Spitzer* 8.0 μm mJy	*Spitzer* 24 μm mJy	SDSS[a] u,g,r,i,z	Yun[b] R	Ivison R	Notes
1	6.8±1.4	38.0±9.3	X	5.7±1.0	-	60±13	52±5.7	X	X	-	1(4)	1(4)	-(-)	-(-)	1(-)	-(1,1)	-	1(48)	S radio source
”	”	”	X	”	-	-	53±5.6	X	X	-	1	1	-	1	-	-	X	-	N radio source
2	6.5±1.4	20.9±5.2	X	X	373±58	X	507±9.0	X	X	X	X	X	X	X	X	1,0(0,1)	1	1(74)	N radio source
”	”	”	X	X	-	X	90±9.7	X	X	X	X	X	X	X	X	-	X	1	S radio source
3	6.0±1.4	15.1±3.8	X^c	-	241±39	X	289±9.0	X	X	X	1(10)	1(4)	1(1)	1(-)	1(2)	0,1(0,2)^c	2^d	1(35)	NE SHARC II source
”	”	14.0±3.5	X^c	-	84±20	X	96±7.8	X	X	X	1	1	-	-	1	-	-	1	SW SHARC II source
4	5.2±1.4	-	-	3.2±0.7	-	X	20±6.7	X	X	X	X^c(14)	X^c(13)	X^c(1)	X^c(1)	X^c(3)	1,0(3,2)	X	1(41)	
5	5.1±1.3	35.6±9.7	11±2.6	2.9±0.7^c	X	51±13	51±9.3	54±14	60±35	-	1(10)	1(6)	1(1)	1(-)	1(2)	-(2,0)	3^d	1(47)	E radio source
”	”	-	-	”	X	59±13	42±6.5	X	X	-	1	1	1	1	1	1,0	3	1	S radio source
”	”	-	-	3.1±0.7	X	-	27±5.9	X	X	-	X	X	X	X	X	-	X	-	W radio source
”	”	-	-	-	X	-	29±7.8	X	X	-	X	X	X	X	X	-	X	-	N radio source
6	5.0±1.5	27.6±6.9	X	X	60±17	X	55±9.9	X	X	X	X	X	X	X	X	1,0(4,0)	-	X	E SHARC II, E radio source
”	”	”	X	X	105±22	X	138±11	X	X	X	X	X	X	X	X	-	-	X	E SHARC II, W radio source
”	”	63.6±15.8	X	X	611±93	X	939±16	X	X	X	X	X	X	X	X	1,0	1	X	W SHARC II source
7	4.9±1.5	-	X	X	-	X	51±23	X	X	X	-(6)	-(5)	-(1)	-(-)	-(2)	-(-)	X	-(71)	
8	4.8±1.3	34.5±9.3	10.9±2.4	4.8±0.6	X	-	27±7.6	29±11	-	-	1(13)	1(13)	1(-)	-(-)	1(6)	-(2,1)	X	1(83)	S radio source
”	”	”	”	”	X	46±12	28±6.7	24±9	-	-	1	1	-	1	1	-	-(2)	1	N radio source
”	”	”	-	-	X	136±23	157±8.0	X	X	58±11	X	X	X	X	X	0,1	3	1	E radio source
9	4.8±1.5	-^{c}	X	X	60±18	X	68±11	X	X	X	1(13)	1(14)	1(-)	1(-)	1(5)	-(1,0)	2	X	
10	4.7±1.4	-	-	-	-	X	-	X	X	X	-(6)	-(6)	-(3)	-(1)	-(1)	-(2,1)	X	-(60)	
11	4.6±1.5	-	X	X	-	X	116±33	X	X	X	1(6)	1(4)	-(-)	-(-)	-(-)	1,0(3,2)	X	X	
12	4.6±1.4	-^{c}	X	X	-	X	-	X	X	X	X	X	X	X	X	-(3,0)	X	-(66)^c	
13	4.5±1.4	-	-^{c}	-	63±18	X	63±7.2	X	X	X	-(7)	-(7)	-(1)	-(-)	-(2)	1,0(3,0)	3^d	1(58)	NE radio source
”	”	-	-	-	-	X	27±7.9	X	X	X	1	1	1	-	1	0,1	X	1	E radio source
”	”	-	-	-	-	X	30±7.6	X	X	X	-	-	-	-	-	-	X	-	SE radio source
14	4.4±1.3	24.1±6.0	10.5±1.6^c	3.4±0.6	76±19	78±15	73±7.3	73±10	56±37	-	X^c(7)	X^c(3)	X^c(-)	X^c(-)	X^c(1)	-(1,1)	-	1(83)	S radio source
”	”	-	-	-	-	X	34±7.2	X	X	-	1	1	1	1	1	-	X	1	W radio source
”	”	-	-	-	-	45±12	26±8.4	X	X	-	X^c	X^c	X^c	X^c	X^c	-	1	1	NE radio source
”	”	-	-	-	-	-	26±8.3	X	X	-	-	-	-	-	-	1,0	X	1	SW radio source
15	4.4±1.4	-	X	-	-	X	50±7.7	X	X	-	1(13)	1(12)	1(3)	1(2)	1(2)	1,0(5,0)	X	1(60)	
16	4.1±1.4	44.0±9.0	6.1±1.8	2.8±0.5	X	-	49±8.5	41±12	32±22	-	1(9)	1(7)	1(-)	1(-)	1(-)	-(1,1)	X	1(112)	
17	4.0±1.3	15.5±3.9	5.1±1.3	2.4±0.6	-	-	20±6.6	22±11	-	-	1(4)	1(5)	1(1)	1(0)	1(2)	0,1(3,2)	1	1(91)	NW radio source
”	”	”	”	”	-	54±13	58±9.4	58±12	57±32	-	1	1	1	1	1	-	3(4)	1	SE radio source

[a] The two listed numbers correspond to the SDSS galaxy and star classifications, respectively.

[b] The Optical R band source list (Yun et al., 2005) includes only sources within 3″ of the corresponding radio source.

[c] See source description in § 10.3.2

[d] The multiple Yun et al. (2005) R-band optical sources coincident with the radio source are close in both position ($\leq 1''$) and flux (≤ 0.2 mag), and are likely due to a lack of merging close sources in the catalog.

Note. — An (X) corresponds to Bolocam sources not covered by the survey / source list. Items in parentheses correspond to the detection of sources within the Bolocam positional error circle, but not likely associated with the source.

results of each of these redshift surveys in this section. The spectroscopic redshifts will form the basis of comparison to the photometric redshift techniques discussed in § 11. The previous photometric redshifts also prove useful in considering the merits of including 350 μm SHARC II observations when estimating redshifts of submillimeter galaxies.

1) Chapman et al. (2005) obtained spectroscopic redshifts for a sample of 73 submillimeter galaxies, the largest set of spectroscopic redshifts to date. The sources are a subset of 150 SCUBA/JCMT sources detected at 850 μm over seven separate fields. Requiring accurate positions for spectroscopic identification, 104 of the SCUBA galaxies have radio identifications from deep VLA radio maps at 1.4 GHz. Of these, a subset of 98 sources were observed with the Low Resolution Imaging Spectrograph (LRIS) on the Keck I telescope, resulting in the spectroscopic identification of 73 of these galaxies. Twelve of the sources correspond to the SCUBA sources in the Lockman Hole, 5 of which a coincident with Bolocam galaxy candidates (Bolocam 5, 8, 14, 16 and 17). Chapman et al. (2005) find redshifts of 2.611, 3.036, 2.148, 2.142, 0.686 for the five Bolocam galaxies, respectively. While spectra for each of the Bolocam galaxies are not included among the sample spectra, Chapman et al. (2005) comment that all of the above detections have multiple-line identifications and can therefore be considered robust. The subset of Chapman et al. (2005) redshifts with Bolocam detections ($z = 2.1 \pm 0.9$) is consistent with the overall redshift distribution of the entire sample (with a median redshift of 2.2).

2) Aretxaga et al. (2003) implement a Monte Carlo photometric redshift technique, using existing far-IR - radio multiwavelength data for 77 sources first identified at 850 μm (SCUBA) or 1.2 mm (MAMBO). The technique produces the redshift probability distribution for an individual galaxy by choosing an evolutionary model and generating a catalog of luminosities and redshifts based on template SEDs from local starbursts, ULIRGs, and AGN. Thirteen of the sources correspond to SCUBA sources in

the Lockman Hole, including 5 Bolocam galaxies (Bolocam 5, 8, 14, 16 and 17 – the same subset with Chapman et al. 2005 spectroscopic redshifts). Five different evolutionary models were used, with the results listed in Table D.2. Given the stated uncertainties in the photometric redshifts, the Aretxaga et al. (2003) results are in general agreement with the spectroscopic measurements. Note that the photometric redshift for Bolocam source 17 is consistent with both the modified blackbody and near IR stellar bump models (see § 11.4), further supporting a possible misidentification by Chapman et al. (2005).

3) The ROSAT Ultra Deep Survey (Lehmann et al., 2001) of the Lockman Hole reached a flux density level of 1.2×10^{-15} erg cm^{-2} s^{-1} in the 0.5-2.0 keV energy band detecting 94 X-ray sources. Spectroscopic identifications of 90% of the sources based on highly accurate positions ($2''$ FWHM) with the High Resolution Imager (HRI) and Keck R-band images were performed with the LRIS spectrometer on the Keck telescopes, yielding a single spectroscopic redshift for the northwest optical component of Bolocam source 17. Multiple lines were detected (Mg II, [Ne V], and [O II]) giving a redshift of 0.974 (cf. § 11.4).

4) Oyabu et al. (2005) spectroscopically identified 29 of the 44 far-infrared sources (with accurate 1.4 GHz VLA radio positions) detected in the 0.9 deg^2 *ISO* survey of the Lockman Hole. Optical identifications of the radio sources were performed in both the I- and R-bands (using the University of Hawaii $88''$ and Subaru telescopes), with

Table D.2. Previous Spectroscopic and Photometric Redshifts of Bolocam Galaxies

Bolocam Number	Chapman et al. (2005) $z_{\rm spec}$	Aretxaga et al. (2003) $z_{\rm phot}^{\rm le2}$	Lehmann et al. (2001) $z_{\rm spec}$	Oyabu et al. (2005) $z_{\rm spec}$	Egami et al. (2004) $z_{\rm phot}$
5	2.611(NE)	$2.7^{+1.8}_{-0.7}$(NE)			
6				0.362(W)	
8	3.036(S)	$5.8^{+0.2}_{-1.7}$		1.110(E)	
14	2.148(S)	$2.6^{+0.4}_{-0.5}$(S)			2.6(S)
16	2.142	$3.3^{+1.1}_{-1.3}$			
17	0.689(SE)	$3.7^{+1.5}_{-0.7}$	0.974(NW)		∼3(SE), 0.9

optical spectroscopy performed with both the Keck II and WIYN telescopes. Five of the *ISO* sources fall in the region covered by Bolocam, with 2 sources coinciding with Bolocam sources (6 and 8). Oyabu et al. (2005) find a redshift of 0.362 for the most westerly radio source of Bolocam 6 and a redshift of 1.110 for eastern radio source of Bolocam 8.

5) With *Spitzer* IRAC and MIPS, Egami et al. (2004) positively detect all 9 of the radio sources associated with 7 SCUBA galaxies, including 4 detections of two Bolocam sources (14 and 17). The photometric redshifts using only the near- and mid-infrared points are 2.6 for Bolocam 14, and ~ 3 and 0.9 for the two radio sources near Bolocam 17.